EXTENDED PERFORMANCE SOLAR ELECTRIC PROPULSION THRUST SYSTEM STUDY

Final Report

September 1977

Volume IV

Thruster Technology Evaluation

By

Ion Physics Department Staff

Hughes Research Laboratories

and

Technology Division Staff

Space and Communications Group

of

Hughes Aircraft Company

Prepared For

NATIONAL AERONAUTICS AND SPACE ADMINISTRATION

NASA Lewis Research Center

Contract NAS 3–20395

EXTENDED PERFORMANCE SOLAR ELECTRIC PROPULSION THRUST SYSTEM STUDY

Final Report

September 1977

Volume IV

Thruster Technology Evaluation

By

Ion Physics Department Staff

Hughes Research Laboratories

and

Technology Division Staff

Space and Communications Group

of

Hughes Aircraft Company

Prepared For

NATIONAL AERONAUTICS AND SPACE ADMINISTRATION

NASA Lewis Research Center

Contract NAS 3–20395

TECHNICAL REPORT STANDARD TITLE PAGE

1. Report No.	2. Government Accession No.	3. Recipient's Catalog No.
CR-135281		

4. Title and Subtitle	5. Report Date
EXTENDED PERFORMANCE SOLAR ELECTRIC PROPULSION THRUST SYSTEM STUDY VOLUME IV — THRUSTER TECHNOLOGY EVALUATION	October 1977
	6. Performing Organization Code
7. Author(s) R.L. Poeschel and E.I. Hawthorne, et al.	8. Performing Organization Report No.
9. Performing Organization Name and Address Hughes Aircraft Company Hughes Research Laboratories: 3011 Malibu Canyon Road, Malibu, California 90265 Hughes Space & Com.Group: P.O. Box 92919, Los Angeles, CA 90009	10. Work Unit No.
	11. Contract or Grant No. NAS 3-20395
12. Sponsoring Agency Name and Address National Aeronautics and Space Administration Lewis Research Center 21000 Brookpark Road Cleveland, Ohio 44135	13. Type of Report and Period Covered 14 Feb 1977–29 Aug 1977
	14. Sponsoring Agency Code

15. Supplementary Notes

Project Manager: James Cake, NASA-Lewis Research Center, Cleveland, Ohio

16. Abstract

Ion-thruster technology has progressed during the past decade to the point that it is considered ready for application. During this study, several thrust system design concepts were evaluated and compared using the specifications of the most advanced 30-cm engineering model thruster as the technology base. Emphasis was placed on relatively high-power missions (60 to 100 kW) such as a Halley's comet rendezvous. The extensions in thruster performance required for the Halley's comet mission were defined and alternative thrust system concepts were designed in sufficient detail for comparing mass, efficiency, reliability, structure, and thermal characteristics. Confirmation testing and analysis of thruster and power-processing components were performed, and the feasibility of satisfying extended performance requirements was verified. A baseline design was selected from the alternatives considered, and the design analysis and documentation were refined. The baseline thrust system design features modular construction, "conventional" power processing, and a "concentrator" solar array concept and is designed to interface with the Space Shuttle. A program development plan was formulated that outlines the work structure considered necessary for developing, qualifying, and fabricating the flight hardware for the baseline thrust system within the time frame of a project to rendezvous with Halley's comet during December 1985. An assessment was made of the costs and risks associated with a baseline thrust system as provided to the mission project under this plan. Critical procurements and interfaces were identified and defined. The results of this study are presented in the five volumes of this report.

17. Key Words (Selected by Author(s))	18. Distribution Statement
Solar Electric Propulsion Thrust System Ion Propulsion Ion Thruster	Unclassified-Unlimited

19. Security Classif. (of this report)	20. Security Classif. (of this page)	21. No. of Pages	22. Price*
UNCLASSIFIED	UNCLASSIFIED	113	

*For sale by the Clearinghouse for Federal Scientific and Technical Information, Springfield, Virginia 22151.

FOREWORD

The work described herein was performed by the coordinated efforts of personnel within two divisions of the Hughes Aircraft Company. Responsibility for the study resided in the Ion Physics Department of Hughes Research Laboratories. This department is managed by Mr. J.H. Molitor. A major portion of the thrust system design activity was performed by a team of individuals assembled from the Technology Division of the Space and Communications Group and coordinated and directed by Dr. E.I. Hawthorne. The work was funded under contract NAS3-20395 and monitored by Mr. James E. Cake of the NASA Lewis Research Center. The key technical contributors were

R.L. Poeschel	- Study manager for the final phases of the study and project engineer for the approach confirmation task
E.I. Hawthorne	- Manager of all thrust system design and program development activities
Y.C. Weisman	- Project engineer for structural design
M. Frisman	- Project engineer for structural design
G.C. Benson	- Project engineer for power management and control design
R.J. McGrath	- Project engineer for thermal control design
R.M. Martinelli	- Project engineer for capacitor diode voltage multiplier development and evaluation
T.L. Linsenbardt	- Thermal analysis
J.R. Beattie	- Thruster evaluation

SUMMARY

The primary objective of this study was to provide a data base for a program plan for the development of the ion-propulsion thrust system for the Halley's comet mission spacecraft. This data base was to include: the definition of a design concept, selected from among alternate candidate configurations; the identification of required supporting technology, including the definition of critical areas and potential technical risks; the definition of a program development plan, including a development schedule and an assessment of potential schedule risks; and a preliminary estimate of yearly and total program costs.

A concurrent objective of the study was to conduct a hardware "approach confirmation" technology effort to evaluate the ion thruster's performance and lifetime at the power level required for the Halley's comet mission, to design and evaluate the thruster isolator required for operation at the higher power level, and to evaluate the design of a capacitor-diode voltage multiplier.

A thrust system baseline configuration was identified for the 30-cm extended-performance mercury ion thruster that can perform the Halley's comet rendezvous mission. The configuration is comprised of 10 thrusters configured with a power management and control system and a structure and thermal control system in a modular thrust system design. The power management and control system uses conventional power processing. Power is provided to the thrust system with an 85 kW concentrating solar array. The thrust system mass is 1010 kg (including 15% contingency), the average system efficiency is 70%, and the estimated reliability upper bound is 72%.

Adaptability of the 900-series 30-cm thruster design to the 6 to 7 kW range required for the Halley's comet mission was demonstrated with only minor design modification required, and an acceptable high-voltage isolator design was validated by latoratory tests. The design and performance of an alternate power management and control system design approach utilizing the capacitor-diode voltage multiplier was successfully demonstrated by laboratory model tests at power levels in excess of 1 kW.

The technology efforts mentioned above assisted in the identification of the level of technical risks associated with the thrust system design. These risks have been found amenable to resolution through normal engineering development and, therefore, judged to be acceptable for mission application.

The program plan, which includes the procurement plan generated for the baseline configuration, is a viable plan that provides for delivery in May 1981 of the flight thrust system to be integrated with the mission module and solar array. The cost of the thrust system development program is projected to be 54 million dollars (in fiscal year 1977 dollars) excluding contractor fee, of which approximately 13.5 million dollars will be required in fiscal year 1978.

In contrast to the low technical risk, the schedule risk for initiating this program development is of particular concern. Timely approval of the authorization of 13.5 million dollars for fiscal year 1978 must be granted so that the pre-project, or advanced development, activities can be initiated.

TABLE OF CONTENTS

LIST OF ILLUSTRATIONS

SECTION I

INTRODUCTION

This report summarizes the results of a six-month study to define the design, program plan, and costs of the ion-propulsion thrust system for the Halley's comet mission spacecraft. The modular characteristics of the design developed during this study also make it applicable as the prime space propulsion system for other potential missions.

This study, which is based on an initial system characterization (completed 7 February 1977) performed by the National Aeronautics and Space Administration's Lewis Research Center (NASA LeRC), was performed in three parts:

- Design tradeoff studies (14 February to 15 April 1977) to define and compare alternate design approaches
- Conceptual design definition, program plan, and costs of a selected design approach (15 April to 15 June 1977)
- Approach confirmation of supporting technology in selected areas.

The results of this study are presented in five volumes. Volume I summarizes the results of the entire program. Volume II discusses the conceptual design, program development plan, and cost estimates for the selected baseline thrust system design. Volume III describes the design tradeoff studies performed to compare alternate design approaches. This volume, Volume IV, describes the evaluation of thruster technology for extended-performance applications. Volume V presents the details of the capacitor-diode voltage multipler (CDVM) circuit analysis and experimental evaluation. The results reported in these volumes have also been presented in briefings at NASA LeRC.

A. BACKGROUND

In the fall of 1976, the Office of Aeronautics and Space Technology (OAST) was given the responsibility of assessing the capability of the electric propulsion technology under development at NASA LeRC and of the

solar array technology under development at Marshall Space Flight Center (MSFC) and the Jet Propulsion Laboratory (JPL) to perform the Halley's comet rendezvous mission proposed by JPL. OAST established an "August Project" team from members of the three organizations to develop a preliminary program plan to support a fiscal year (FY) 1979 new start.

The August Project consisted of parallel efforts by JPL, NASA LeRC, and MSFC to define the design approach, program plan, costs, and risks of the Halley's comet mission. Three areas were considered: the spacecraft (including the science payload), the ion propulsion subsystem (referred to as the thrust system in this report), and the solar array. The NASA LeRC program was conducted in two phases. First, initialization studies (completed 15 February 1977) were conducted to define requirements and to identify preliminary design characteristics. Second, during the 15 February to 15 July period, alternative thrust-system configurations were analyzed, and a baseline was defined, the program plan and projected costs were generated, and a risk assessment was made. To perform these design studies it was necessary to postulate or extrapolate extended-performance characteristics in several technology areas. Consequently, studies were conducted in four technology areas to confirm the validity of the design approaches that were considered.

The thrust systems that were considered are based on the electric propulsion technology that NASA LeRC has been developing for over a decade. The technical baseline for this application is the most recent operational engineering model thruster (EMT), the 900-series 30-cm mercury ion EMT. This thruster is a scaled-up version of the 15-cm thruster developed and flight tested during the 1960-1969 period for the SERT II program. The EMT operates at a 3-kW power level with a specific impulse of 3,000 sec. By making minor modifications in the existing thruster design, extended performance at approximately 6-kW power level, 4,800-sec specific impulse, and 15,000-hr pre-wearout life (as required for a Halley's comet mission) was believed to be achievable at a low technical risk. This supposition was evaluated as part of this study.

In addition to the extended performance thruster, the key elements of the thrust system for this extended-performance application are the power management and control (PMaC) subsystem, the gimbal system, propellant storage and distribution system, thermal control, and supporting structure. The background of extensive development in power-processing technology for mercury ion thrusters and technology developments in the other areas were the basis for the high level of confidence that the required extended performance levels could be achieved.

B. SCOPE

The scope of this study included: the development of conceptual designs for various candidate systems; the selection, definition, and evaluation of a baseline design concept and its critical interfaces; an evaluation of the sensitivity of the baseline design to critical data base and design parameters; the generation of a development program plan for the baseline concept; estimation of costs and fiscal year funding requirements; fabrication of a demonstration scale model; and the conduct of supporting technology studies (including fabrication and testing of critical hardware components) to estimate the physical and electrical performance and to provide a baseline for subsequent work.

The design characteristics, program plan, and costs of the baseline system were defined in parallel with the supporting technology effort. Design definition was carried out in two consecutive phases:

- Phase 1: Definition and comparison of alternate configurations, leading to baseline selection
- Phase 2: Design definition and evaluation of the baseline configuration, culminating in the generation of a program plan and cost estimates.

The evaluation of supporting thruster technology consisted of three essentially independent investigations to confirm the critical assumptions made during the design study in the following areas:

- Operation and documentation of a modified 900-series EMT at the beam voltage and power levels required for a Halley's comet mission

- Design and evaluation of thruster propellant electrical isolators for operation at beam voltages up to 4,000 V
- Development of a model for the charge-exchange plasma efflux from the ion beam exhaust plume (for analysis of interactions between the thrust system and a solar array operated at high voltage).

The program schedule, which required that the results of the completed study be reported during July 1977, determined the approach and scope of the thrust system design study and of the supporting studies. Much of the design study was therefore limited to conceptual definition of the key characteristics of subsystems and components, with just enough detail included to permit realistic estimates of mass, power dissipation, and reliability. Similarly, we sought to confirm the technology approaches in question by using straightforward engineering extrapolations of existing data or hardware designs, and the scope of the study was quite limited.

The fewest possible modifications were made to the 900-series EMT and evaluated. The high-voltage isolator design study was based on already proven approaches; and the charge-exchange plasma model was based on data available from previous ion beam measurement and theoretical analyses. Since the intent was to evaluate feasibility, conclusive verification of any specific design is not implied. Although the thruster technology areas do relate directly to the design studies described in Volumes I, II, and III, the results are presented here, in a separate volume, because those areas were investigated independently.

SECTION 2

MODIFICATION AND EVALUATION OF THE 900-SERIES 30-cm EMT FOR EXTENDED-PERFORMANCE OPERATION

Recent developments in the technology of thin solar cells, innovative solar array designs, and advanced technology ion thruster development have made feasible energetic missions such as the Halley's comet rendezvous. These high-energy-requirement missions, which require propulsion system specific masses of 10 to 25 kg/kW, would use the launch capabilities of the Space Shuttle's intermediate upper stage (IUS) combined with solar electric propulsion employing 30-cm diameter electron-bombardment mercury ion thrusters. The 900-series 30-cm EMT, developed for primary propulsion applications, is now close to achieving flight hardware status. The EMT has been successfully operated and performance documented over a throttling range of 4:1;[1] it has a demonstrated lifetime of 10,000 hr (Ref.2). A mathematical model of this thruster was recently developed that describes the performance parameters and thrust correction factors with respect to the independent variables of beam current and beam voltage.

A. DEFINITION OF THE EXTENDED PERFORMANCE OPERATING RANGE AND THRUSTER REQUIREMENTS

The design conditions of the 30-cm EMT were selected early in its development program to satisfy the requirements of a typical baseline set of planetary and Earth orbital missions using the solar array and power conditioning technology (resulting in a propulsion system specific mass, α, of 50 kg/kW) that was available at that time. The specific impulse design point of the 30-cm EMT is 3,000 sec, which corresponds to a beam voltage of 1,100 V. At this voltage, a thrust level of 128 mN is produced when operating at the beam current design point of 2 A.

The propulsion system specific mass of 10 to 25 kg/kW, a solar array power of 50 to 100 kW, and other Halley's comet mission requirements dictate the use of a thruster that has a higher power and specific impulse than does the present 900-series 30-cm EMT. Figure 1 presents thruster operating envelopes for the various power systems considered in

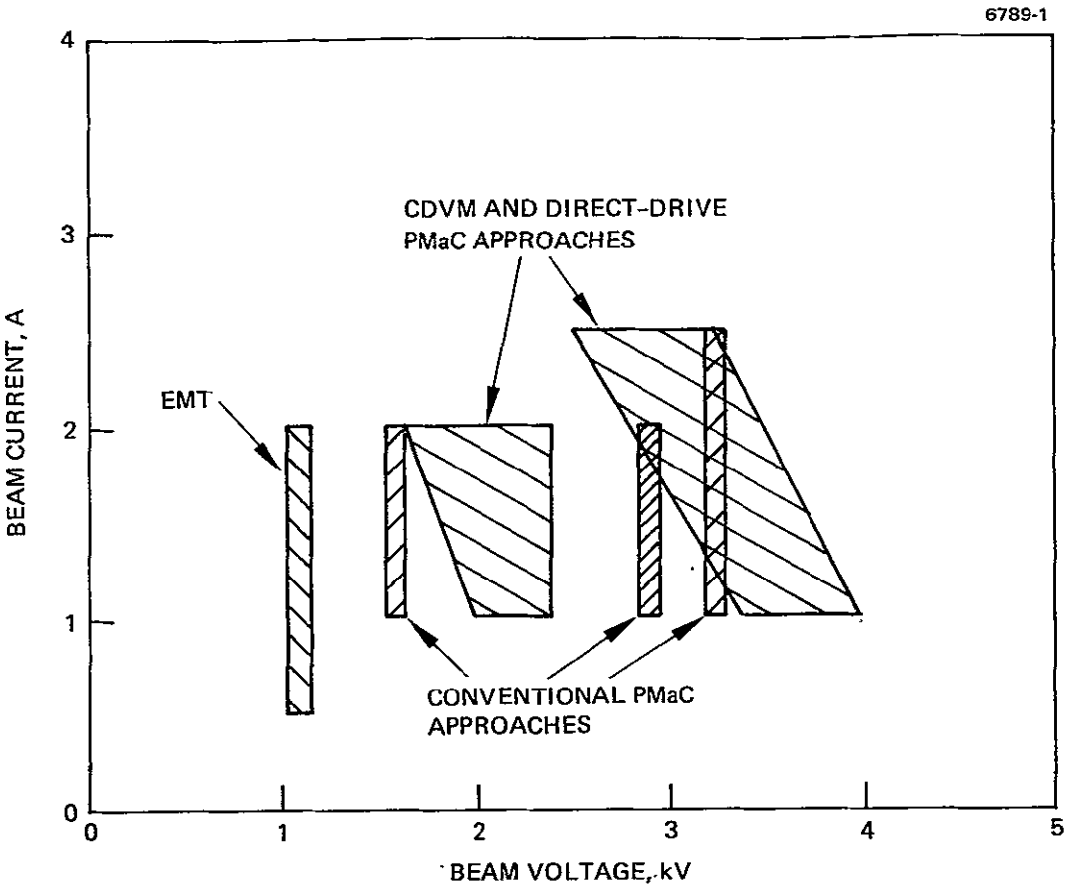

Figure 1. Thruster operating envelopes for various PMaC approaches proposed for the Halley's comet rendezvous.

the design study for the Halley's comet mission. Also shown is the operating range over which the 900-series EMT has been performance documented and mathematically modeled. The 900-series EMT does have the capability to operate below the beam voltage range shown in Figure 1. Comparing these envelopes illustrates how far some of the PMaC approaches considered depart from the basic EMT operating range. To operate the EMT in this extended performance range would require at least two modifications to the current design:

- Propellant isolator redesign or modification to permit thruster operation at high levels of beam voltage.
- An increase in the accelerator system gap to reflect the lower perveance requirements of the extended-performance thruster and to provide increased voltage standoff capability.

In addition, several factors peculiar to high-voltage thruster operation must be considered. These include the adequacy of wire insulation, protection of insulator surfaces, and close examination of threaded parts and sharp edges on insulator shields.

Preliminary verification and documentation of thruster operation at high power levels was accomplished under NASA contract NAS 3-19703 (Ref. 3). During that program, high beam current performance tests were conducted over a beam current range of 2 to 4 A with a nominal beam voltage of 1,100 V. Performance at high beam voltage levels was documented over a voltage range from 2 to 5 kV while maintaining a 2-A beam current. The test performance results were in agreement with predictions. The major conclusions from these preliminary studies were that

- High-voltage operation has no discernible effect on discharge chamber wear rates, but requires adequate electrical insulation.
- High-current operation increases the discharge chamber wear rate (and shortens thruster lifetime as a consequence).

Although those preliminary tests verified that the 30-cm EMT could be operated in the extended-performance range with relatively few modifications, performance data was still needed for a much broader operating range, as indicated in Figure 1. This documentation was obtained

under the test program described here. The primary objectives of the investigation were to:

- Verify that the modified EMT can be operated throughout the performance envelopes representative of the Halley's comet rendezvous mission
- Assess the applicability of the EMT performance model in the increased beam current and beam voltage ranges.

Experimental evaluation of the extended-performance thruster included:

- Performance documentation
- Measurement of propellant utilization and thrust correction factors
- Measurement of beam cone angle
- Determination of discharge chamber and screen grid erosion rates
- Measurement of various thruster component temperatures.

B. THRUSTER AND TEST FACILITY DESCRIPTIONS

To operate the 30-cm EMT at beam voltage levels representative of the Halley's comet rendezvous mission required that the thruster modifications discussed in the previous section be made. The modified thruster used during the test program, the vacuum test facility, and laboratory power system are described in Sections 2.B.1 and 2.B.2.

1. Thruster

Figure 2 is a photograph of the extended-performance thruster (SN 801) used during the test program. This thruster is an 800-series thruster modified to include all the components from the 900 series that were expected to affect thruster lifetime and performance characteristics. These modifications included:

- Flake control treatment of various discharge chamber surfaces

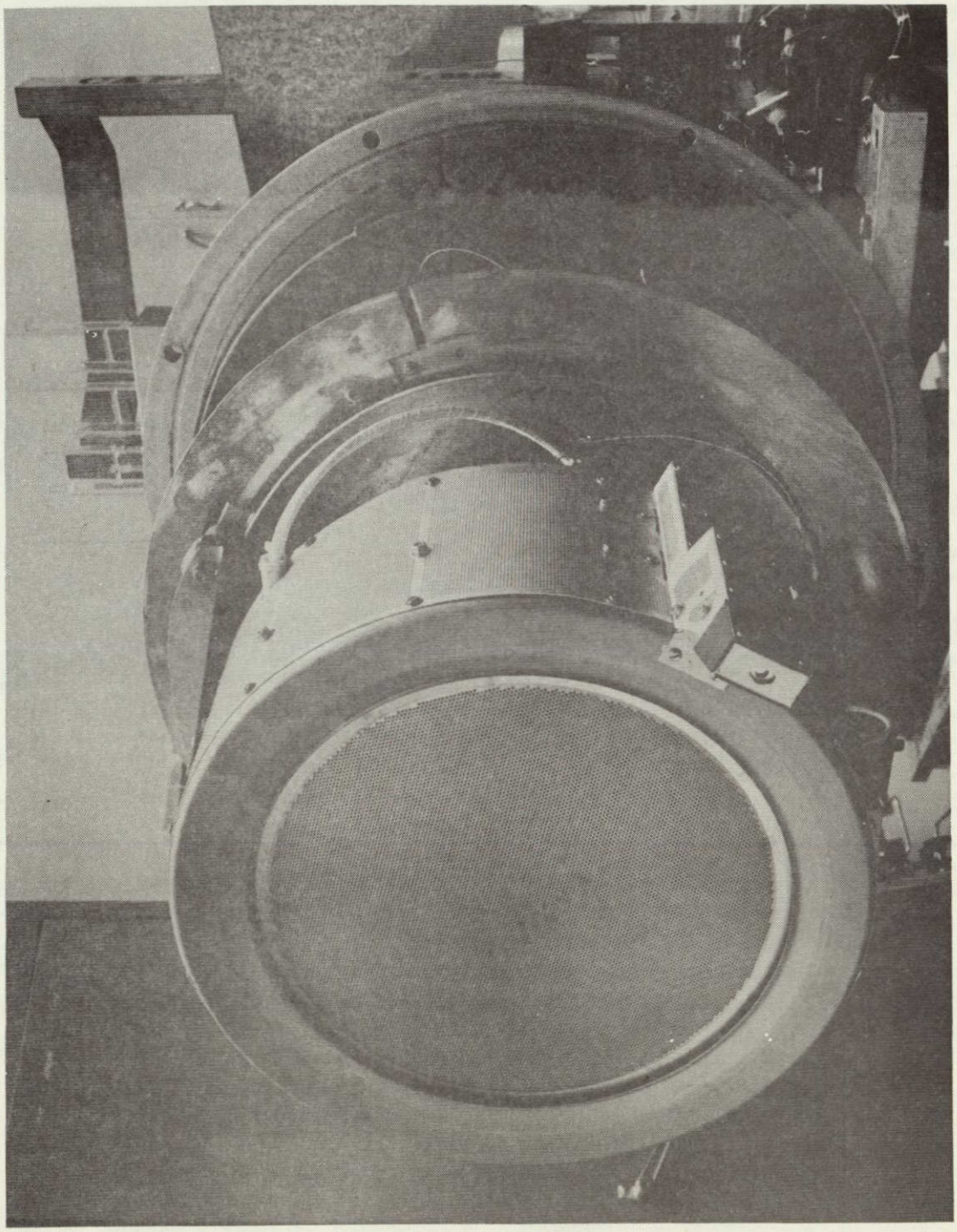

Figure 2. Photograph of thruster SN 801 modified for extended performance testing.

- Erosion control treatment of selected discharge-chamber and neutralizer surfaces
- 400-series thruster design baffle mount
- Swaged-type cathode heaters
- Impregnated porous tungsten cathode inserts
- A separable-type (cathode from vaporizer) neutralizer assembly.

The flake control surface treatment consisted of a wire mesh covering on the anode and the upstream discharge chamber boundary. Erosion control treatment involved installing tantalum cladding on the cathode pole piece and baffle and applying thin graphite strips to the neutralizer housing. In addition to these modifications, insulated restraints were installed at various locations to prevent wires from contacting thruster structural members.

As discussed earlier, the reduced perveance requirements of the extended-performance thruster allows the grid separation to be increased, thereby providing an improved voltage standoff capability. The EMT perveance and the perveance requirements of the extended-performance thruster are indicated in Figure 3. The perveance requirements of both thrusters are dictated by the minimum total extraction voltage available at the 2-A beam current level; Figure 3 shows the minimum voltage to be about 700 V higher for the extended-performance thruster configurations. The increase in grid spacing corresponding to the line labelled "required perveance" in Figure 3 can be calculated by using the EMT grid separation of 0.5 mm (0.020 in.) and the total extraction voltages at the 2-A beam current level, and by assuming that the current is governed by space-charge-limited flow between planar electrodes. The grid separation calculated in this manner is 0.76 mm (0.030 in.). This is the nominal spacing used during the test program and represents a 25% reduction in the grid separation used in the preliminary high-voltage thruster tests.[3] Figure 4 presents the variation in measured grid separation for ion optics assembly SN 817, which was used during the present program. Under atmospheric conditions, applying grid voltages greater than 2,500 V produced arcing in the minimum grid separation region

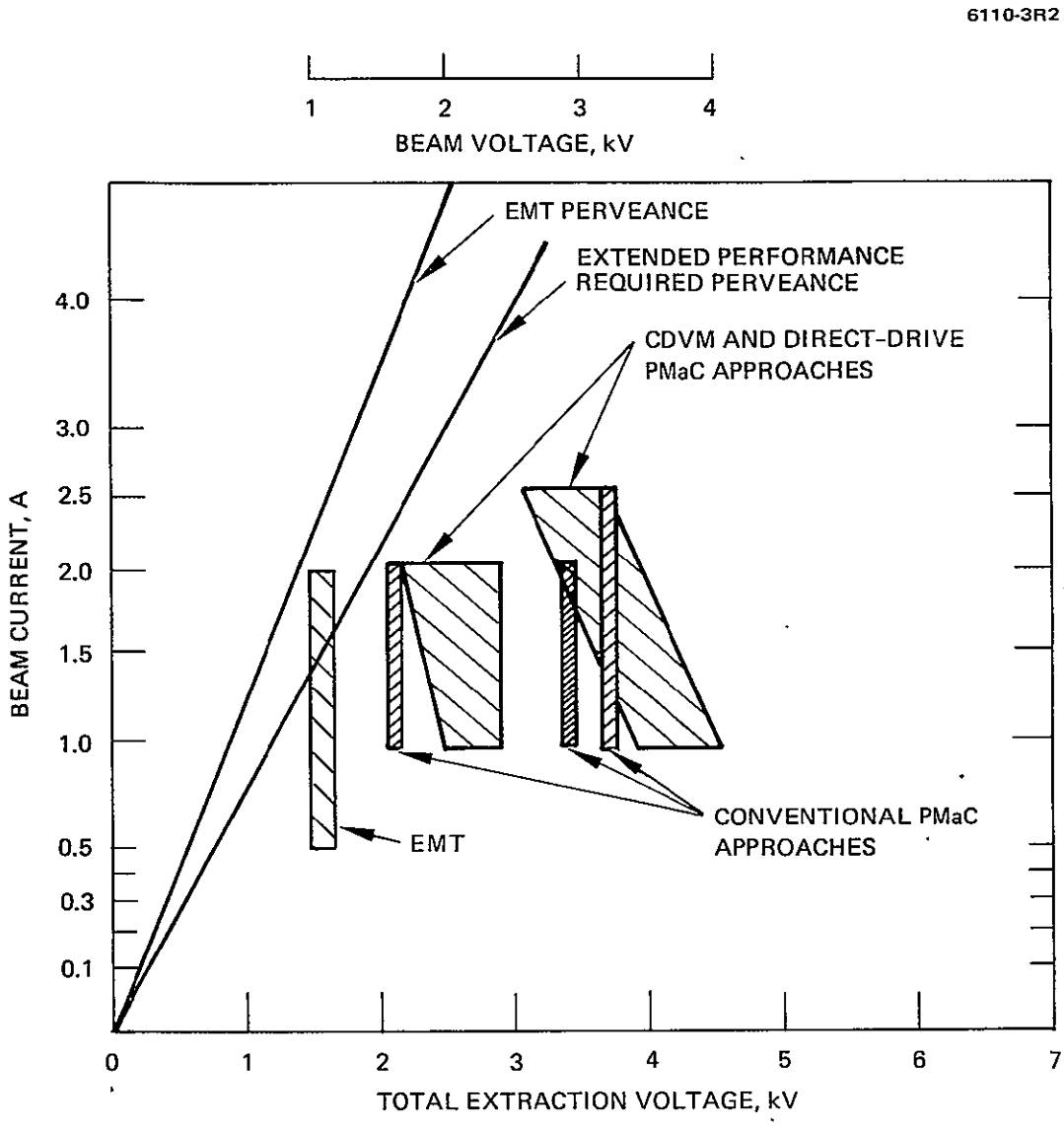

Figure 3. Thruster perveance requirements for different PMaC approaches.

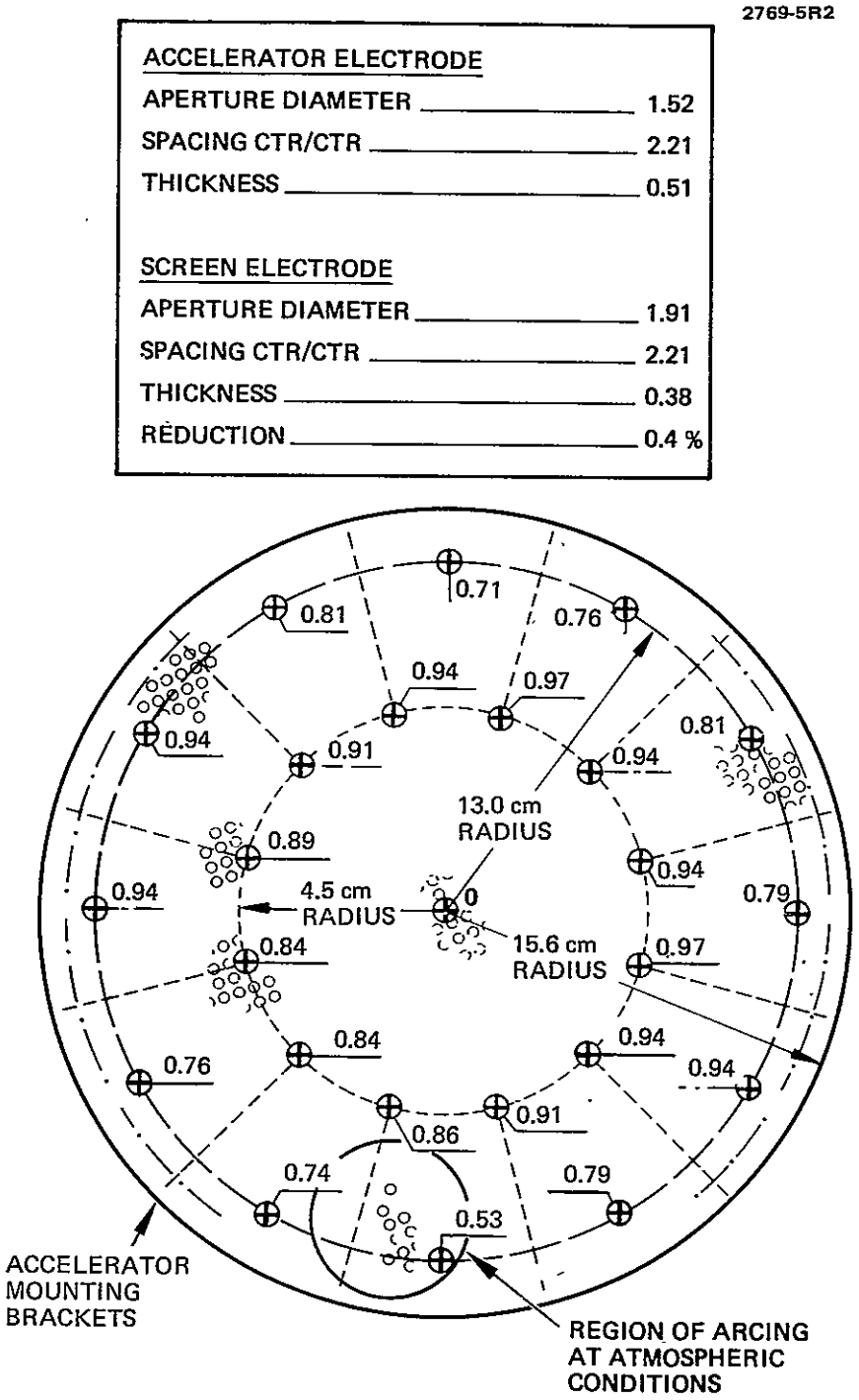

Figure 4. Electrode spacing chart for EMT grid design with nominal interelectrode spacing increased from 0.5 to 0.76 mm (dimensions are in mm except as noted).

indicated in the figure. However, before the thruster test program was begun, voltage standoff capability under high-vacuum conditions was demonstrated with applied voltages as high as 4,400 V.

One of the first tests conducted with the extended-performance thruster was to verify that the perveance and voltage standoff capability of the re-spaced ion optics were adequate for the extended performance operating envelopes shown in Figure 3. The figure shows that the perveance requirement is set by the operating point corresponding to beam conditions of 2 A and 1600 V (an accelerator voltage of 500 V was used in all tests). Perveance data was obtained at these conditions by reducing beam voltage while keeping discharge power and accelerator voltage constant. Figure 5 presents the measured variation of accelerator and beam currents with respect to total extraction voltage. The perveance line constructed from the measured variation in accelerator current, the EMT perveance line, and the required extended-performance thruster perveance lines are also shown in Figure 5. This data indicates that the perveance of the EMT optics, re-spaced to a separation of 0.76 mm, is more than adequate for operation in the performance envelopes characteristic of the Halley's comet mission. Subsequent testing of the extended-performance thruster verified the adequacy of high-voltage insulation and ion optics voltage standoff capability up to the 10-kW power level that corresponds to beam conditions of 2.5 A and 3,900 V.

2. Test Facility

The Hughes Research Laboratories (HRL) 2.7 m (9 ft) diameter vacuum facility was used for all thruster testing. The tank is cryopumped and has maintained ambient chamber pressure on the order of 10^{-6} Torr for ion beam power levels up to 10 kW and beam currents up to 4 A. Power to the various thruster components was provided by general-purpose laboratory-type supplies. These power supplies were adequate for thruster operation throughout the extended performance envelopes indicated in Figure 1. A block diagram of the thruster power system is presented in Figure 6.

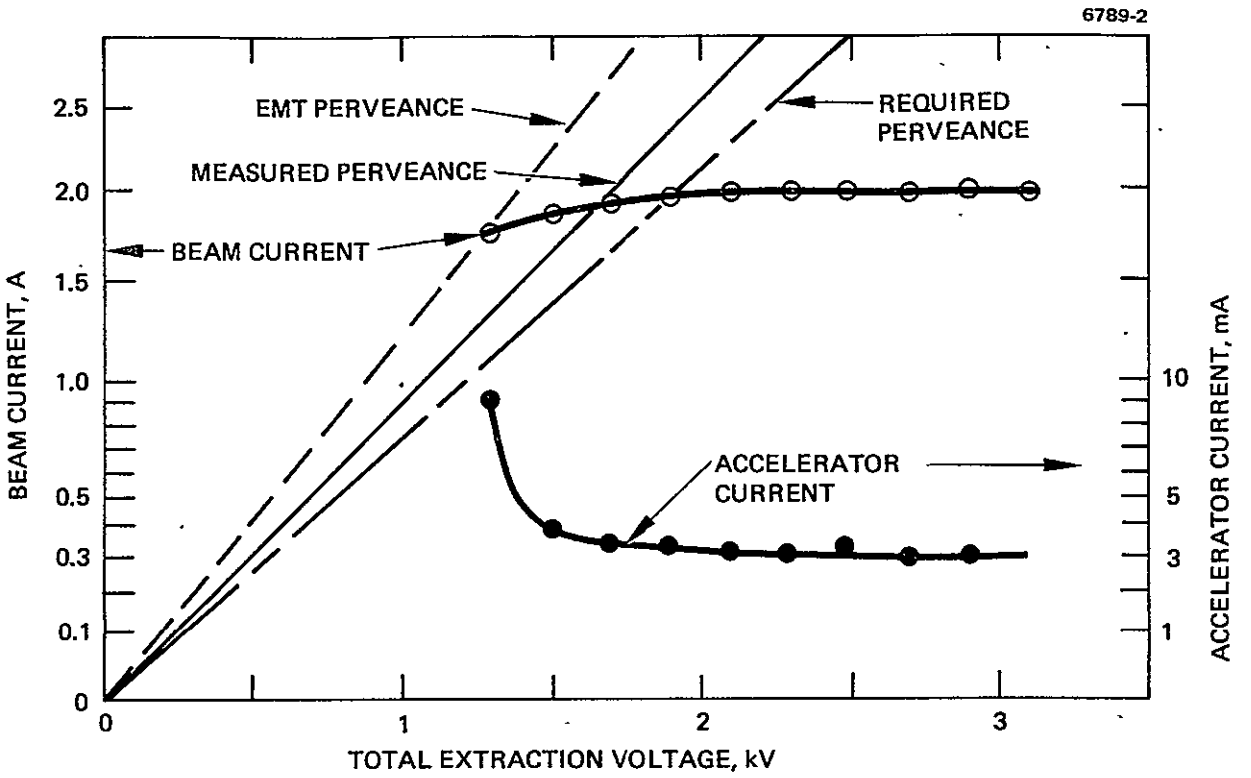

Figure 5. Perveance data for EMT grid design with interelectrode spacing increased to 0.76 mm.

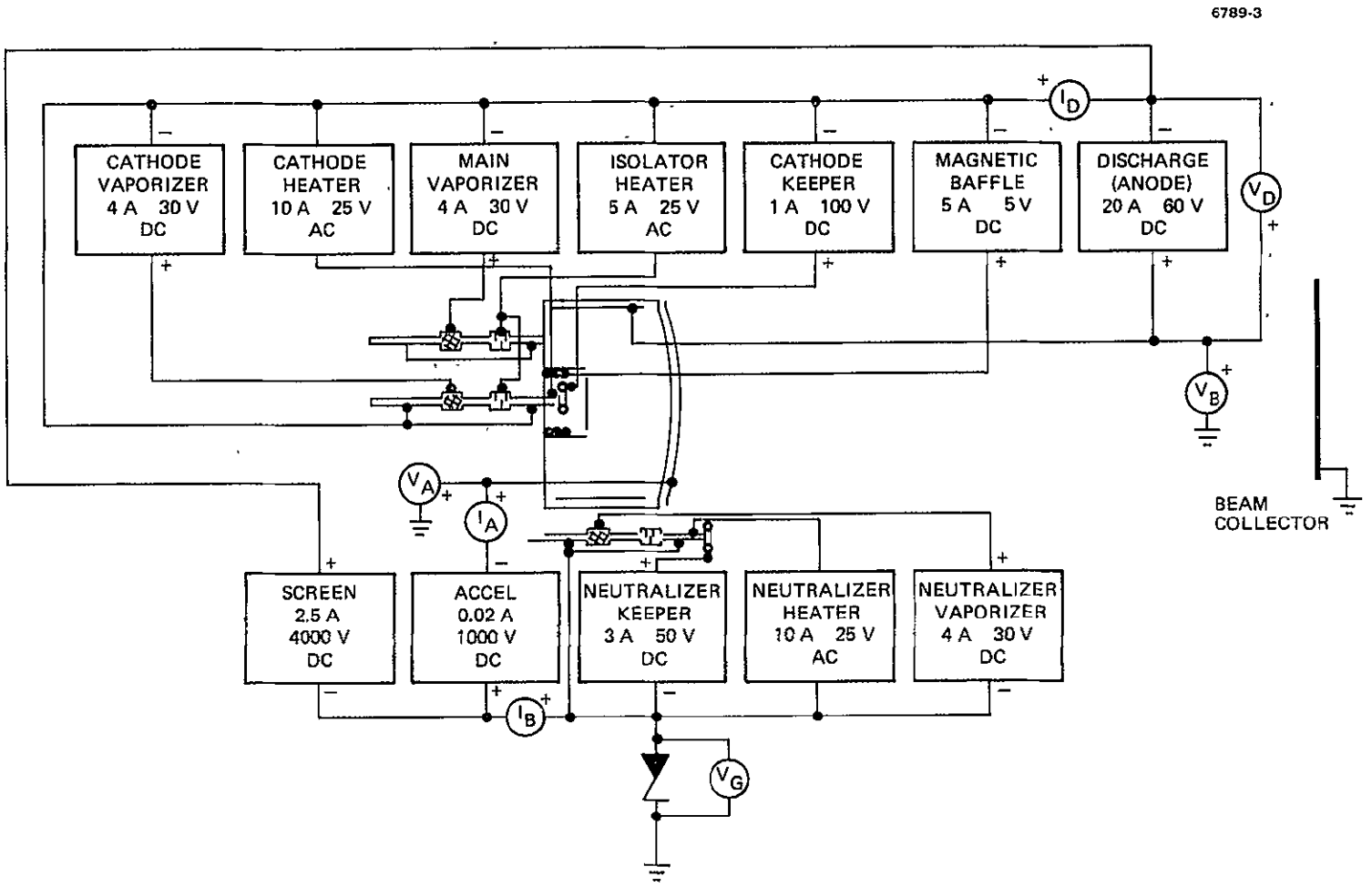

Figure 6. Block diagram of the power system of the extended-performance thruster.

The design and testing of high-voltage propellant isolators was done concurrently with the thruster testing program. This required short-circuiting the EMT cathode and main isolators to allow these propellant feed systems to float at thruster body potential. Consequently, the load cell flow measurement technique normally used for 30-cm thruster testing and documentation was not available for use under this program because the main and cathode feed systems were floated as high as 3.9 kV, which is beyond the isolation capability of the load cell instrumentation. Instead, the flow rates were determined by timing the fall of liquid mercury columns in calibrated glass pipettes.

In addition to providing power for the various thruster components, the power system assembled for this test program allowed certain operating parameters (such as beam current) to be held at a constant value. This was done by using current- or voltage-limited power supplies and closed-loop vaporizer control systems. Beam current was maintained at the desired value by controlling the main vaporizer current; the discharge and neutralizer keeper voltages were maintained at selected values by closed-loop control of the cathode and neutralizer vaporizer currents. The cathode and main vaporizer control loops were considered necessary to ensure that the data acquired would be accurate and repeatable for relatively short test times ($\leq$ 2 hr) and to maintain test parameters constant over longer periods (up to 30 hr) for tests using the $\vec{E} \times \vec{B}$ momentum analyzer probe and for erosion rate measurements.

C. SELECTION OF THRUSTER OPERATING PARAMETERS

The values of beam current and voltage selected for thruster performance documentation tests are representative of the operating envelopes required for the various PMaC approaches proposed for the

Halley's comet rendezvous mission. These envelopes and the operating points selected for the performance documentation tests are presented in Figure 7. The discharge parameters corresponding to the selected operating points are presented in Table 1. A discharge power loss of 200 eV/ion for these operating points was chosen because it would yield good propellant utilization at acceptable power levels. With the exception of some limited parameter variation testing, the discharge voltage was held constant at 36 V, which is a reasonable compromise between thruster efficiency and lifetime considerations.

An accelerator grid voltage of 500 V was chosen to eliminate electron backstreaming without causing excessive beam divergence. This choice was made on the basis of preliminary high-voltage thruster tests conducted under NASA Contract NAS 3-19703. These tests had revealed that thruster operation at beam voltages higher than 2 kV causes electron backstreaming if the absolute value of accelerator voltage is less than 400 V. Subsequent testing under the current program of the extended-performance thruster confirmed that the minimum accelerator grid voltage necessary to prevent electron backstreaming was 400 V. Cathode and neutralizer keeper currents of 0.8 and 2.0 A, respectively, were selected to be consistent with the current EMT operating conditions. The magnetic baffle current was set at either 2.2 or 2.7 A (approximately). The lower value corresponds to the minimum cathode flow rate required to prevent inefficient "low-mode" discharge-chamber operation; the higher value was selected to allow evaluating the effects of cathode flow rate on the thruster performance parameters.

D. TEST PROCEDURE

The thruster was operated at the desired conditions for approximately 3 hr after startup. By this time the starting transients had decayed, the tank pressure had reached the low 10^{-6} Torr range, and the accelerator grid current was typically less than 0.2% of the beam current. Propellant flow rate measurements were then started and continued for approximately 2 hr. These measurements consisted of

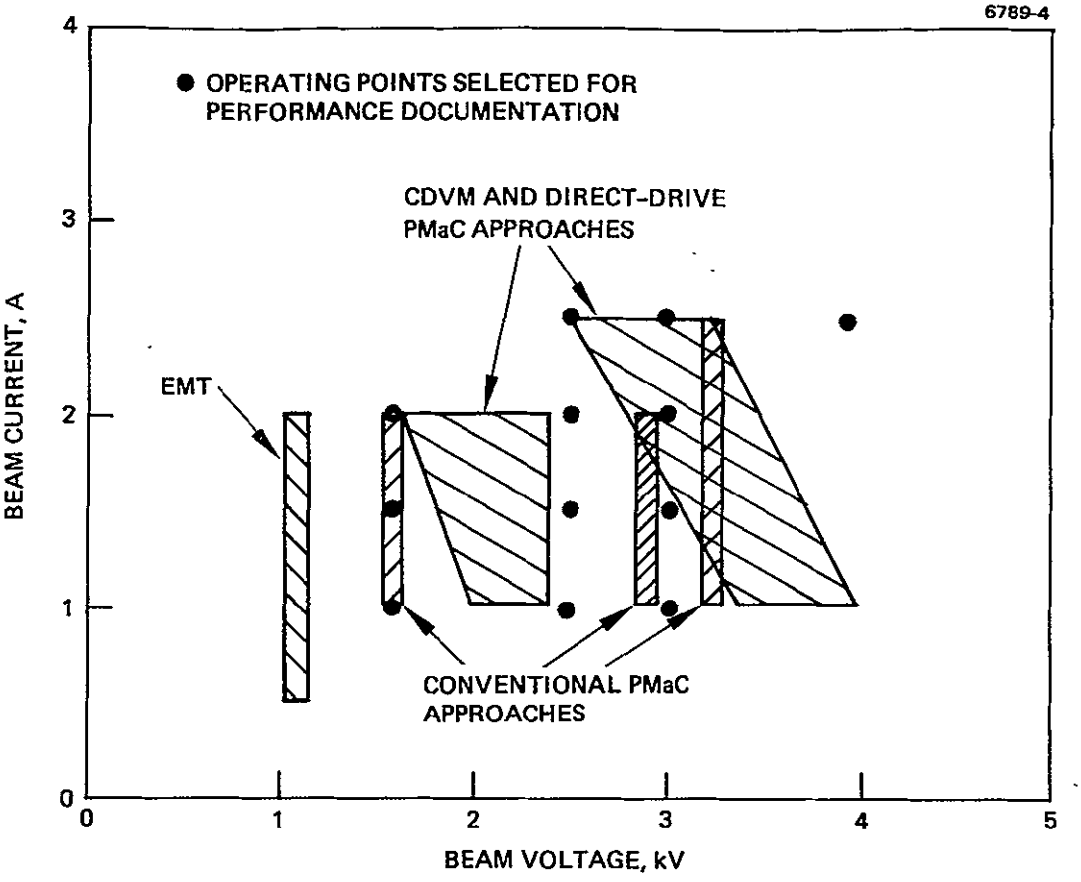

Figure 7. Thruster operating points selected for performance documentation.

Table 1. Operating Parameter Range for the Extended Performance Thruster

Beam		Discharge[a]	
I_B, A	V_B, kV	I_D, A	V_D, V
2.5	3.9	13.9	36
2.5	3.0	13.9	36
2.5	2.5	13.9	36
2.0	3.0	11.4	35
2.0	3.0	11.1	36
2.0	2.5	11.1	36
2.0	1.6	11.1	36
1.5	3.0	8.3	36
1.5	2.5	8.3	36
1.5	1.6	8.3	36
1.0	3.9	5.6	36
1.0	3.0	5.6	36
1.0	2.5	5.6	36
1.0	1.6	5.6	36

[a]200 eV/ion discharge loss

T5917

recording the height of a liquid mercury column at 10 min time intervals. The slope of the volume-versus-time curve plotted from this data was used to determine propellant flow rate. The plots were used to provide a visual indication of linearity and, hence, of steady-state flow conditions. After sampling flow data for approximately 2 hr, the flow rate for each vaporizer was calculated using linear least-squares regression. The correlation coefficient, which indicates the constancy of the flow rate during the data sampling period, was typically greater than 0.999.

Electrical measurements and tank pressure readings were also recorded at 10-min time intervals. Currents and voltages critical

to thruster performance calculations (discharge, beam, and accelerator) were measured using ±1% accuracy mirrored-scale panel meters. All other electrical quantities were measured using ±3% accuracy meters.

Beam diagnostic data was obtained using an $\vec{E} \times \vec{B}$ momentum analyzer probe.[4] This instrument was used to measure the positively charged constituents of the ion beam and to measure thrust losses due to beamlet divergence and the presence of multiply charged ions. Beam profiles were recorded using a single Faraday cup probe that was swept through the ion beam at various axial locations.

E. EXPERIMENTAL RESULTS

The thruster test program consisted of two basic tasks: performance documentation and assessment of thruster lifetime. Performance documentation involved determining thruster performance parameters (such as electrical and propellant utilization efficiencies) and measuring the efficiency correction factors (which correct for losses caused by beam divergence and the presence of multiply charged ions). The thruster lifetime investigation, which consisted of three types of tests, was conducted to enable assessing the effects of high-power thruster operation on thrust system lifetime. These tests included measurements of discharge chamber and screen grid erosion rates, beam cone angle,* and critical thruster component temperatures.

1. Performance Documentation

Performance testing consisted of obtaining flow rate, electrical, and beam diagnostic measurements at each of the beam conditions indicated in Figure 7. The performance parameters were calculated using the electrical measurements indicated in Figure 6 and the following expressions for total power

$$P_T = (I_B + I_A)(V_B - V_G) + (I_D + I_B + I_A)V_D \quad (1)$$
$$+ I_A V_A + \Sigma P_{misc} \ ,$$

*Cone angle is the angle of a conically shaped region that contains 95% of the primary ion beam ion current.

electrical efficiency

$$\eta_e = \frac{I_B V_B}{P_T} \quad , \tag{2}$$

propellant utilization efficiency

$$\eta_u = \frac{I_B}{\dot{m}_{TOTAL}} \tag{3}$$

and thruster efficiency

$$\eta_T = \eta_e \eta_u (\alpha F_t)^2 \quad , \tag{4}$$

where $\dot{m}_{TOTAL}$ is the total propellant flow rate expressed in equivalent amperes, and ΣP_{misc} represents the miscellaneous thruster input power (which consists of magnetic baffle, keeper, and vaporizer heater powers). The thrust correction required to account for the presence of doubly charged ions, α, and the thrust loss correction due to beamlet divergence, F_t, were calculated from the $\vec{E} \times \vec{B}$ probe measurements in the manner described in Ref. 4.

The calculated performance data is presented in Table 2. This performance data is compared with the values calculated using the EMT mathematical model in the following section. There are trends evident in the performance data that are not accounted for in the model, however, and these effects are discussed below.

a. Beam Voltage Effects

The propellant utilization data (Table 2) generally indicates that utilization increases with increasing beam voltage. This trend, which was also observed in the preliminary high-power thruster tests,[3] probably is a result of plasma sheath movement within the screen grid apertures. As beam voltage is increased with beam current held

Table 2. Thruster Performance Data for Extended-Performance Operations

Controlled Parameters[a]					Measured Parameters								Beam Diagnostics					
I_B, A	V_B, V	I_D, A	V_D, V	I_{MB}, A	I_A, mA	$\dot{m}_m$, A	$\dot{m}_c$, A	$\dot{m}_{TOTAL}$[b] A	P_{TOTAL},[a,b] W	η_e,[b] %	η_u,[b] %	η_t,[b] %	I^{++}/I^{+}, %	α	β	F_t	$\alpha^2 F_t^2$	J^{++}/J^{+}, %
1.0	1.6	5.6	36	2.3	2.4	1.147	0.082	1.259	1,877	85.2	79.4	62.2	8.4	0.981	0.961	0.977	0.919	0.14
1.0	1.6	5.6	36	3.0	1.8	1.096	0.106	1.232	1,886	87.8	81.2	63.0	8.9	0.980	0.959	0.976	0.915	0.21
1.0	2.5	5.6	36	2.3	2.3	1.156	0.086	1.272	2,778	90.0	78.6	65.0	7.9	0.982	0.963	0.976	0.919	0.15
1.0	2.5	5.6	36	3.0	1.7	1.109	0.106	1.245	2,787	89.7	80.3	65.6	8.2	0.981	0.962	0.973	0.911	0.19
1.0	3.0	5.6	36	2.3	2.4	1.140	0.088	1.250	3,279	91.5	80.0	66.8	8.0	0.982	0.963	0.973	0.913	0.16
1.0	3.6	5.6	36	2.8	1.4	1.075	0.115	1.220	3,285	91.3	82.0	68.2	9.2	0.979	0.958	0.975	0.911	0.15
1.0	3.9[b]	5.6	36	2.6	1.8	1.032	0.153	1.215	4,182	93.3	82.3	70.0	9.2	0.979	0.958	0.975	0.911	0.15
1.5	1.6	8.3	36	2.2	3.1	1.651	0.074	1.755	2,778	86.4	85.5	67.0	11.9	0.974	0.997	0.976	0.907	0.27
1.5	1.6	8.3	36	2.3	3.4	1.630	0.075	1.735	2,779	86.4	86.5	67.9	11.6	0.974	0.973	0.979	0.969	0.26
1.5	1.6	8.3	36	3.0	2.7	1.566	0.094	1.690	2,771	86.6	88.8	69.2	13.2	0.971	0.942	0.977	0.900	0.35
1.5	2.5	8.3	36	2.2	2.7	1.632	0.079	1.741	4,129	90.8	86.2	70.9	12.0	0.973	0.946	0.978	0.906	0.27
1.5	2.5	8.3	36	3.0	2.6	1.531	0.118	1.679	4,122	91.0	89.3	73.9	12.1	0.973	0.946	0.980	0.909	0.30
1.5	3.0	8.3	36	2.2	2.5	1.611	0.080	1.721	4,879	92.2	87.2	72.8	11 4	0 974	0.949	0.977	0.906	0.30
1.5	3.0	8.3	36	2.7	1.9	1.585	0.085	1.700	4,884	92.1	88.2	72.9	13.4	0.970	0.941	0.977	0.898	0.31
1.5	3.0	8.3	36	2.8	1.9	1.565	0.101	1.696	4.225	92.1	88.4	72.7	11.5	0.974	0.949	0.977	0.893	0.28
1.5	3.0	8.3	36	3.0	2.7	1.501	0.124	1.655	4,873	92.3	90.6	75.3	11.8	0.974	0.977	0.974	0.900	0.31
2.0	1.6	11.1	36	2.3	4.3	2.100	0.063	2.193	3,683	86.9	91.2	70.3	18.3	0.961	0.923	0.980	0.887	0.43
2.0	1.6	11.1	36	2.3	4.5	2.088	0.058	2.176	3,684	86.9	91.9	71.2	16.4	0.965	0.930	0.978	0.891	0.72
2.0	1.6	11.1	36	2.8	3.5	2.039	0.093	2.162	3,691	86.7	92.5	71.1	18.4	0.961	0.923	0.980	0.887	0.49
2.0	2.5	11.1	36	2.3	3.6	2.094	0.069	2.193	5,483	91.2	91.2	79.1	16.6	0.965	0.929	0.978	0.891	0.51
2.0	3.0	11.4	35	2.2	3.4	2.079	0.074	2.183	6,484	92.5	91.6	75.7	15.4	0.967	0.933	0.978	0.894	0.77
2.0	3.0	11.1	36	2.3	3.3	2.048	0.073	2.151	6,484	92.5	93.0	76.1	17.3	0.963	0.926	0.977	0.885	0.50
2.0	3.0	11.1	36	2.7	2.6	2.016	0 108	2.154	6,491	92.4	92.9	75.5	19.5	0.959	0.918	0.978	0.880	0.51
2.0	3.0	11.1	36	2.7	2.8	2.001	0.112	2.143	6,492	92.4	93.3	76.4	17.7	0.962	0.925	0.489	0.885	0.48
2.0	3.0	11.1	36	2.7	2.4	1.977	0.113	2.120	6,490	92.4	94.3	76.8	19.0	0.960	0.920	0.978	0.881	0.50
2.5	2.5	13.9	36	2.2	4.4	2.467	0.078	2.575	6,842	91.4	97.1	76.6	24.5	0.951	0.902	0.977	0.863	0.74
2.5	3.0	13.9	36	2.2	4.1	2,451	0.088	2,569	8,092	92.7	97.3	77.4	24.4	0.951	0.902	0.974	0.858	0.70
2.5	3.9[c]	13.9	36	2.7	3.4	2.336	0.119	2.485	10,347	94.2	100.6	81.3	24.4	0.951	0.912	0.974	0.858	0.70

[a] Accelerator voltage V_A was 500 V.

[b] Assumes V_{NK} = 13.8 V, I_{NK} = 1.8 A, V_G = 10 V, neutralizer flow rate = 0.030 A.

[c] Beam diagnostic data was obtained at 3 kV beam voltage.

T5917

constant, the plasma sheath moves upstream, which reduces ion loss to the screen aperture walls and increases the effective open area of the screen grid. These effects permit discharge operation at a lower plasma density, which implies lower neutral density and increased propellant utilization at a fixed beam current level.

b. Magnetic Baffle Current Effects

Reducing the magnetic baffle current and the cathode flow rate proportionately generally improved the performance of the discharge chamber. Improved performance at low cathode flow conditions is apparently a consequence of fewer neutrals passing through the baffle aperture region. This permits a larger fraction of the electrons drawn from the cathode discharge plasma to attain an energy corresponding to the potential difference between the cathode and main plasmas, which results in an increase in the ionization cross section and more efficient thruster operation. However, a lower limit on cathode flow rate exists since very low cathode flows generally result in an inefficient mode of discharge operation (sometimes referred to as "low mode"), characterized by poor propellant utilization efficiency.

Table 2 presents thruster performance data for both low and high magnetic baffle currents (approximately 2.2 and 2.7 A), corresponding to cathode flow rates in the range from 60 to 150 mA. This data shows a consistent trend towards more efficient thruster operation at higher cathode flow rates. This is shown by the increase in propellant utilization and total thruster efficiency which accompanied increased cathode flows. The increase in propellant utilization at constant beam current generally reduced accelerator drain current and (presumably) erosion of the accelerator grid caused by charge-exchange ion impingement.

The reason for the performance improvement that was observed at higher cathode flow rates is not well understood. A complete understanding would require acquiring plasma diagnostic and magnetic field geometry information, and this was beyond the scope of this program.

Lacking this data, all that can be said is that the extended-performance thruster may be operationally different from the unmodified 900-series EMT in this respect. If such a difference exists, it would need to be determined whether it is caused by plasma, geometric, or magnetic-field effects. Efficient and stable thruster operation at higher cathode flow rates is considered a desirable characteristic since it would provide a wider margin for flow variation above the low-mode lower limit on cathode flow rate.

c. High Power Operation

The performance data in Table 2 indicates that electrical efficiency is higher when operating at higher power levels. This occurs because the discharge and miscellaneous fixed power losses become smaller fractions of the total thruster power as the beam power is increased. As discussed earlier, operation at increased beam voltages with beam current held constant increases propellant utilization efficiency. Also, at a fixed beam voltage, the propellant utilization efficiency increases with beam current level. The increase in propellant utilization with beam current is expected since thruster operation at the 200 eV/ion discharge power level generally results in a constant neutral loss rate.[5]

d. Discharge Voltage Reduction

Lowering the discharge voltage level to 35 V reduces propellant utilization and the ratio of double-to-single ions. The combination of reduced plasma potential (ion energy) and double ion density achieved through discharge voltage reductions is considered an effective means for increasing thruster lifetime. However, the lowered discharge voltage reduces the cross sections for the formation of both single and double ions. This results in a loss in propellant utilization efficiency. Acceptable propellant utilization efficiency may be maintained only if the neutral density is increased to offset any reduction ion ion production rate.

An acceptable neutral loss rate can be maintained at the increased neutral density by reducing the open area of the accelerator grid. The use of small-hole accelerator grid (SHAG) optics for obtaining good thruster performance at low discharge voltage levels was demonstrated under a previous program.[3] No effort was made during the current program to verify the effectiveness of SHAG optics in improving thruster lifetime.

2. Thruster Lifetime

Three types of tests were conducted to assess the lifetime capabilities of the extended-performance thruster:

- Beam divergence angle measurements for use in assessing the compatibility of the thruster and the solar array and defining this interface requirement.
- Temperature measurements of various thruster components for determining the effects of high-power thruster operation on local temperatures near critical areas (such as propellant isolators, wire insulation, and braze joints).
- Erosion rate measurements on critical thruster components (such as the screen and accelerator grids, pole piece, baffle, and baffle supports).

The results of these tests are discussed separately below.

a. Beam Divergence

The primary ion beam cone angle was determined by sweeping a Faraday probe through the beam while simultaneously recording probe position and collector current. These measurements were made at axial locations 10 and 20 cm downstream from the accelerator grid; the beam current that was obtained by integrating the current density profiles measured with the Faraday probe generally agreed with the metered beam current to within ±5%.

The radial position at which the current density drops to zero can be used to define the beam edge, although this method of defining the beam edge is considered somewhat inaccurate because of the

detection threshold and finite collection area of the Faraday probe. An alternate and perhaps more meaningful procedure is to define the beam edge as that radius which contains a large fraction (say 95%) of the total primary ion beam. This approach reduces any error introduced by the detection threshold of the probe, since the "tail" of the current density profile contributes a relatively small amount to the beam current integral.

Beam cone angles obtained from the Faraday probe measurements are presented in Figure 8 as a function of beam current. The angles were calculated using the beam radius at a known axial location, and a beam radius at the thruster exit plane of 14.5 cm. The variation of beam cone angle with beam voltage was found to be negligible, which is not surprising since the net-to-total beam voltage ratio, R, remained relatively constant. Figure 8 indicates that a 20^{o} cone contains 95% of the primary beam ions and that this value is essentially independent of beam conditions. The beam cone angles calculated from the radius at which the Faraday probe signal drops below measurement threshold (less than 6 $\mu A/cm^2$) is also shown in Figure 8; this data suggests a maximum beam cone angle of approximately 40°. The absolute beam edge determined in this manner is considered optimistic, since recording the Faraday probe output on a more sensitive current indicator would tend to increase the calculated radius at which the signal drops below the measurement threshold. Based on probe measurements made using more sensitive current scales, the error in absolute beam edge is estimated to be within +8°.

An alternate and more accurate procedure for determining the absolute beam edge was accomplished through the use of alternating-film erosion monitors.* These monitors were attached to the neutralizer housing, from which an unobstructed view of the primary ion beam edge was provided. This technique accurately defines the beam edge by

*A complete description of the alternating-film erosion monitor technique is presented later in this section.

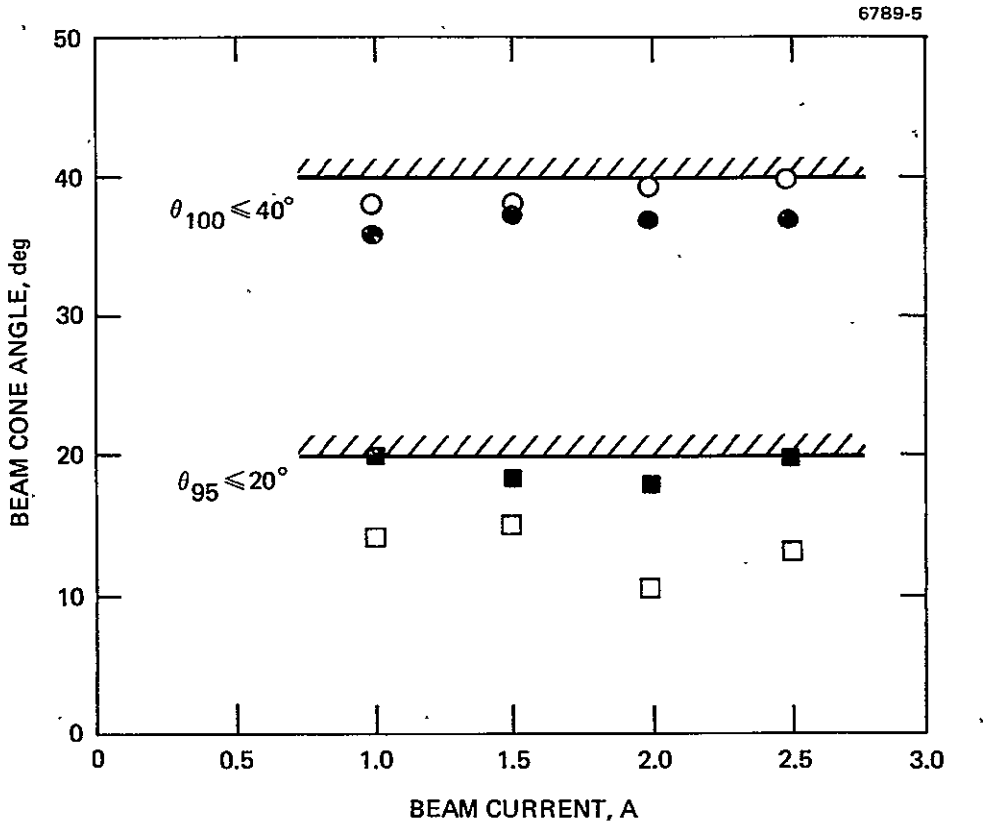

BEAM CONE ANGLE vs BEAM CURRENT

SYMBOL	% I_B	LOCATION, cm
○	100	10
◉	100	20
□	95	10
■	95	20

Figure 8. Measured beam cone angles.

determining the axial location on the neutralizer housing upstream of which no sputtering damage occurs. Beam cone angles determined in this manner are presented in Table 3. This data indicates that the beam cone angle is $\approx 50^{o}$ and is independent of beam current. An increase in the beam cone angle of approximately 1^{o} was observed at the lower beam voltage, and this increase in beam divergence was apparently due to the reduction in the net-to-total beam voltage ratio, R.

Beam divergence angles determined using the erosion monitors have an estimated accuracy of $\pm 1^{o}$, with the bulk of the error caused by errors in geometric measurements. Comparison of the absolute beam cone angles determined by the Faraday probe and erosion monitor techniques indicates agreement to within 2^{o} when the error in the Faraday probe method is accounted for.

b. Temperature Measurements

Thruster component temperatures were measured using Chromel-Alumel thermocouples attached at the critical locations indicated in Figure 9. After several hours of thruster operation at the 6.5-kW power level (2-A, 3000-V beam conditions), the indicated temperatures were recorded using a digital thermocouple meter. These measurements are in good agreement with thermal data obtained during preliminary high-power thruster testing at the 5-kW beam power level.[3] The temperatures recorded at the 6.5-kW power level are only 40 to 50^{o}C higher than those corresponding to EMT operation at 2.5 kW and are considered to be within the acceptable temperature range of these components.

c. Erosion Rate Measurements

The erosion rates of critical thruster components were measured at various thruster operating conditions using the multilayer erosion monitor technique[3] developed under previous NASA and COMSAT contracts. The thruster components selected for erosion rate

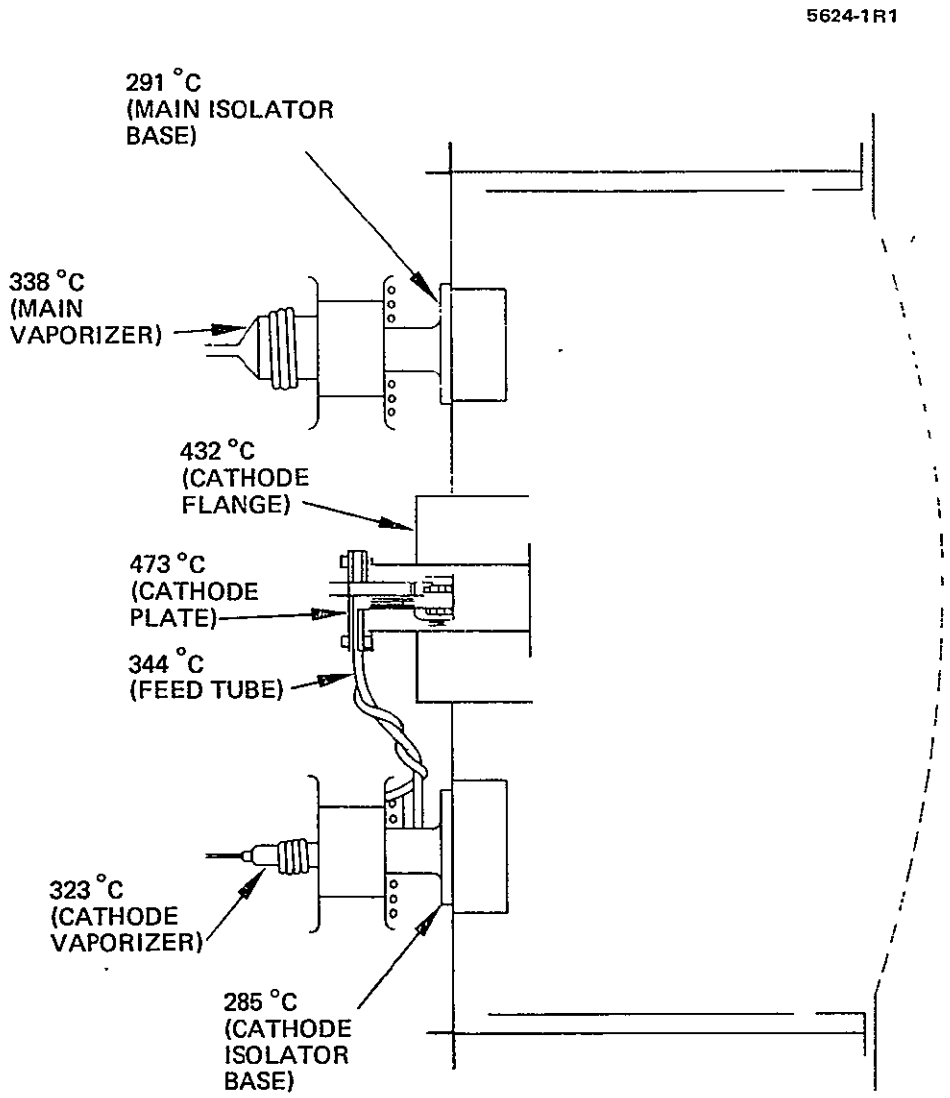

Figure 9. Schematic of thruster discharge chamber showing thermocouple locations and measured temperatures corresponding to 2-A, 3-kV beam conditions.

Table 3. Beam Cone Angles Determined from Alternating-Film Erosion Monitor Measurements

I_B, A	V_B, kV	θ, deg	R[a]
1.0	3.0	50.5	0.86
1.5	3.0	50.4	0.86
2.0	3.0	50.1	0.86
2.0	1.6	51.4	0.76

[a] R ≡ ratio of the net-to-total accelerating voltages

T5917

measurements included the screen and accelerator grids, baffle and support, cathode pole piece, and neutralizer housing.

d. Erosion Monitor Description

The multilayer erosion monitors, which are prepared in the Sputtering Processes Laboratory at HRL, consist of alternating layers of color-contrasting materials (such as tantalum and copper, or molybdenum and copper) that are sputter-deposited on a tantalum or stainless-steel substrate. Layer thickness is carefully controlled during the application process by maintaining the sputtering ion beam voltage and current constant and by precisely timing the deposition. A small piece of polished material sputter-deposited during preparation of the multilayer monitor material is used for calibrating layer thickness using a surface profilometer. Typical layer thickness for erosion monitors produced and calibrated in this way is 60 ±0.6 nm for the usual deposition control conditions.

Multilayer monitors used inside the discharge chamber had 8 tantalum or molybdenum layers and 7 copper layers; the first layer (either tantalum or molybdenum) applied to the substrate was double thickness. Because copper erodes about 20 to 40 times faster than either molybdenum or tantalum, the copper layers are factored into the analysis as only a portion of a layer. Therefore, the total equivalent thickness

of a 15 layer (8 Ta or Mo plus 7 Cu layers) monitor having 60 nm layer thickness is approximately 566 nm of molybdenum or 553 nm of tantalum.

e. Test Procedure

Small pieces of the thin-film erosion monitor material were spot-welded to the thruster components selected for erosion measurements. A portion of the monitors mounted on all thruster components except the screen and accelerator grids was masked to aid in determining the number of layers that had been eroded during thruster operation. Those monitors mounted on the screen and accelerator grids were perforated, with the monitor hole pattern matching that of the screen grid. Photographs to show typical examples of the erosion monitors mounted on various thruster components are presented in Figure 10. A summary of the location, type, and thickness of the erosion monitors used during these tests is given in Table 4.

Several precautions were taken during the thruster erosion monitor testing to ensure valid data acquisition. Among these were careful control of the discharge chamber operating conditions by means of vaporizer control loops, and checks on the double ion content of the discharge chamber using the $\vec{E} \times \vec{B}$ probe. Test chamber vacuum conditions are crucial in obtaining valid erosion-rate measurements since the presence of adsorbed gases and surface contamination (from poorly controlled vacuum conditions) could substantially reduce the surface sputtering yield. Several procedures were followed during these tests to ensure accurate erosion rate data by carefully monitoring and controlling the vacuum chamber pressure. The control procedures included:

- Venting the vacuum tank with gaseous nitrogen before removing or installing the thruster
- Sufficient pumping after thruster installation to achieve chamber pressures in the low 10^{-6} Torr range without cryo-pumping.

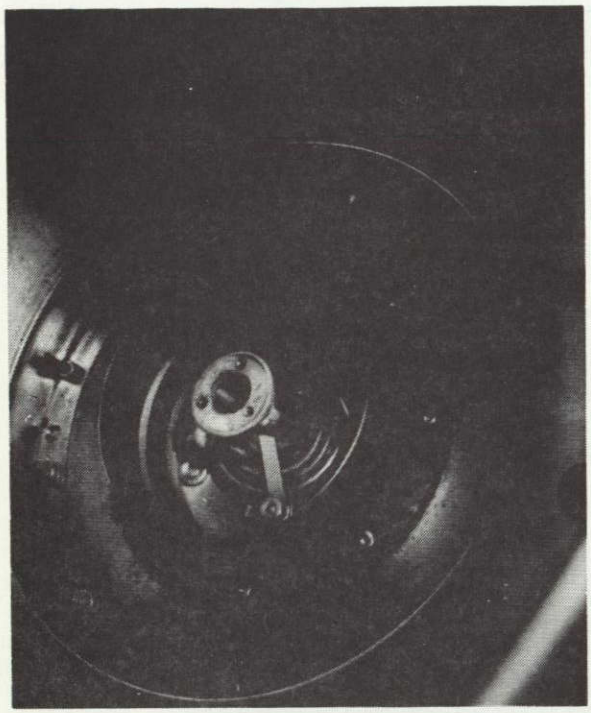

(a) BAFFLE SUPPORT

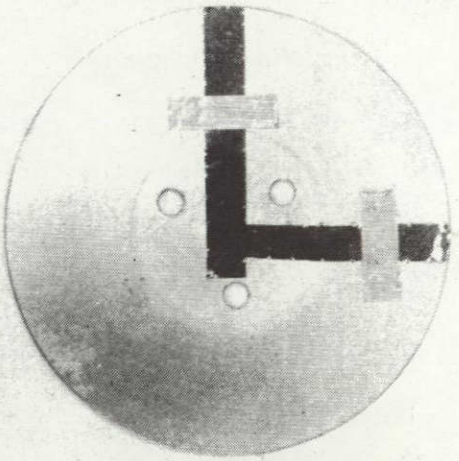

(b) BAFFLE, UPSTREAM SIDE

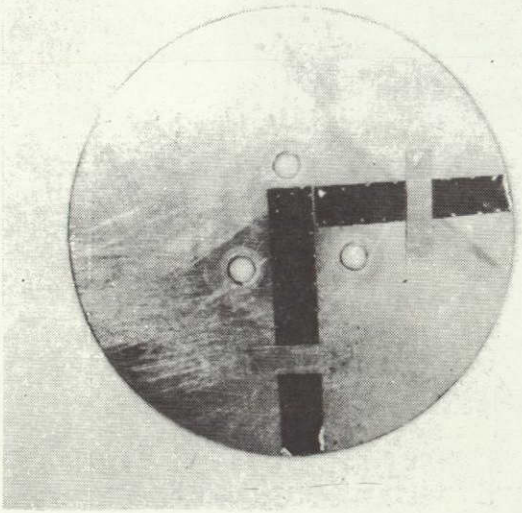

(c) BAFFLE, DOWNSTREAM SIDE

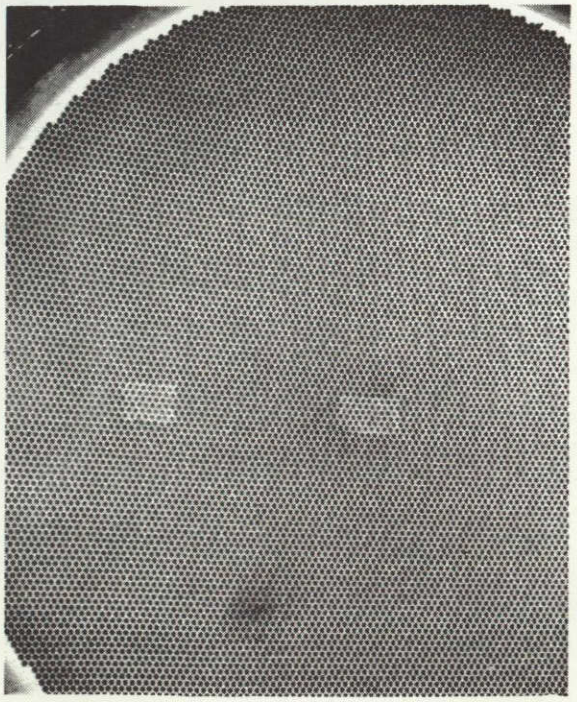

(d) SCREEN ELECTRODE, UPSTREAM SIDE

Figure 10. Photographs of multilayer erosions monitors mounted on internal thruster surfaces. (From Ref. 3.)

Table 4. Erosion Monitor Locations and Layer Description

Thruster Location	Monitor Material	Layer Thickness, nm	Number of Layers
Screen and accelerator grid	Mo and Cu	60	8 Mo + 7 Cu
Baffle, baffle support, cathode pole piece	Ta and Cu	60	8 Ta + 7 Cu
Neutralizer housing	Mo and Cu	150 (Mo) 200 (Cu)	14 Mo + 13 Cu

T5917

Vacuum chamber conditions were recorded periodically using ionization gauges located at the end of the chamber near the plane of the accelerator grid and at the chamber wall ≈ 2 m downstream from the thruster. The latter position is felt to be the most representative of the ambient vacuum chamber conditions. Figure 11 presents a time history of the vacuum chamber pressure recorded during a 14-hr erosion monitor test conducted at beam conditions of 1.5 A and 3000 V. After the beam voltage was applied, the tank pressure rose to the high 10^{-6} Torr range as a result of ion bombardment of the beam collector. After this initial pressure rise, the chamber pressure dropped to a low point of 3.5×10^{-8} Torr near the end of the 14-hr test.

f. Post-Test Data Analysis

Thruster operating times were scaled to remove several of the erosion monitor layers. After the tests, the monitors were removed from the various thruster components for analysis. To facilitate determining the number of layers removed, a "diagnostic etch" was performed on each monitor by ion-beam machining a groove through the remaining layers. By loosely positioning a mask above the surface, as shown in Figure 12, a tapered groove was machined to facilitate identifying layer interfaces at the boundary of the region masked during the test.

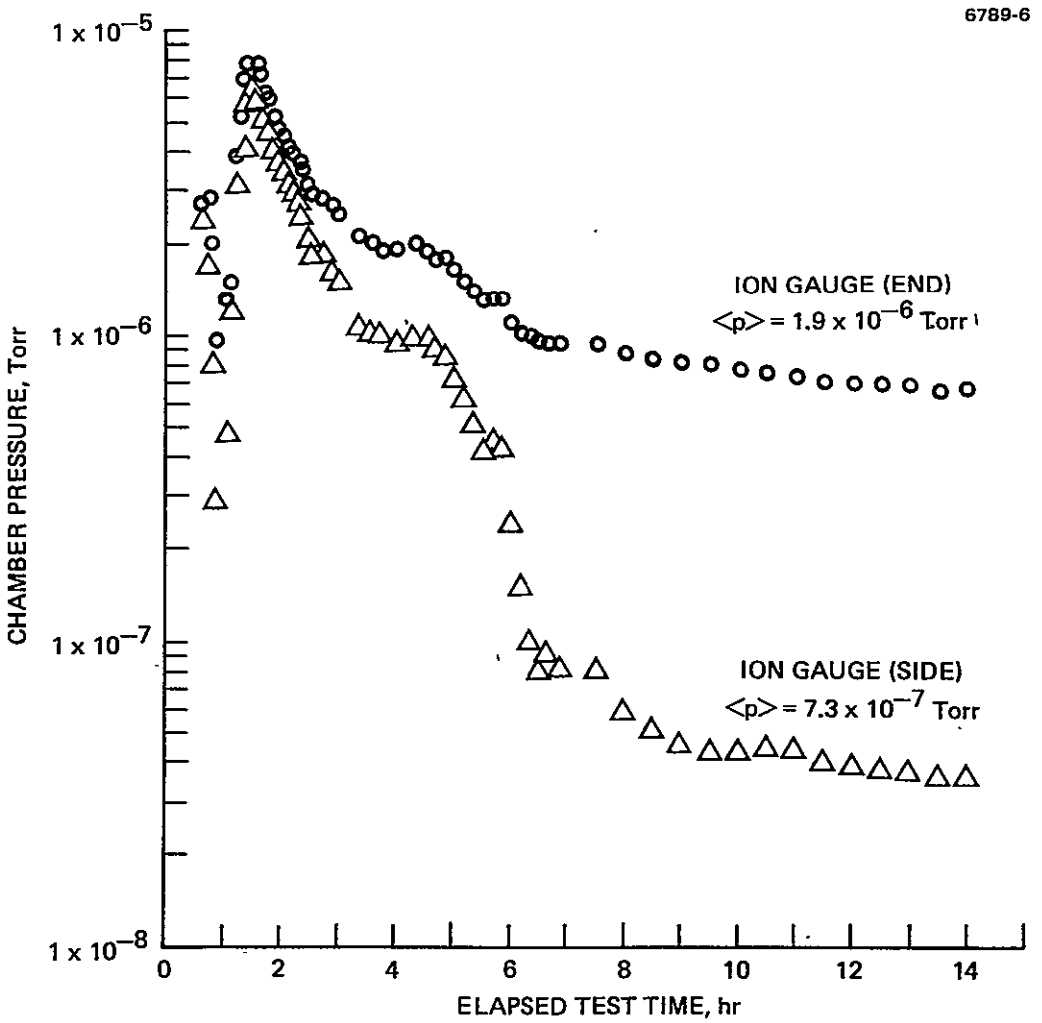

Figure 11. Vacuum chamber pressure variation during 14-hr erosion monitor test.

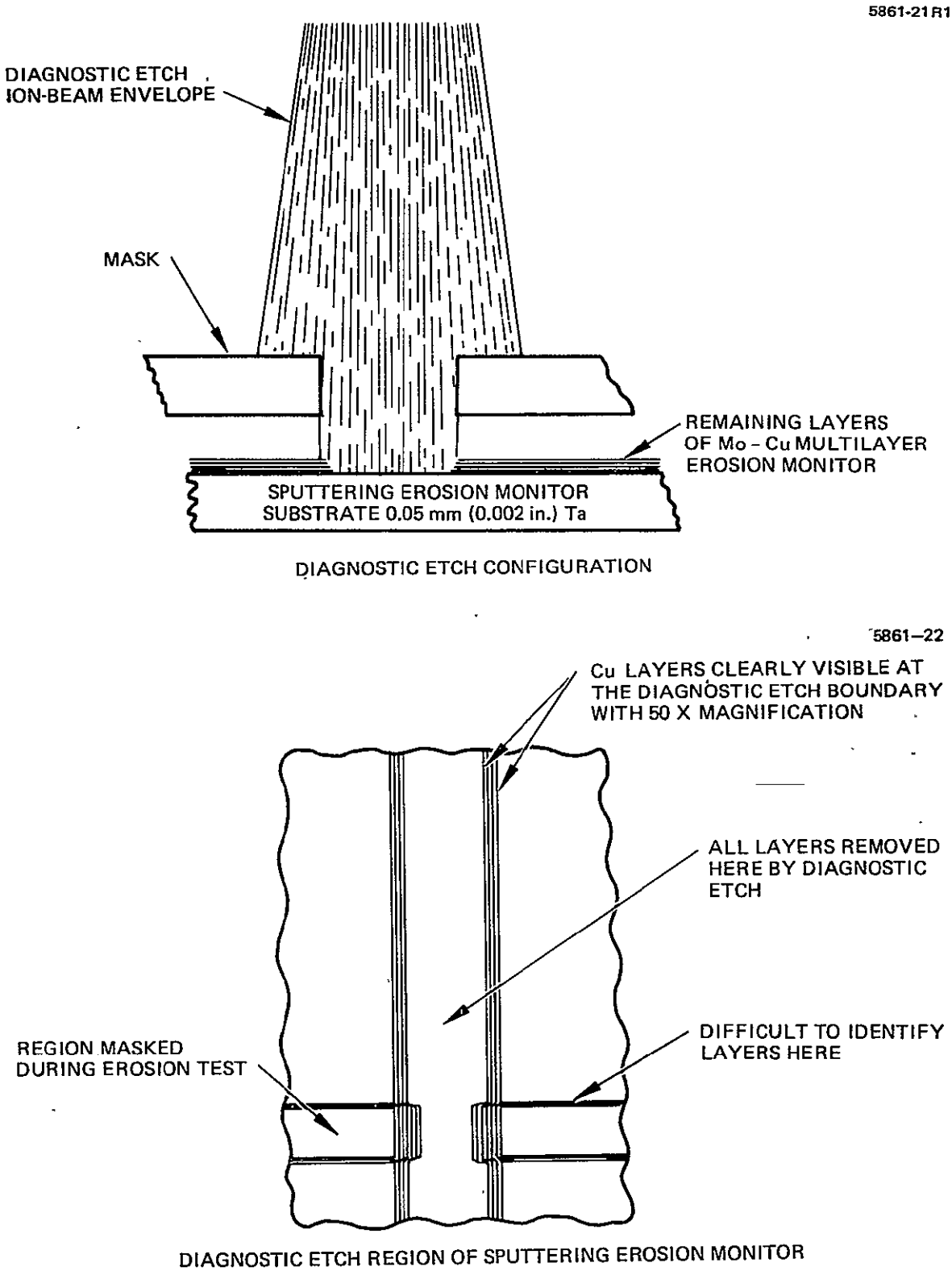

Figure 12. Diagnostic etch for erosion monitor analysis.

The erosion monitor layers, particularly those constructed with thin substrates, sometimes became blistered. Using thicker substrate material alleviated this problem somewhat by confining the blistering to regions near the edge of the baffle and at the tip of the cathode pole piece. This localization effect and the dependence on substrate thickness suggest that blistering may be caused by high temperatures. Blistering was observed only with monitors mounted on the baffle, baffle support, and cathode pole piece; none occurred with monitors mounted on the screen grid, accelerator grid, or neutralizer housing.

Once the number of copper layers remaining had been determined, the erosion rate, W, was calculated using the following expression:

$$W = [(N - N' + 0.5)\ \delta_{Ta,Mo} + (N - N')\ \delta_{Cu}/\gamma_{Ta,Mo}]/\tau\ , \qquad (5)$$

where N and N' are the initial and final number of copper layers, respectively; δ is the layer thickness; τ is the test time; and γ adjusts for the increased erosion rate of copper ($\gamma_{Ta} = 40$ and $\gamma_{Mo} = 20$). The first term in the numerator represents the thickness of eroded Ta or Mo, with the factor 0.5 introduced to account for the unknown fraction of the Ta or Mo layer remaining above the highest visible copper layer. Adopting this definition of the unknown remaining layer thickness, the uncertainty in the number of eroded layers is ±0.5. Thus the erosion rate uncertainty, U, can be expressed as

$$U_{Ta,Mo} = \pm\ \delta_{Ta,Mo}/2\tau\ . \qquad (6)$$

The second term in Eq. 5 accounts for the copper layers eroded, and the factor $1/\gamma$ converts copper layer thickness to equivalent tantalum or molybdenum layer thickness.

g. Results

Table 5 presents thruster wear rates calculated from the multilayer erosion monitor test results. The observed discharge

Table 5. Thruster Wear Rates Obtained from Alternating-Film Erosion Monitor Measurements

Parameters	Case 1	Case 2	Case 3	Case 4
Operating Conditions				
Beam current, A	2.0	2.0	1.5	1.0
Beam voltage, kV	1.6	3.0	3.0	3.0
Wear Rates, nm/hr				
Screen grid				
Center	52.3	52.3	20.7	2.6
Mid-radius	31.3	15.5	9.1	1.3
Accelerator grid				
Center	41.8	36.5	6.8	3.9
Mid-radius	15.5	15.5	6.8	1.3
Baffle				
Discharge side	76.8	66.5	33.8	19.2
Cathode side	5.0	5.5	6.7	3.8
Baffle support	15.3	15.3	6.7	3.8
Cathode pole piece	15.3	15.3	2.2	1.3
Neutralizer	167.5	115.8	107.9	61.3
Uncertainty[a]	±5	±5	±3.2	±1.3

[a]Neutralizer uncertainty 2.5 times the values shown.

T5917

chamber wear rates are relatively independent of beam voltage at the 2-A beam current level. The screen grid wear at the center of the grid was unaffected by the variation in beam voltage, and the accelerator grid wear rate at the center was lower at the higher beam voltage. This effect is consistent with the increase in propellant utilization and the decrease in accelerator grid drain current that was observed at higher beam voltages. The wear rates are strongly dependent on beam current, which is to be expected because both single and double ion densities within the discharge chamber increase with beam current.

Multilayer erosion monitors attached to the downstream side of the accelerator grid indicated that the charge-exchange ion erosion pattern was asymmetric with respect to the accelerator grid hole pattern. An indication of poor beamlet compensation was also evident in the angular dispersion data obtained from the $\vec{E} \times \vec{B}$ momentum analyzer. This is illustrated in Figure 13, which shows the beamlet dispersion at various radial locations. The dispersion data at thruster radii of 0.5 and 0.75 indicates that the beamlets were vectored off-axis by as much as 8 to 12°.

F. THRUSTER PERFORMANCE AND SCREEN GRID EROSION MODELS

This section presents mathematical models of thruster performance and screen grid erosion. The thruster performance model, which is based on EMT performance documentation obtained previously at 3000 sec specific impulse in the 1 to 2.5 kW power range, gives an accurate mathematical description of the EMT performance parameters with beam current and beam voltage as independent variables. The model was used to calculate thruster performance parameters in the extended performance range (Figure 1); the results are compared with the experimental data obtained with the extended-performance thruster. An analytical model of screen grid erosion was derived, and erosion rates calculated with the model are compared with the wear rate data obtained using the multilayer erosion monitors.

1. Performance Model

The data from the extensive testing and performance documentation undergone by the 30-cm EMT was used to develop an analytical model of thruster performance. Standard curve fitting techniques were used to develop the mathematical description of EMT performance in terms of beam current, I_B, and beam voltage, V_B:

Total power (in W)

$$P_T = I_B(V_B + 200) + 65 \ , \qquad (7)$$

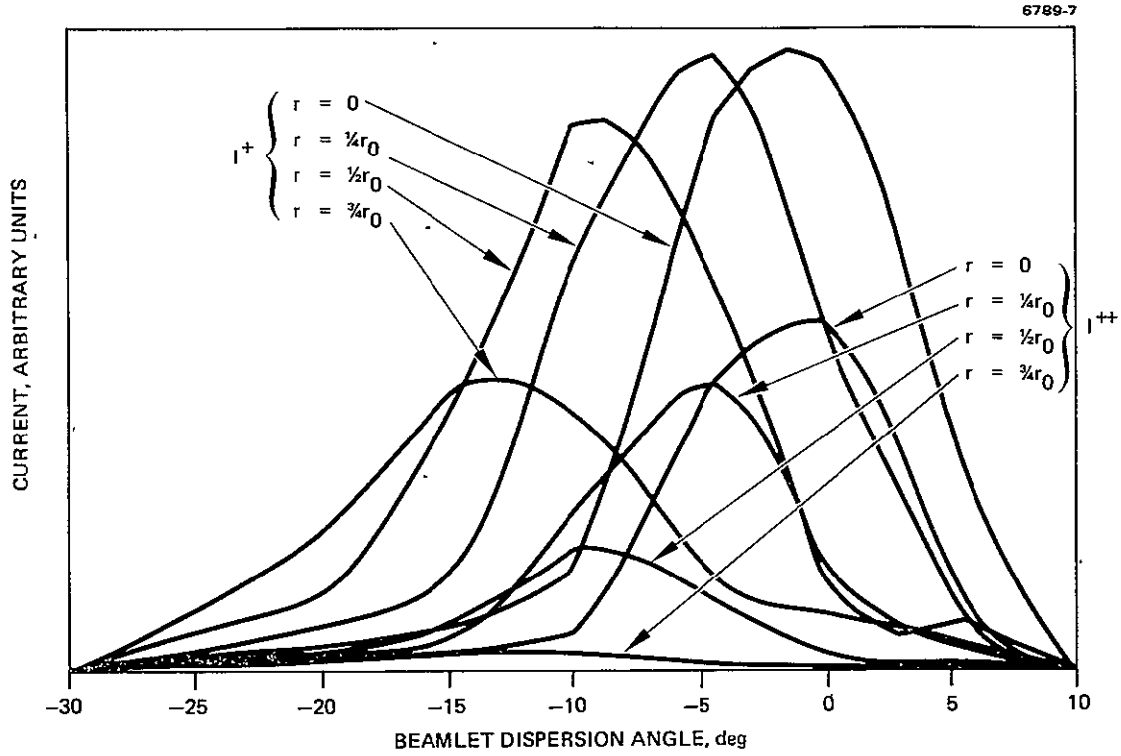

Figure 13. Beamlet dispersion data obtained from $\vec{E} \times \vec{B}$ momentum analyzer measurements (r_0 is the radius of the accelerator aperture array).

electrical efficiency

$$\eta_e = \frac{I_B V_B}{P_T} , \tag{8}$$

propellant utilization efficiency (measured)

$$\eta_u = \frac{1}{\beta} \left[\frac{I_B}{I_B + I_N} \right] \tag{9}$$

$$\beta = 1.0 - 0.8 \left[\frac{I_B + I_{BX}^2}{2.2 + I_{BX}^2} \right] \tag{10}$$

$$I_{BX} = \left\{ \begin{array}{ll} 0 & , \ I_B < 1 \\ I_B - 1 & , \ I_B \geq 1 \end{array} \right\}, \ A \tag{11}$$

neutral loss rate (in A)

$$I_N = 0.240 + 0.032 \ I_B , \tag{12}$$

thrust correction factor

$$\gamma = 0.942 - 0.005 \ I_B + \frac{0.025}{I_B + 0.6} , \tag{13}$$

total thruster efficiency (corrected)

$$\eta_t = \gamma^2 \eta_e \eta_u , \tag{14}$$

specific impulse (corrected, in sec)

$$I_{sp} = 100\, \eta_u\, \gamma \sqrt{V_B}\ , \tag{15}$$

and thrust (corrected, in N)

$$T = 2.039 \times 10^{-3}\, \gamma I_B \sqrt{V_B}\ , \tag{16}$$

where β is the ratio of total propellant flow to the sum of the beam current and neutral loss rate, and I_{BX} is a dummy variable. The expressions presented above were formulated to obtain a "best fit" to the EMT performance data in the 1- to 2-A beam current operating range.

The EMT performance model was used to calculate thruster performance parameters for the extended-performance range. These results, and the experimental results obtained during testing of the extended-performance thruster, are presented in Figures 14 through 18. The mathematical performance model gives an excellent description of the power, thrust, and total efficiency of the extended-performance thruster. There is appreciable scatter in the experimental data for propellant utilization and consequently also for specific impulse. The data points correlate quite well with the analytically determined curves, although the points do not fall near the curves in all instances. Some of the discrepancy may have been caused by changes in beam voltage and magnetic baffle current since these quantities were constant in the EMT data used to formulate the model.

Although beam current and beam voltage were treated as independent variables in the extended-performance operating range, this is true only for the thruster operating envelope defined by (1) the perveance line of the ion optics, (2) the specified voltage standoff capability of the propellant isolators, and (3) the recommended maximum and

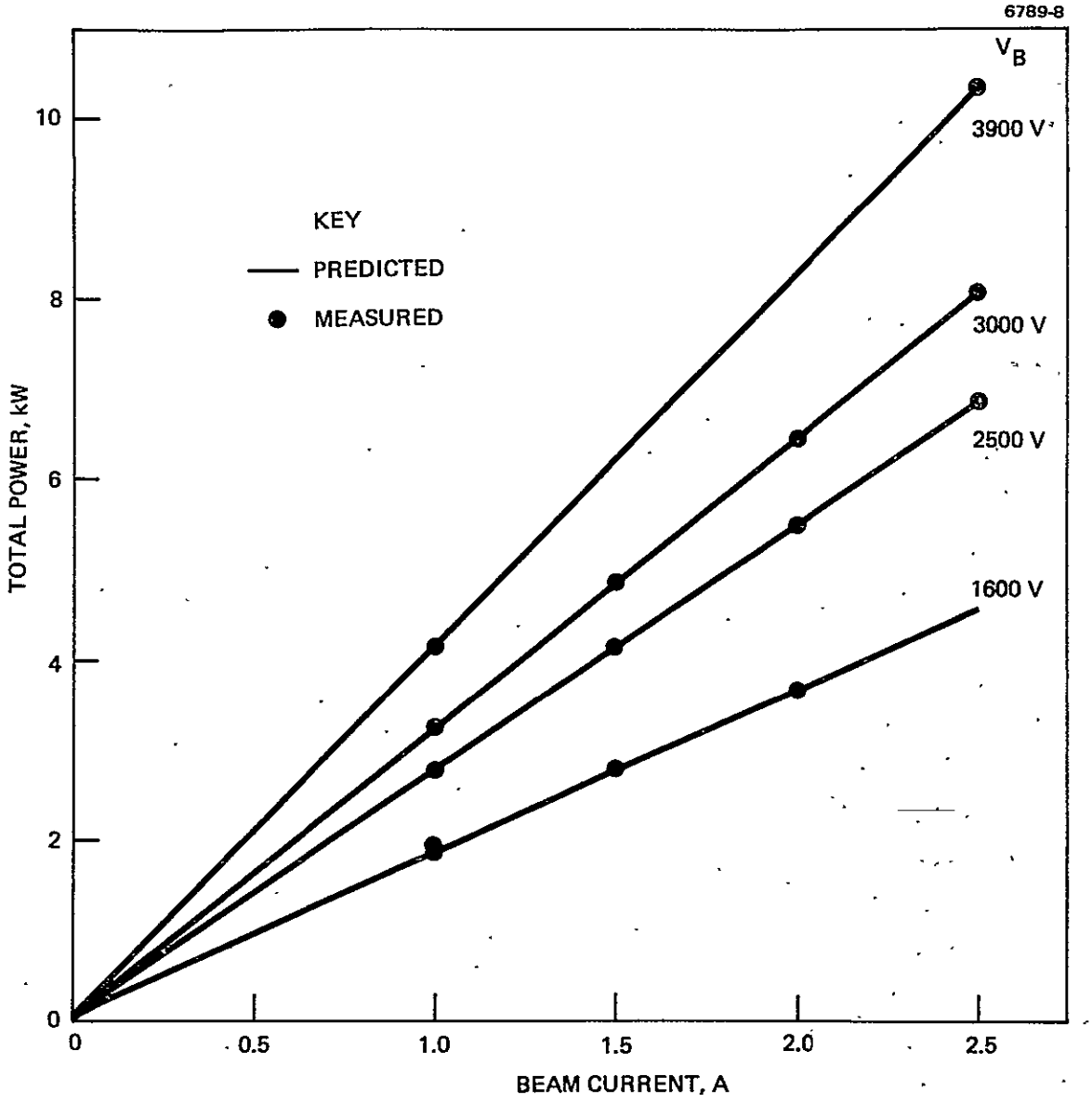

Figure 14. Total power versus beam current: comparison of values predicted by the performance model with measured experimental results.

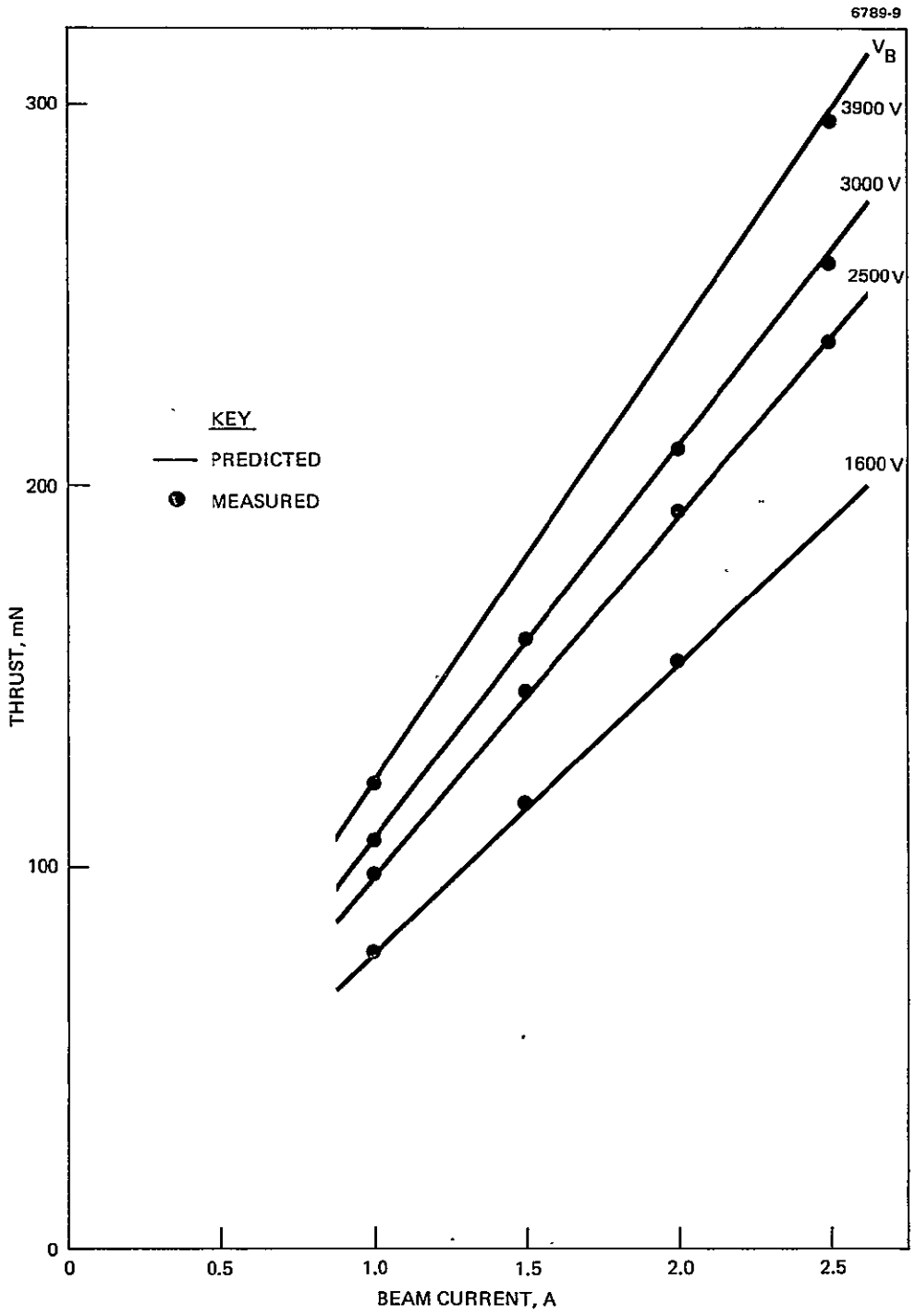

Figure 15. Thrust versus beam current: comparison of values predicted by the performance model with measured experimental results.

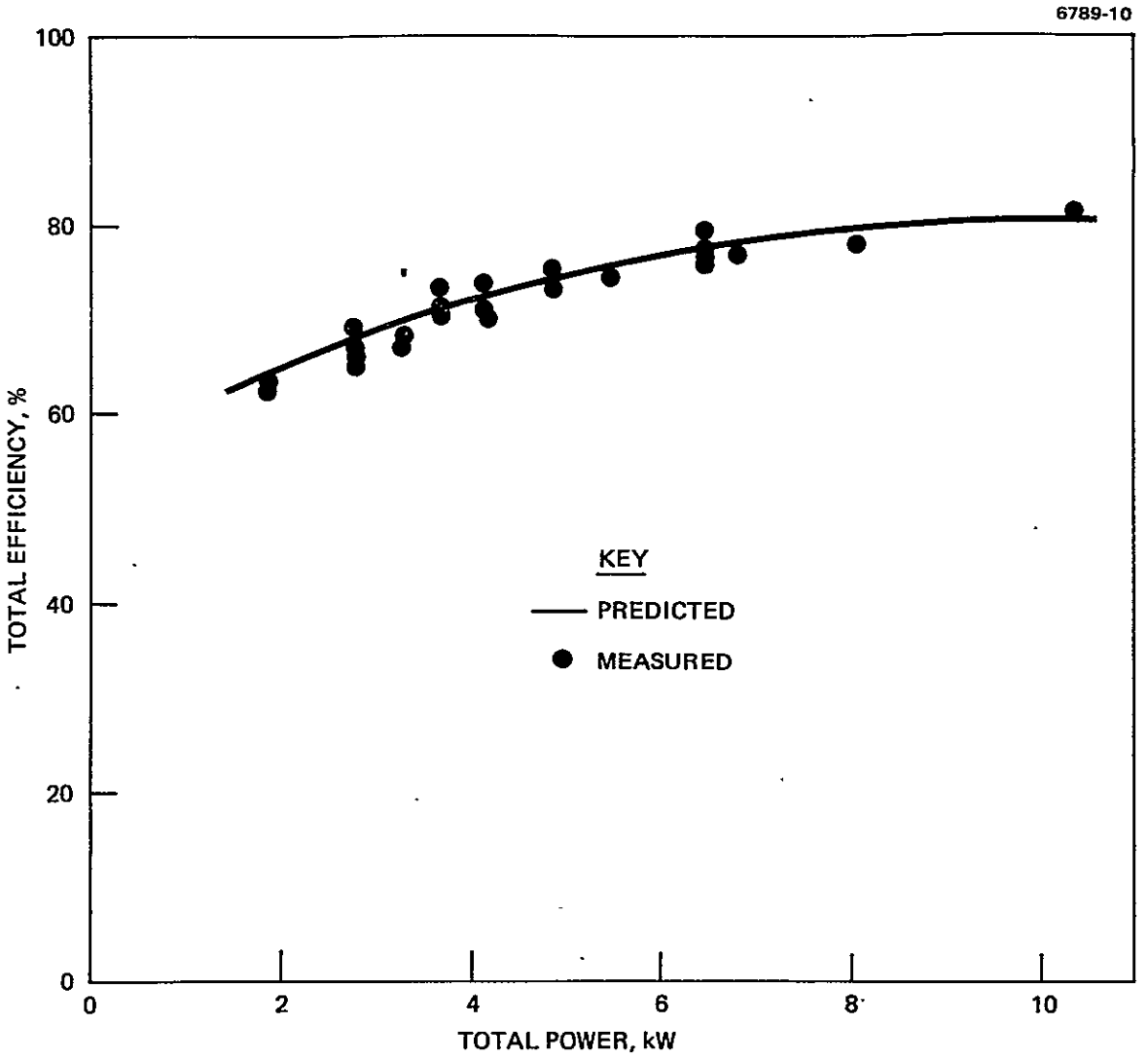

Figure 16. Total efficiency versus total power: comparison of values predicted by the performance model with measured experimental results.

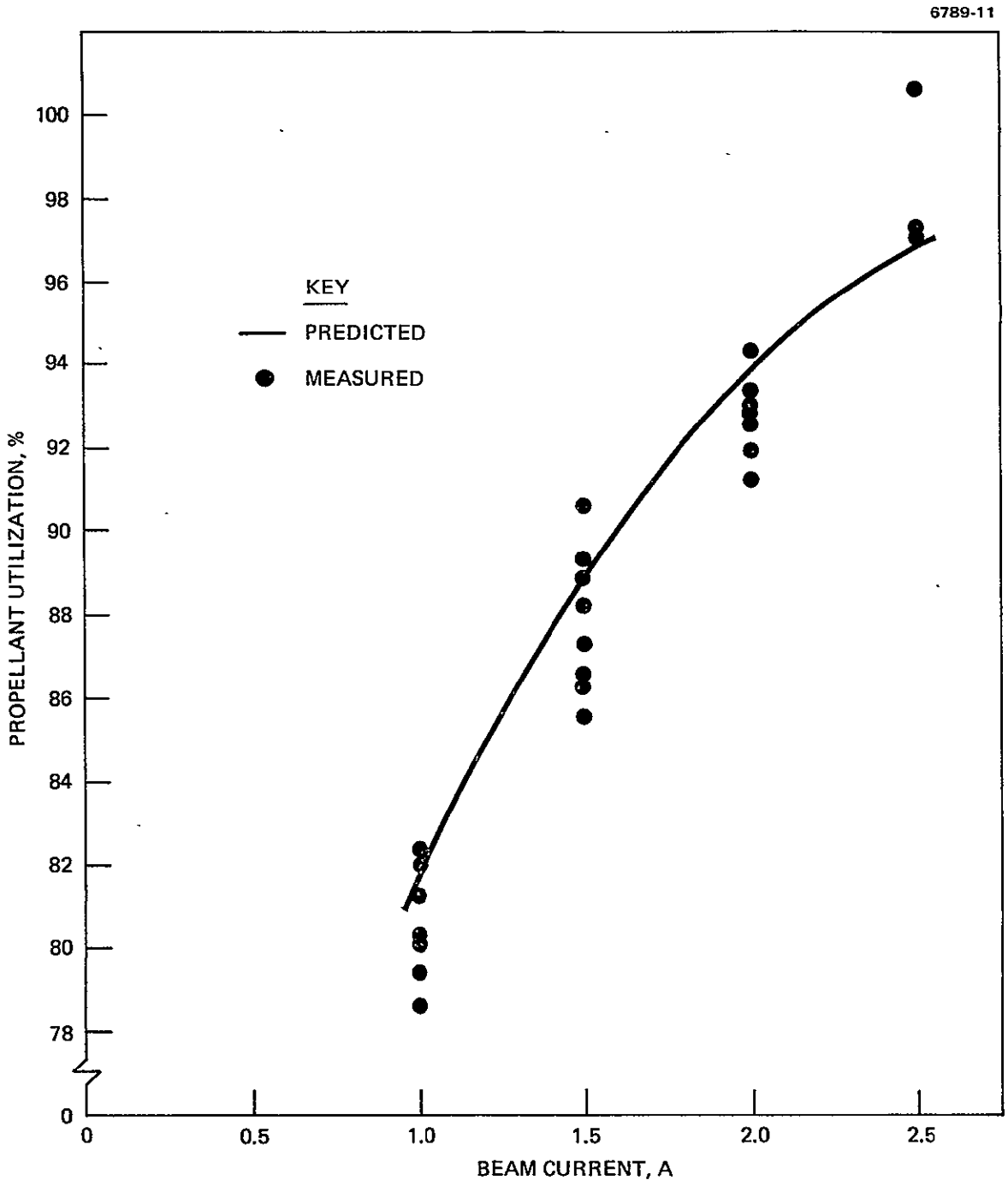

Figure 17. Propellant utilization versus beam current: comparison of values predicted by the performance model with measured experimental results.

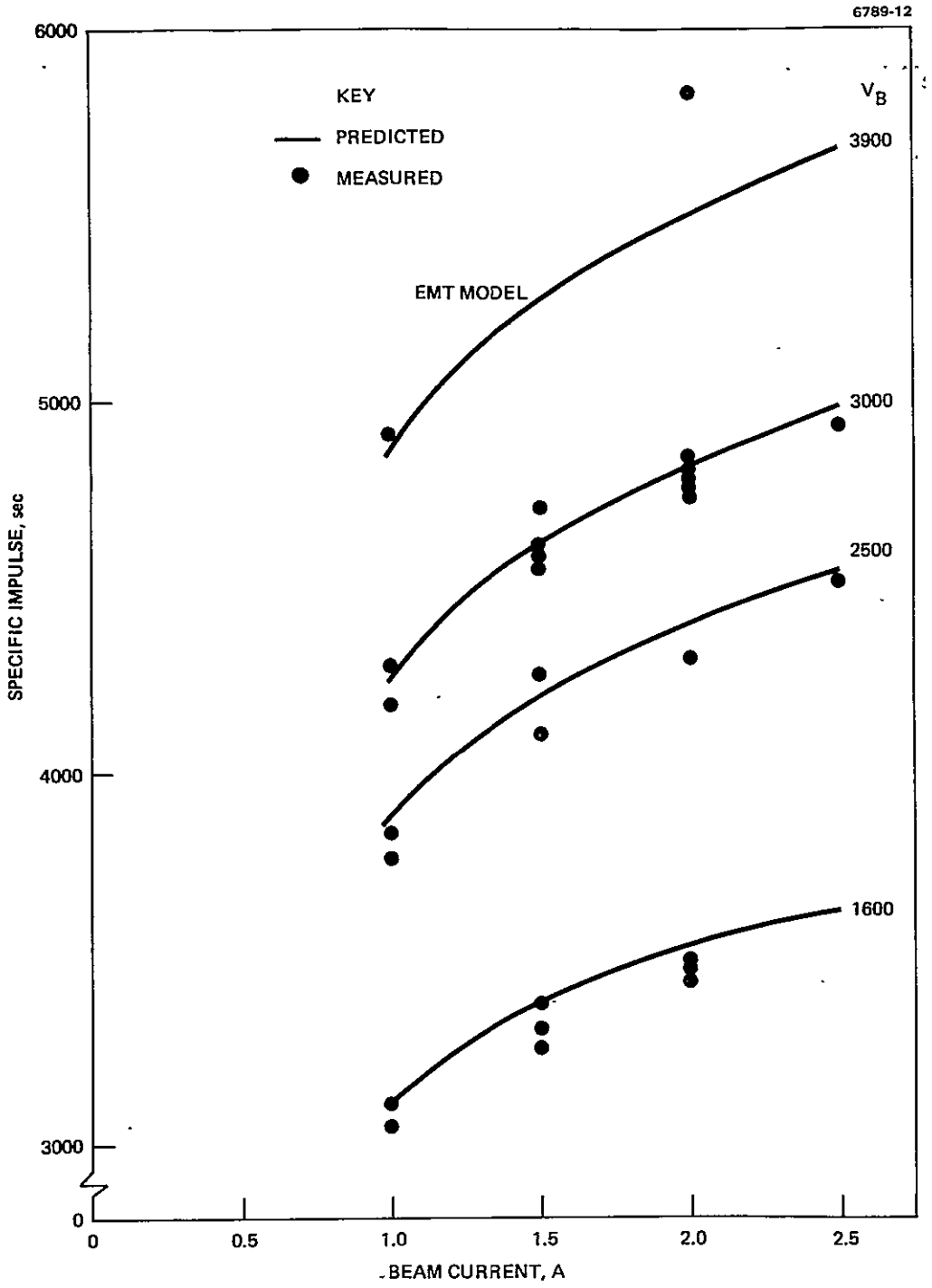

Figure 18. Specific impulse versus beam current: comparison of values predicted by the performance model with measured experimental results.

minimum beam current operating limits of 2.5 and 1.0 A. The perveance limit can be derived from the definition of perveance

$$P \equiv \frac{I_B}{V_T^{3/2}} \quad , \tag{17}$$

where the perveance, p, is found from Figure 5 to be 2.4×10^{-5} $AV^{-3/2}$.

2. Screen Grid Erosion Model

Thruster lifetime is a major concern in all electric propulsion applications because long thrust times are required. This is particularly true of the Halley's comet mission, in which thrusters may be required to operate for as long as 14,000 hr. The lifetime limitation of the current 30-cm EMT design is thought to be caused by failure of the screen grid due to sputter erosion damage. Based on the 10,000-hr endurance test results of thruster SN 701, the erosion rate at the center of the screen grid was estimated at 35 nm/hr when operating at the 2 A beam current level.[3] At this rate, the time required to erode a substantial fraction (say 90%) of the screen grid is $\approx$ 10,000 hr. Although this lifetime would be adequate for many missions, it is only marginal and perhaps inadequate for the primary propulsion requirements of the Halley's comet rendezvous. A mathematical model of screen grid erosion is therefore needed to predict screen grid lifetime and to identify thruster modifications likely to reduce screen grid erosion.

3. Sputtering Model

The surface sputtering rate, W, can be expressed in terms of the incident ion flux, j, and the target sputtering yield, S, by

$$W = (j^{+}S^{+} + \frac{1}{2} j^{++}S^{++})/qn \quad , \tag{18}$$

where n is the density of the target material, q is the electronic charge, and the superscripts refer to the charge on the ion. This expression can be rewritten in terms of the measurable beam parameters by introducing the continuity equation for a nonreacting one-dimensional flow of the charged species

$$J = j\phi_s \ , \tag{19}$$

where J is the current density immediately downstream from the accelerator grid, and $\phi_s = A_s/A_B$ is the ratio of screen grid open area to active beam area. Combining Eqs. 18 and 19 yields an expression for the wear rate in terms of beam conditions:

$$W = \frac{J_T}{qn\phi_s}\left[\frac{S^+ + \frac{1}{2}(J^{++}/J^+)S^{++}}{1 + J^{++}/J^+}\right] \ , \tag{20}$$

where J_T is the sum of the single- and double-ion current densities. This expression can be applied if local values of the current density and sputtering yield (ion energy) are used.

The screen grid lifetime can be predicted by applying the wear rate expression to the thruster centerline, where the total current density and double-to-single ion current density ratio are highest and maximum screen grid erosion is observed. The current density, J_{TO}, at the centerline is given by

$$J_{TO} = \frac{1}{F}\left[\frac{I_B}{A_B}\right] \ , \tag{21}$$

where F is the beam flatness parameter, defined as the ratio of the average beam current density to the maximum beam current density

evaluated at the accelerator grid. Combining Eqs. 20 and 21 yields the screen grid erosion rate on centerline, W_o

$$W_o = \frac{I_B}{qnF\phi_s A_B}\left[\frac{S^+ + 0.5\,\mathscr{J}_o\,S^{++}}{1+\mathscr{J}_o}\right] , \qquad (22)$$

where $\mathscr{J}_o$ is the ratio of double-ion current density to single-ion current density on centerline. Expressing the erosion rate in this form permits easy identification of those factors affecting screen grid lifetime. For example, operation at a high beam current increases the erosion rate and shortens thruster lifetime. This effect is nonlinear because $\mathscr{J}_o$ also increases with beam current. The inverse dependence of erosion rate on the product $F\phi_s$ indicates the advantages of a uniform current density profile and of a screen grid design having a high open area fraction. The advantages of thruster operation at reduced discharge voltage levels are implicit in Eq. 22 since the sputtering yields and $\mathscr{J}_o$ are strong functions of the discharge voltage. This effect is also highly nonlinear since $\mathscr{J}$, S^+, and S^{++} are nonlinear functions of discharge voltage.

4. Thruster Lifetime Prediction

The screen grid erosion expression can be written in a form convenient for calculating thruster lifetimes by introducing the screen grid parameters and estimated beam flatness of the 30-cm EMT:

$$\phi_s = 0.75$$

$$A_B = 573\ cm^2$$

$$n = 6.4 \times 10^{22}\ cm^{-3}$$

$$F = 0.58\ .$$

Substituting these values into Eq. 22 yields

$$W_o = 1.409 \times 10^4 \left[\frac{S^+ + 0.5\mathcal{J}_o S^{++}}{1 + \mathcal{J}_o}\right] I_B \text{ in nm/hr} \quad . \quad . \quad (23)$$

The sputtering yields S^+ and S^{++} are evaluated at the single-ion energy E and the double-ion energy 2E using the experimental data of Askeroy and Sena.[6] The single-ion energy E is assumed equal to the local plasma potential, which is approximated as the sum of the discharge voltage plus the anode sheath potential (assumed to be 6 V). Thus S^+ can be approximated as

$$E = V_D + 6 \quad . \quad . \quad (24)$$

Eq. 23 can be used to predict the thruster lifetime under various operating conditions, where the thruster lifetime, $\mathscr{L}$, is defined as the time required to erode a substantial fraction (90%) of the screen grid. Table 6 presents calculated thruster lifetimes based on operating parameters taken from Table 2 and Ref. 3 and on the assumption of 90% of the grid having been eroded. These results indicate the strong dependence of thruster lifetime on beam current operating point. Reducing the beam current by a factor of 0.5 results in an increase in predicted lifetime by a factor of almost 4. A factor of 2 is gained by the reducing beam current density; the remainder of the improvement occurs because the ratio of double-ions to single-ions is reduced. Table 6 also presents erosion rate and thruster lifetime calculations for discharge conditions that were measured using SHAG optics on the EMT thruster. At the 2-A beam current level, reducing the discharge voltage to 30 V by using SHAG optics increases the predicted thruster lifetime to 23,000 hr. This is a factor of 2.5 increase over the predicted lifetime when standard EMT grids are used.

The validity of the thruster lifetime predictions can be assessed by comparing the calculated screen grid erosion rates with measurements obtained during the endurance test of thruster SN 701. The measured

Table 6. Calculated Screen Grid Erosion Rates and Thruster Lifetimes

Optics	I_B, A	V_D, V	$\mathscr{J}_o$	S^{++} x 10^3	S^{+} x 10^3	W_o, nm/hr	$\mathscr{L}$, hr
EMT	2.0	36	0.5	6.5	0.4	38	9,000
EMT	1.5	36	0.3	6.5	0.4	22	15,300
EMT	1.0	36	0.15	6.5	0.4	11	31,500
SHAG	2.0	30	0.22	3.5	0.25	15	23,000

T5917

erosion at the center of the screen grid after 10,000 hr of operation at 1.4 A beam current was 0.18 mm, equivalent to an erosion rate of 18 nm/hr. This value can be extrapolated (approximately) to 1.5 A beam current operation by multiplying by the ratio of beam currents. This results in an extrapolated screen grid erosion rate of 19.3 nm/hr. The screen grid erosion rate calculated for the extended-performance thruster operated at 1.5 A beam current is 22 nm/hr, which is about 14% higher than the extrapolated value; this is considered to be reasonably good agreement. The screen grid erosion rate of thruster SN 901 was 31 nm/hr after $\approx$ 4,000 hr of operation at 2 A beam current.[7] The calculated value for the extended-performance thruster is 38 nm/hr. This agreement is considered reasonable, particularly considering the simplicity of the model and the uncertainties present.

5. Comparison of Calculated and Measured Screen Grid Erosion Rates

Calculated (using the erosion model) and measured (using the multilayer erosion monitor technique) screen grid erosion rates are presented in Table 7 for comparison. The agreement at the 1.5 A beam current level is within the uncertainty in the measured results and is therefore considered very good. Both the measured and calculated values are in agreement with the screen grid erosion rate of 19.3 nm/hr extrapolated (also for 1.5 A beam current) from the 10,000 hr endurance test of thruster SN 701. Although there is apparent agreement at the 1.5 A beam current level, at higher or lower beam current levels the

Table 7. Comparison of Calculated and Measured Screen Grid Erosion Rates

I_B, A	Screen Grid Erosion Rate, nm/hr	
	Calculated	Measured
1.0	11	2.6 ±1.3
1.5	22	20.7 ±3.2
2.0	38	52.3 ±5.0

T5917

agreement is poor. There are, however, several plausible explanations for the differences in calculated and measured erosion rates; these are discussed below.

The calculated results were based on sputtering yields taken from published data that had been taken in laboratory experiments conducted under carefully controlled vacuum conditions. Therefore, this sputtering yield data may not be equivalent to what would have been obtained in the actual discharge chamber environment because of various effects such as surface temperature variations, adsorption of vacuum chamber residual gases, chemical reaction on discharge chamber surfaces, and formation of surface irregularities or "cones." Depending on the thruster power level and vacuum chamber conditions, these effects may either increase or decrease the effective surface sputtering yield. Another factor that strongly affects the calculated erosion rate is the beam flatness parameter. A value of F equal to 0.58 (taken from EMT beam measurements) was used in all calculations. However, the beam profile may become more uniform at reduced beam current levels, which would reduce the calculated screen grid erosion rate. The calculated erosion rate is strongly dependent on the shape of the beam profile: if the assumed value of beam flatness were reduced from 0.58 to 0.47, the calculated erosion rate corresponding to the 2-A beam current conditions would be 47 nm/hr. This is within 10% of the measured value, which is less than the uncertainty in the erosion rate measurement.

The erosion rate measured at the 2-A beam current level is significantly higher than the 29 to 31 nm/hr measured during previous tests[3,7] and, if valid, would severely limit the lifetime of the screen grid. One factor that may have increased the screen grid erosion rate (and, for that matter, the erosion rate for all discharge chamber components) is the low tank pressure maintained during the extended-performance thruster tests. The dependence of measured discharge chamber erosion rates on ambient conditions in the vacuum chamber was recognized early in the test program. This was based on an experimental and analytical evaluation performed at NASA LeRC of the results from the 900 series thruster endurance testing at Hughes.[7] Precautions were taken to ensure a high-quality vacuum environment during the erosion monitor tests. Other investigations of discharge chamber sputtering have indicated that baffle erosion is strongly dependent on cathode flow rate.[8] In these studies, the baffle erosion rate was observed to increase by a factor of 2 when the cathode flow rate was increased from 80 to 135 mA. The cathode flow rate during the tests of the extended-performance thruster was about 110 mA at the 2-A beam level, which may explain the higher observed baffle erosion. Since the increase in baffle erosion with cathode flow is apparently caused by increased ionization near the baffle aperture, its effect should be localized. Therefore, it is difficult to associate an increase in screen grid erosion with cathode flow effects unless these flow effects give rise to some other phenomenon (such as increased discharge chamber oscillations) that strongly affects erosion rates.

F. CONCLUSIONS

Performance characteristics of the thruster used in this program are essentially identical to those previously documented and analytically modeled using the 30-cm EMT. Therefore, the mathematical model describing the performance parameters of the EMT in terms of the independent variables of beam current and beam voltage is applicable to the extended-performance thruster operating envelopes proposed for the Halley's comet rendezvous mission.

Re-spacing the EMT ion optics assembly to an interelectrode gap of 0.76 mm provides more than adequate perveance throughout the extended performance operating envelopes and provides sufficient voltage standoff capability. The only other thruster modifications required for high-voltage operation are replacement of the cathode and main propellant isolators and the use of insulated restraints for preventing contact between wiring and thruster structural members.

An accelerator grid voltage of 500 V is adequate to prevent electron backstreaming for beam voltages as high as 3900 V. The backstreaming limit of the re-spaced EMT ion optics is $\approx$ 400 V.

The ion beam envelope does not change significantly with beam conditions. When operating at a constant accelerator grid voltage of 500 V, 95% of the primary beam ions are contained within a 20^{o} cone and all primary beam ions are within a 51^{o} cone. The ion beam cone angle can probably be reduced by as much as 10^{o} by reducing the off-axis current component of those beamlets emanating from the outer grid apertures.

High-power thruster operation results in component temperatures that are within the acceptable operating ranges.

At 1.5 A beam current level, both the multilayer erosion monitor measurements and the screen grid erosion calculations agree with the screen grid erosion rate observed in the 10,000-hr endurance test of thruster SN 701. However, at higher or lower beam current levels, the agreement between calculated and measured results is poor.

The measured discharge chamber erosion rates are substantially higher than those measured in the EMT thruster; if these rates are valid, erosion would severely restrict thruster lifetime. The observed increase in measured erosion rates is thought to be due, at least in part, to carefully controlled vacuum conditions.

An analytical model of screen grid erosion was developed that relates screen grid erosion to the discharge chamber plasma properties and certain discharge chamber parameters. The erosion model suggests that the most effective means of improving screen grid lifetime are (1) to reduce discharge voltage by using small-hole accelerator grids

and (2) to improve the plasma density profile (increase the flatness parameter) near the screen grid by some means such as a magnetic field modification.

SECTION 3

DEVELOPMENT OF THE HIGH-VOLTAGE PROPELLANT ELECTRICAL ISOLATOR

The 900-series EMT was developed for operation at a specific impulse of 3,000 sec (beam voltage of 1,100 V). The propellant electrical isolators were developed to have a conservative, steady-state voltage rating of 1,500 V. As pointed out in Section 2, the extended-performance operation range includes beam voltages as high as 3,900 V. Consequently, a high-voltage propellant isolator design is required that can provide a conservative, steady-state voltage rating of at least 5,000 V. Because the allotted schedule time was short, the approach taken here was to scale existing isolator designs, build prototype components, and perform comparative tests. Two isolator design concepts were investigated: a multisection concept that is used in the 900-series EMT design[9] and an insulating labyrinth concept that has been successfully demonstrated in the British ion propulsion program.[10] The evaluation of these concepts is described in this section.

A. THE MULTISECTION HIGH-VOLTAGE ISOLATOR CONCEPT

The fundamental problem in designing a propellant electrical isolator is the prevention of the ionization of the gaseous propellant being supplied to the thruster. Since the propellant vaporizers and propellant storage tanks should be operated at spacecraft potential, the full beam voltage appears across the insulator used to transmit the propellant to the thruster. Ionization of the gas in this situation is governed by the type of gas, the gas pressure (or density), and the dimensions which characterize the vessel containing the gas. Empirical relations have been determined under controlled geometric configurations for several gases, including mercury vapor. These relationships, known as Paschen breakdown curves, relate breakdown voltage to the product of the gas pressure and the gap distance across

which the voltage is applied (p-d). A typical Paschen curve is shown in Figure 19. The basic physical principle involved is that there exists a limiting voltage for any given product of gas pressure and characteristic dimension. Below that voltage, not enough electrons are accelerated across the dimension by the applied voltage to cause a cumulative ionization (avalanche); above that voltage, ionization occurs. This relationship between breakdown voltage and p-d is strongly dependent on boundary conditions (material, surface condition, etc.). Measurements like those shown in Figure 19 are usually made using highly polished, plane, parallel electrodes to define the characteristic dimensions across which the voltage is applied (electric field is established). The voltage minimum on this curve in Figure 19 is sometimes referred to as the Paschen minimum. Voltages below this value cannot cause ionization of the gas in question at any value of p-d. The EMT propellant electrical isolator design is based on the concept of a Paschen minimum breakdown voltage.

In the 900-series EMT isolator design, the vapor flow channel is divided into seven chambers (or sections) by optically dense metal screens, as shown in Figure 20. The voltage is assumed to divide evenly across the length of the alumina cylinder that contains the vapor. Therefore, with 1500 V applied, the voltage across any section would be $\approx$ 215 V, which is less than the Paschen minimum for mercury covered electrodes ($\approx$250 V). At high flow rates, the breakdown voltage for this design is about 2000 V (see Figure 21). Because of the long lead time for obtaining high-quality ceramic materials, we elected to scale the design conservatively (by a factor of four) to leave as many options as possible open. An isolator having 28 sections was therefore specified. One option is to maintain the electric field strength along the insulator surface constant and to increase the overall isolator length also by a factor of four. This would result in an assembly that is structurally questionable with regard to its ability for surviving vibration during launch. We elected to evaluate an assembly of this type (see Figure 22) to prove the scaling principle. The other design extreme is to keep the overall isolator length the same

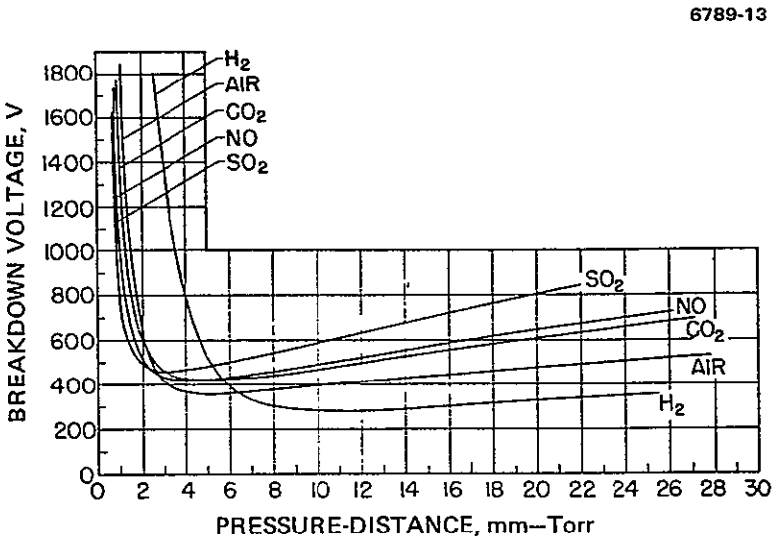

Figure 19.
Paschen curves for various gases. (Taken from Ref. 28.)

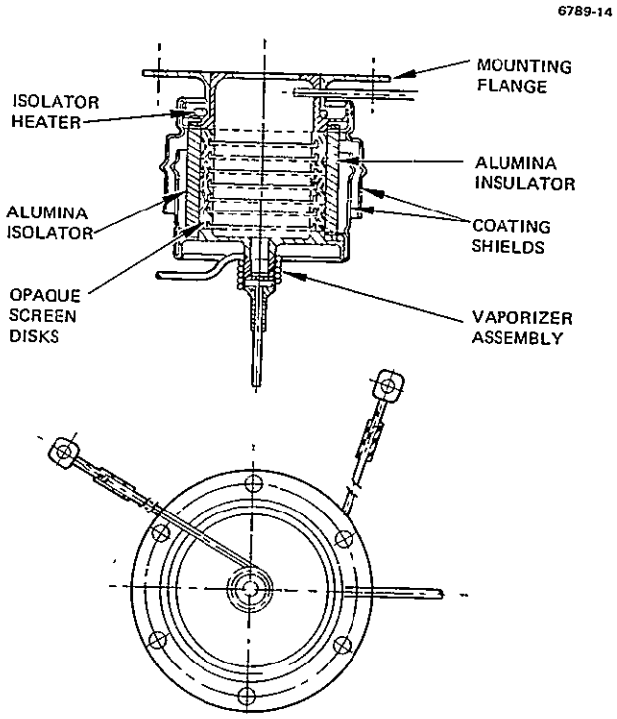

Figure 20. Isolator-vaporizer configuration of the 30-cm thruster.

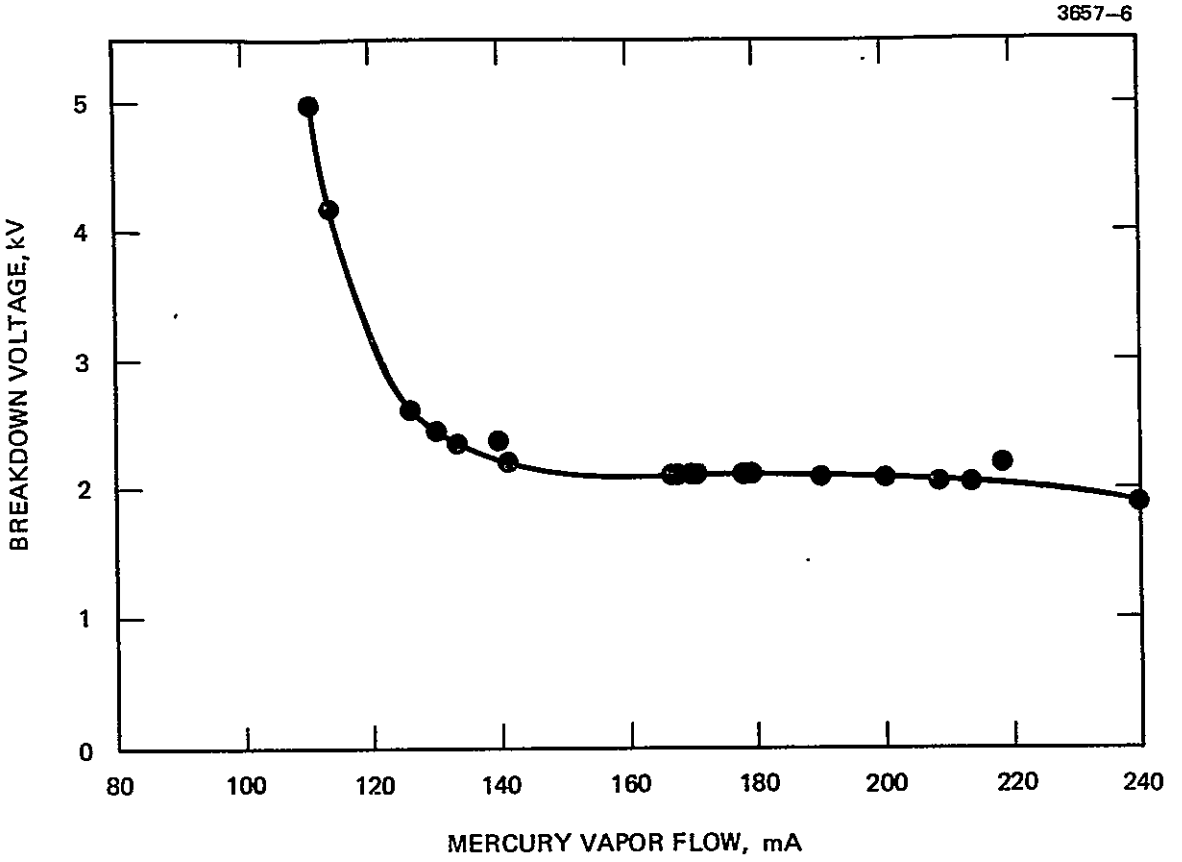

Figure 21. Isolator breakdown voltage as a function of mercury flowrate.

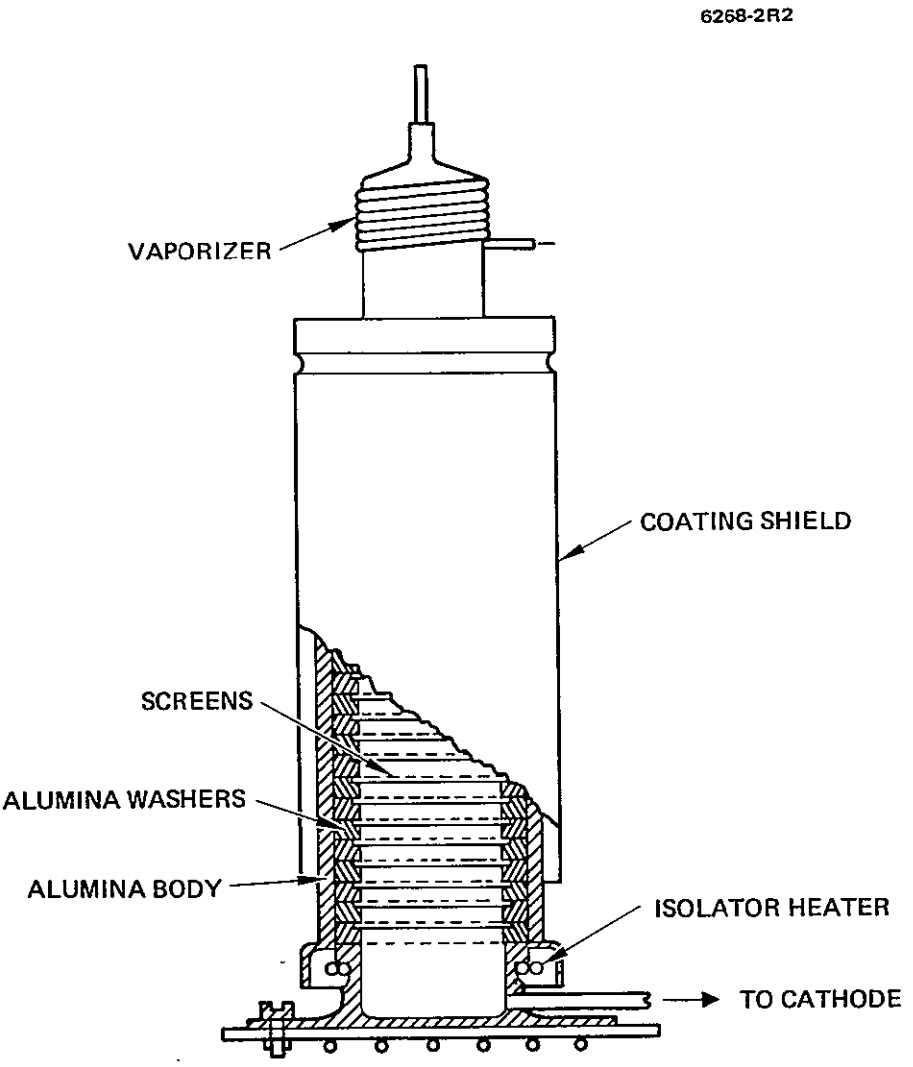

Figure 22. 900-series isolator scaled directly to 28 sections (4 X).

while scaling only the internal elements. This approach is shown in Figure 23; the resulting component becomes a direct replacement for the isolator used on the 900-series EMT. The structural characteristics of this assembly should be the same as those of the 900-series design, but with the field strength along the insulator surface increased by about a factor of four. Based on our experience with high-voltage insulators, surface breakdown on insulators is not significant until the field strength (in vacuum) exceeds 5 kV/cm. Similarly, the interfaces between the dielectric and conductor require no special treatment (to avoid field concentrations) until field strengths exceed 5 kV/cm. Since the field strength in the design shown in Figure 23 is only about half this value, the design was considered to be adequately conservative. The spacers selected for this design are thin alumina discs (such as shown in Figure 24). These discs, which are cast alumina, were chosen more for their short delivery schedule than for their material composition, although their insulating properties are essentially the same as those of the Al 300 alumina material used for the 900-series isolator spacers.

An isolator was constructed in a cathode-isolator-vaporizer configuration for each of these designs; the same quality-control procedures were used as are used in fabricating isolators for the 30-cm EMT. Both isolators were successfully tested with applied voltages up to 6 kV without breakdown under full vapor flow conditions. Test procedures and detailed results are described in Section 3.C.

B. INSULATING LABYRINTH ISOLATOR CONCEPT

With this concept, the propellant vapor is forced to flow through an insulating labyrinth. This can be done by using (1) a porous ceramic that has relatively small pores, (2) tightly packed insulating spheres, or (3) tightly packed insulating fibers. The physical principle is to prevent ionization by providing a high surface-to-volume ratio so that any electron-ion pair formed will reach a surface before it collides with another gas atom. This approach was used successfully

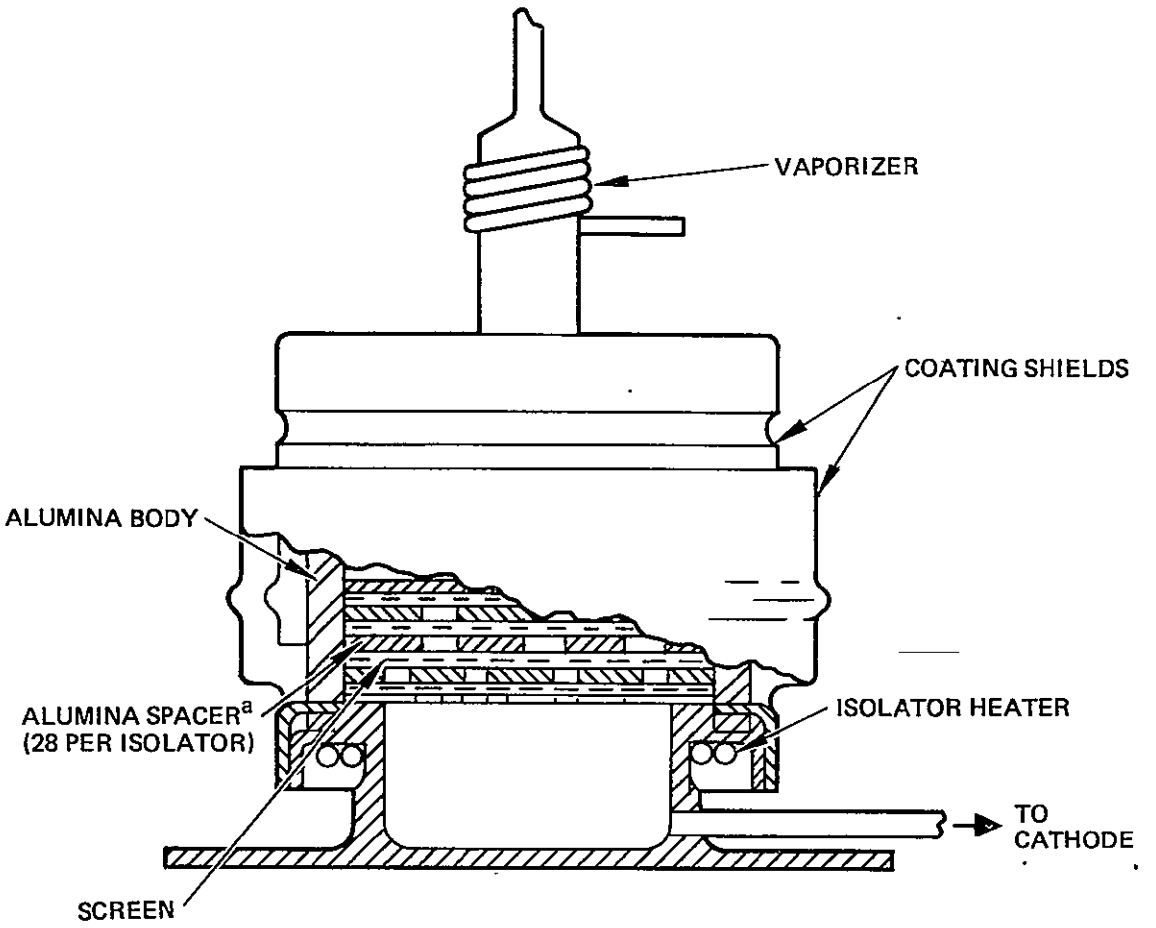

[a]ALUMINA SPACERS 0.65 mm (0.025 in.) THICK (SEE FIGURE 20).

Figure 23. High-voltage propellant electrical isolator using multi-section design concept. (Internal scaling.)

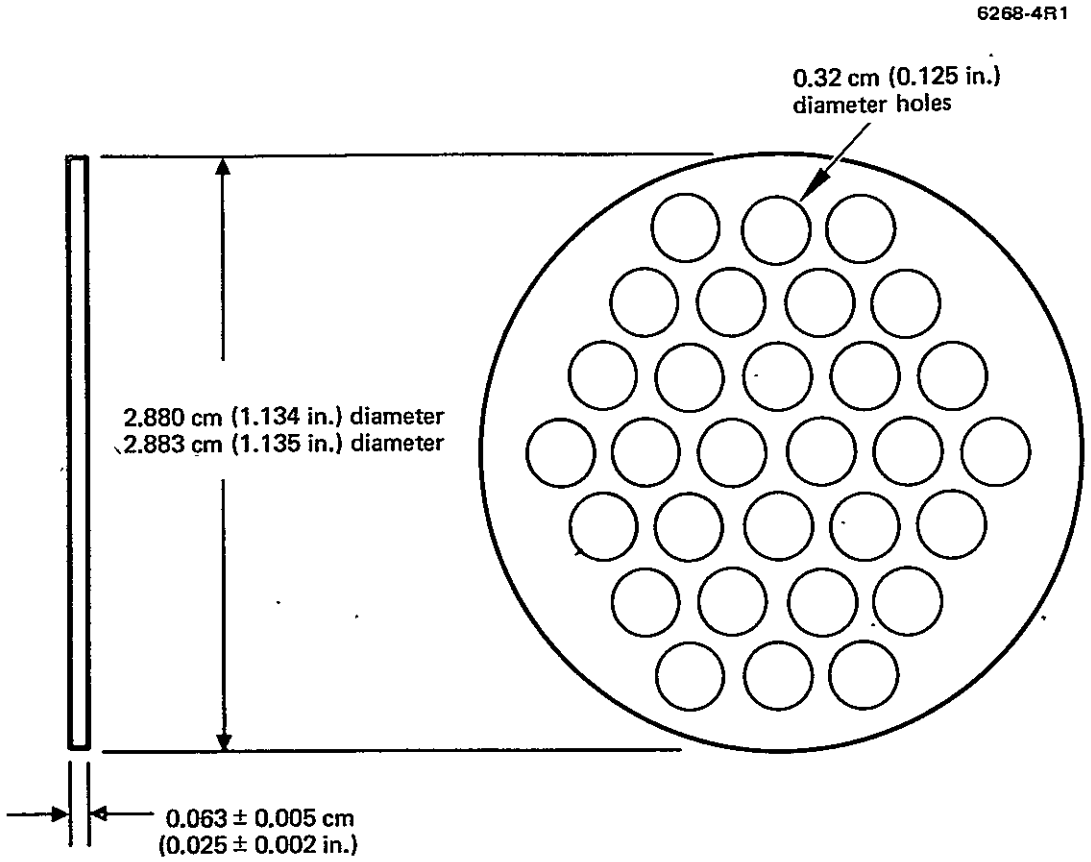

Figure 24. Alumina spacer for the 28-section isolator.

in the British thruster development program.[10] Although the design criteria for this isolator concept are not well defined, our approach was to use an isolator envelope that had the same dimensions as the EMT isolator and to replace the spacers and screens by tightly packed ceramic spheres, as shown in Figure 25. We assumed that we could use Pye's results, which show breakdown voltage to be inversely proportional to sphere diameter.[10] Given that relationship, spheres of 0.1 to 1 mm diameter should have been used. But the only insulating spheres that were obtainable during this program were a mixture ranging from 0.2 to 2 mm in diameter. We elected to assemble an isolator with the configuration shown in Figure 25 in a manner such that the downstream boundary of the isolator could be removed for replacement of the insulating spheres. With such an isolator, we proposed to select sphere sizes from the assortment and evaluate the dependence of breakdown voltage on sphere diameter.

A demountable main isolator assembly (as shown in Figure 25) was successfully fabricated. But the sample of ceramic spheres obtained was found to contain sphere sizes that were predominantly in the 1.2 to 1.5 mm diameter range. Consequently, the evaluation performed is neither complete nor conclusive. The test procedures and results are discussed in more detail in Section 3.C.

C. ISOLATOR TESTS

After fabrication, the isolators were inspected visually, given a preliminary electrical checkout for heater continuity, and installed in a vacuum bell jar. The vacuum facility is pumped by a 15-cm-diameter mercury diffusion pump and has both freon refrigerated and liquid nitrogen baffles. Typical ambient pressure is about 2×10^{-6} Torr. A schematic of the test apparatus is shown in Figure 26. Isolator testing proceeded as follows:

- Isolator leakage current was measured with a voltage of 6 kV applied; the isolator and vaporizer were at ambient temperature.

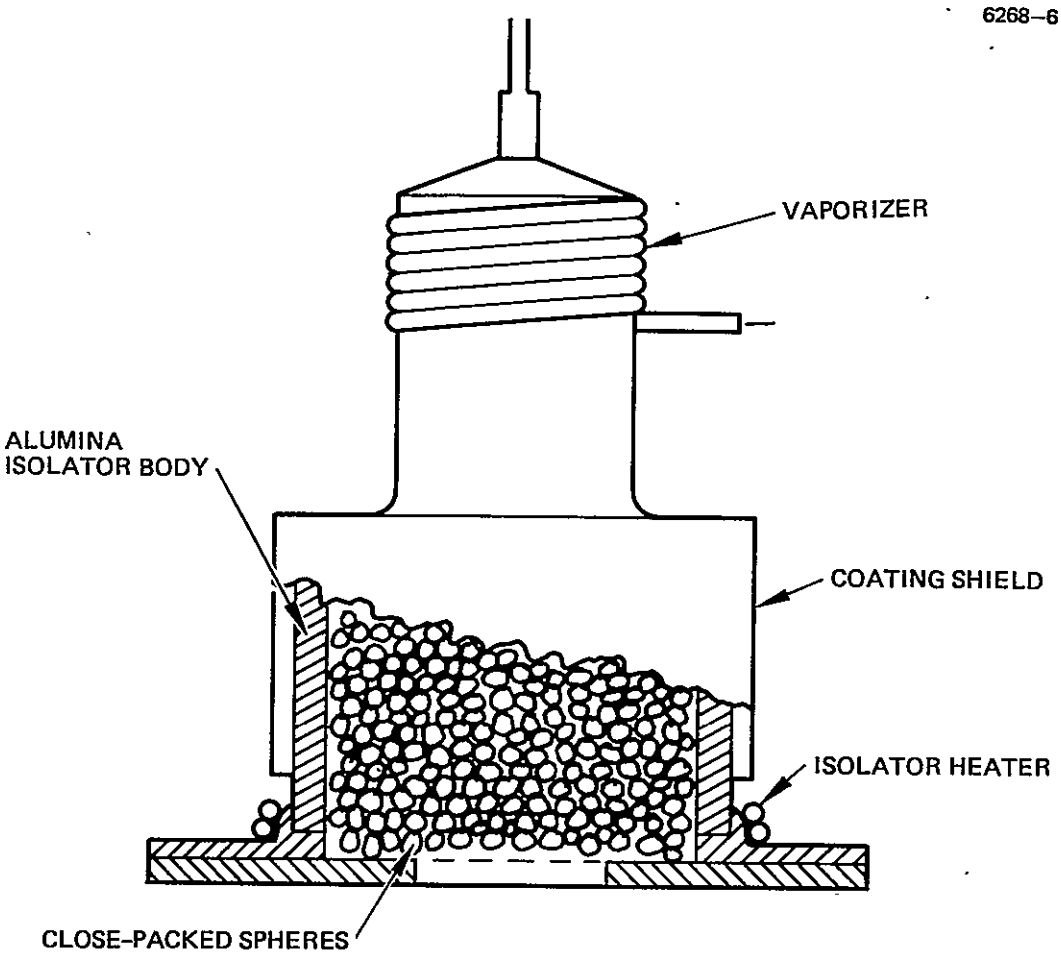

Figure 25. High-voltage propellant electrical isolator using insulating labyrinth design concept.

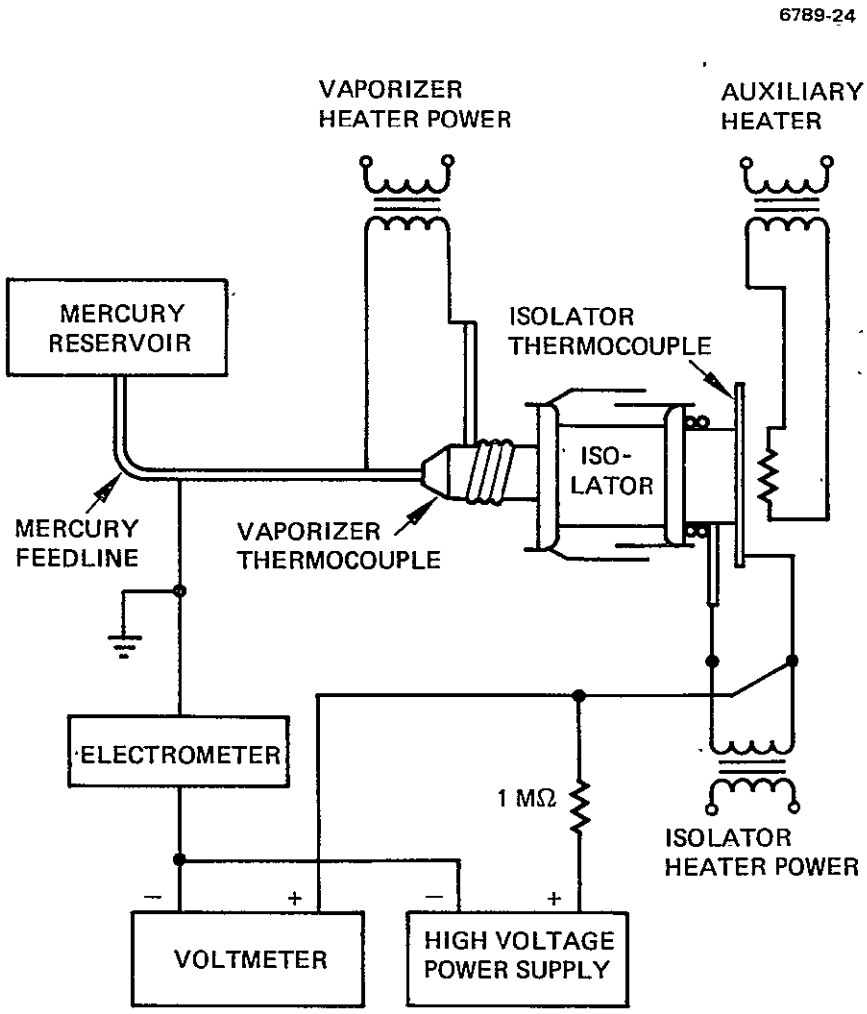

Figure 26. Schematic of high-voltage propellant isolator test apparatus.

- Isolator leakage current was measured with 6 kV applied; the isolator base was heated to 300°C.
- With the isolator base at 300°C, the vaporizer flow rate was adjusted to ≈150 mA (equivalent); voltage was applied to the isolator in 1-kV increments and leakage current was measured as a function of applied voltage up to a limit of 6 kV or to isolator breakdown, whichever occurred first.

The results of this testing are summarized in Table 8. Both of the multisection isolators meet the operational temperature, voltage, and propellant flow requirements (300°C, 6 kV, and 100-to 150-mA propellant flow rate); the insulating-labyrinth-type isolator sustained internal breakdown as a function of isolator temperature. Since the short internally scaled multisection isolator appeared to operate as well as did the longer version, it was selected for a longer duration test of 300 hr.

The conditions for the 300-hr test were specified by NASA:

- Isolator base temperature = 300°C
- Vaporizer temperature = 375°C
- Applied voltage = 4 kV.

The isolator leakage current was monitored continuously by strip chart recorder and flow rate data was recorded twice each working day. The average flow rate measured for the test was about 260 mA (approximately three times the EMT flow rate). The leakage current rose approximately linearly with time over the duration of the test, as shown in Figure 27. Leakage current behavior similar to this has also been observed in testing performed during the development of the 900-series EMT isolator design.[12] The leakage is related to surface contamination of the ceramic insulator. This contamination causes a semiconducting thin film to form on the insulator; this film conducts in proportion to the absolute temperature of the isolator. (A detailed description of both the sources of contamination and preventive measures is given in Ref. 12.) In brief, the insulator surface must be protected from any possible contamination during fabrication by careful assembly procedures

Table 8. Summary of Isolator Test Results

Conditions for Isolator Leakage Tests	Long Multisection Isolator[a]	Short Multisection Isolator[a]	Isolator Filled with Ceramic Spheres[b]	
Ambient temperature; 6 kV applied				
Isolator leakage, nA	2	3	3	
Isolator hot; 6 kV applied				
Isolator base temperature, °C	290	300	290	
Vaporizer temperature, °C	80	190	260	
Isolator leakage, μA	0.13	0.02	0.06	
Isolator hot, vaporizer flow rate "normal"				
Isolator base temperature, °C	330	330	302	152
Vaporizer temperature, °C	345	340	255	258
Vaporizer flow rate, A	0.150	0.130	1.81	2.0
Isolator leakage at 1 kV, μA	0.09	0.02	0.005	0.1
Isolator leakage at 2 kV, μA	0.1	0.03	0.01	0.2
Isolator leakage at 3 kV, μA	0.1	0.03	[c]	0.3
Isolator leakage at 4 kV, μA	0.11	0.03		0.4
Isolator leakage at 5 kV, μA	0.12	0.04		0.54
Isolator leakage at 6 kV, μA	0.13	0.04-1[d]		[e]

[a] These isolators were cathode-isolator-vaporizer configurations operated with a cathode attached for flow impedance.

[b] This isolator was a main-isolator-vaporizer configuration.

[c] Breaks down at 2800 V.

[d] Meter reading fluctuated between 0.04-1 μA — no evidence of breakdown.

[e] Breaks down at 5200 V.

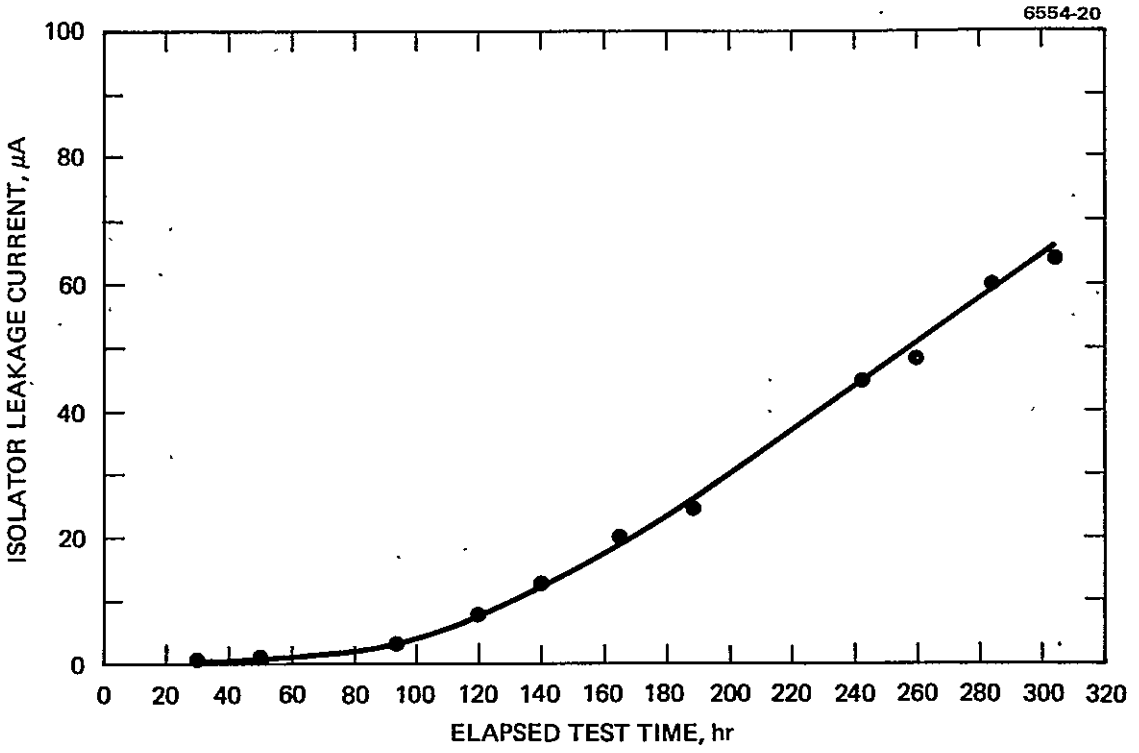

Figure 27. Isolator leakage current versus elapsed test time for the multisection isolator design shown in Figure 23.

and during operation by eliminating possible contaminants from the isolator vicinity and by including protective shielding. Procedures prescribed by NASA LeRC have eliminated this leakage for EMT operating temperatures and voltages. Although the prescribed handling and operating precautions were observed in preparing this test, portions of the auxiliary heater (which was used to simulate thruster thermal input) operated at too high a temperature (700°C) and were too close to the isolator. This could have been a source of contamination. Another possible source of contamination is sputter deposition on the insulator from micro-discharges between the protective shields. Although discharges could not be seen visually, the electrometer was observed to fluctuate sporadically at applied voltages above about 3.5 kV. Although determining the source of the observed leakage current was beyond the scope of this study, we recommend further investigation to determine whether a problem actually exists.

D. CONCLUSIONS

The study described in this section was a "single-pass" evaluation of propellant electrical isolator technology. Although refinement of the designs evaluated could be expected to affect the results quantitatively, we feel that the following general conclusions can be drawn:

- The multisection isolator approach can be scaled for higher voltage operation based on the Paschen minimum voltage principle.
- An isolator with adequate voltage capability can be demonstrated in a configuration that does not perturb the design of the EMT.
- The insulating labyrinth isolator approach can provide high-voltage isolation, but the design criteria are not well established.

The problem of isolator leakage at the high voltages used (4 to 6 kV) is unresolved, but should be tractable by the same procedures used in developing the EMT isolator. Therefore, we conclude that the design

and development of a high-voltage propellant electrical isolator to meet the requirements of the Halley's comet mission can be accomplished within the required time period and at a low technical risk.

SECTION 4

A CHARGE EXCHANGE PLASMA EFFLUX MODEL

One PMaC approach studied under this program would provide the high voltage necessary to operate the ion thrusters by a direct series connection of the solar cells in the solar array. Consequently, large areas of the solar panel must operate at high positive potential with respect to the rest of the spacecraft. Although the high-energy ion beam exhaust is not expected to be influenced by these high-potential surfaces, the low-energy ions that will form near the thruster by charge exchange could present a problem. These ions drift out of the beam, driven by thermal velocities and potential gradients in and around the edge of the high-energy ion-beam plume. The electrons may possibly be conducted from the thruster neutralizer through the dilute "plasma" formed by these charge-exchange ions and be collected by the high-voltage solar array. Our objective was to develop an analytic model to describe the charge-exchange ion efflux from a 30-cm EMT. This model was developed and presented to NASA LeRC during the first month of the program for use in analyzing possible interactions between the spacecraft and the solar array that could result from operating the ion thrusters using a high-voltage solar array.

The charge-exchange plasma model presented here was derived primarily on the basis of experience and measurements made with a single 30-cm thruster. Simplifying assumptions were made to permit analytic descriptions to replace empirical data. The results obtained are considered to be as accurate as any published in the literature. No attempt was made to include assymmetries associated with operating a single neutralizer. Similarly, it was considered to be an overspecification to infer the variation in space potential outside of the ion beam. The charge exchange ion production was calculated and it was assumed that a reasonable potential distribution existed within the ion beam. This produces an ion density and velocity distribution at the beam edge (the beam edge is defined here as the boundary of the envelope containing 95% of the primary ion beam current).

A. CHARGE-EXCHANGE ION CALCULATIONS

Several simplifying assumptions were used in calculating the charge exchange ion flux:

- The neutral atom efflux is emitted in a cosine distribution with a uniform distribution at z = 0. The total neutral atom efflux was 250 mA (equivalent current if each atom were charged).
- The distribution of the primary beam current is Gaussian with a spreading half angle of 15^{o}. A beam current of 2 A was used.
- The charge exchange ions travel in a radial direction and are emitted from a conical boundary enclosing 95% of the primary beam current.
- The potential distribution within the ion beam region is described by the Boltzmann equation with an electron temperature of 5 eV.

The neutral and primary ion beam density distributions are described below in more detail, followed by the charge-exchange calculation.

1. Neutral Density Analysis

Figure 28 shows the geometry used to calculate the downstream neutral density. In these calculations it was assumed that the neutrals are emitted uniformly over the thruster diameter at z = 0 with a cosine distribution. This assumption permits calculating the neutral efflux passing through an annular region having radii r_1 and r_2 a distance z downstream from the thruster by using formulas used for calculating radiant heat transfer.[13] The view factor F_{12} is defined as the fraction of the total flux leaving surface 1 (assumed to emit in a cosine distribution) that lands on surface 2. The neutral efflux Hg_o leaving the thruster and landing on the annular region is thus

$$Hg_{o_1} F_{12} = Hg_{o_2} . \qquad (25)$$

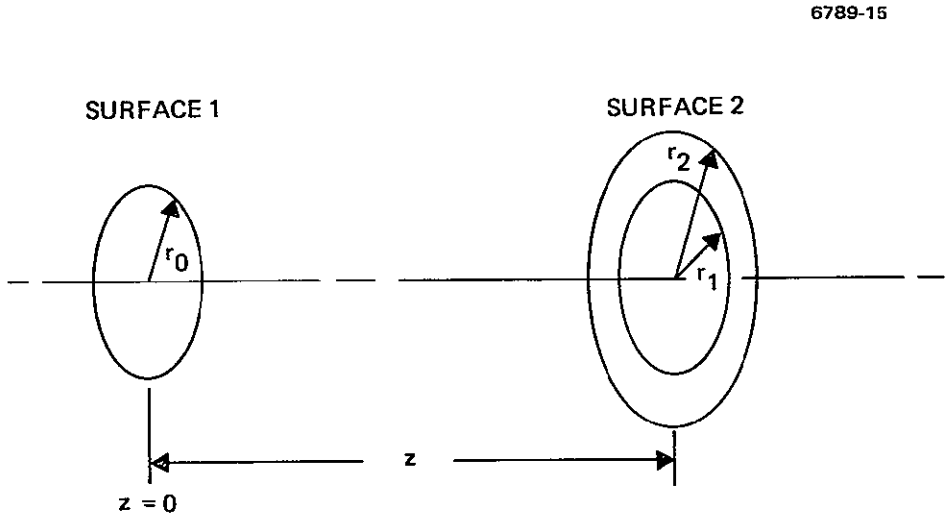

Figure 28. Geometry used for neutral density calculations.

Since the flux is equal to nvA, where n is the density (particles/cm^3), v is the velocity (cm/sec), and A is the area (cm^2), the neutral density at the thruster, n_o, is related to the density at the annular region n (r_1,r_2,z) by

$$n_o A_1 F_{12} = n(r_1,r_2,z) A_2 \tag{26}$$

or

$$\frac{n(r_1,r_2,z)}{n_o} = \frac{r_0^2}{(r_2^2 - r_1^2)} F_{12} \quad , \tag{27}$$

where

$$F_{12} = \frac{1}{2 r_0^2} [(r_2^2 - r_1^2) + \sqrt{T_2} - \sqrt{T_1}] \tag{28}$$

$$T_2 = \sqrt{(r_0^2 + r_2^2 + z^2)^2 - 4 r_2^2 r_0^2} \tag{29}$$

$$T_1 = \sqrt{(r_0^2 + r_1^2 + z^2)^2 - 4 r_1^2 r_0^2} \, . \tag{30}$$

As $r_2 \rightarrow r_1$, Eq. 27 represents the neutral density n(r,z) at radius r where r = 1/2 (r_2 + r_1). This relationship is plotted in Figure 29 as a function of r with Z as a parameter. These curves show how the square distribution at the thruster becomes progressively flatter as z increases. Numerically, for a total neutral efflux of 250 mA (equivalent), an area of 660 cm^2, and a neutral velocity of 2.4 x 10^4 cm/sec ($\sim 300^oC$) we have

$$n_o = \frac{0.250}{660 \times 2.4 \times 10^4 \times 1.6 \times 10^{-19}} \approx 10^{11} \frac{\text{atoms}}{cm^3} \, . \tag{31}$$

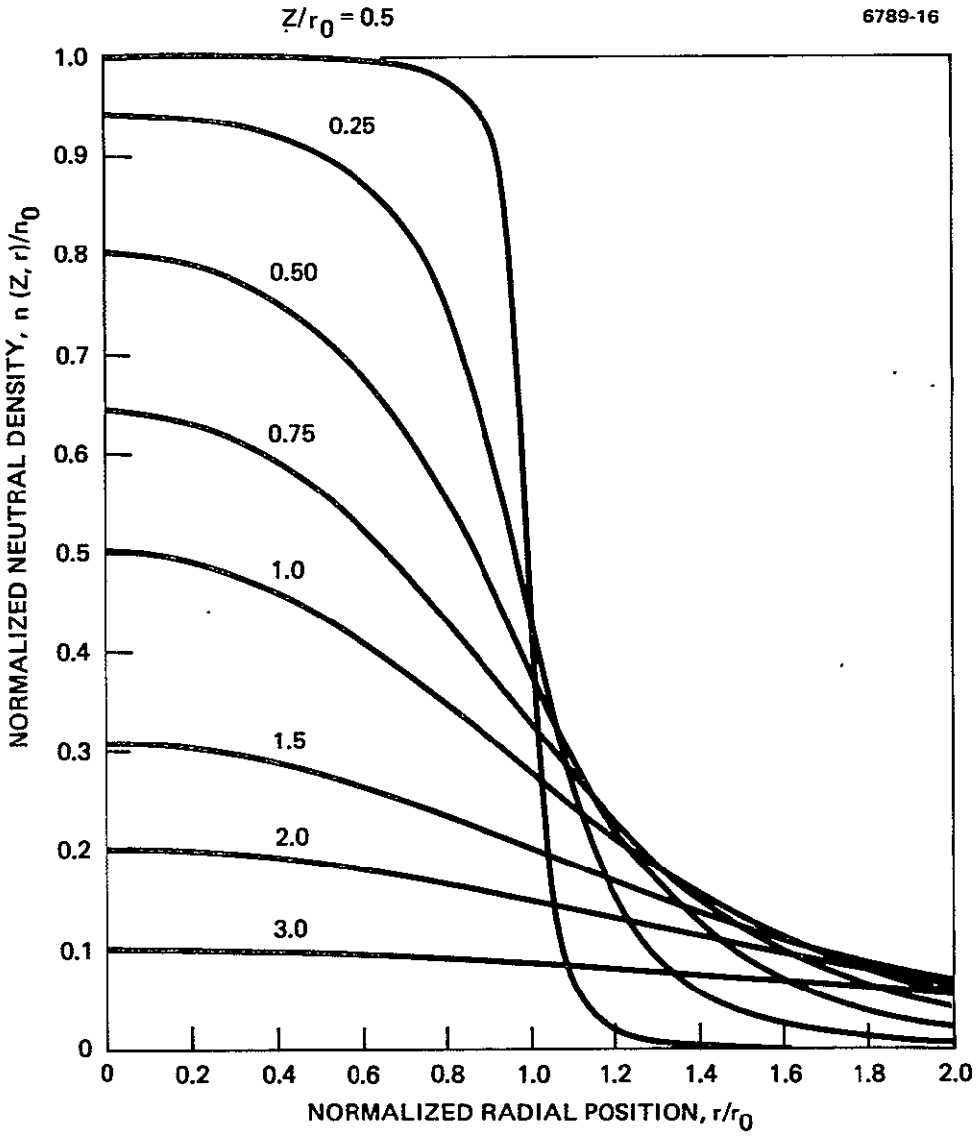

Figure 29. Calculated neutral density (normalized to n_0) as a function of radius with axial position as a parameter.

This value together with the distribution shown in Figure 29 and described by Eq. 27 were used for all the charge-exchange calculations. Since the charge-exchange generation rates are directly proportional to n_o, the generation rate at any other neutral efflux value can be scaled proportionally. This neutral efflux for the 30-cm EMT is essentially independent of ion beam current in the range of currents considered (1 to 2.5 A).

2. Primary Beam Current Density

At any z position, the primary current density was assumed to have a Gaussian profile with a radial dependence described by

$$J(r) = J_o \, e^{-\left(\frac{r}{r_o}\right)^2} . \tag{32}$$

Since the total beam current is given by

$$I^+ = \int_0^\infty 2\pi r J(r,z) \, dr = \pi r_0^2 \, J_o , \tag{33}$$

the current density on axis (r = o) is

$$J_o = I^+/\pi r_0^2 . \tag{34}$$

The current contained up to radius r is

$$I(r) = \int_0^r 2\pi r J(r,z) \, dr \tag{35}$$

or

$$I(r) = I^{+}\left[1 - e^{-\left(\frac{r}{r_o}\right)^2}\right]. \qquad (36)$$

When r equals $\sqrt{3}\,r_0$, $(r) = I^{+}\,[1 - e^{-3}] = 0.95\ I^{+}$ (i.e., 95% of the beam current is contained in a radius defined as $r_{95} = \sqrt{3}\ r_o$). This r_{95} radius is defined to be the beam "edge" at which the charge-exchange current and density was calculated. In reality, there is no beam edge where the beam density abruptly drops to zero. It was further assumed that the r_{95} current envelope spreads with a 15^{o} half angle. This beam divergence is representative for I^{+} = 2 A, V^{+} = 1100 V, and V^{-} = 500 V. From the above assumptions it follows that

$$r_{95} = 15 + z \sin 15^{o}\ , \text{ cm} \qquad (37)$$

The resulting current-density profiles calculated using Eqs. 25, 27, and 30 are shown in Figure 30 where J(r,z) is plotted versus r with z as a parameter. The ordinate in Figure 30 can be converted to density in ions/cm^3 by multiplying by 1.92 x 10^9 (i.e., 1 mA/cm^2 at 1100 V is 1.92 x 10^9 ions/cm^3). For a 1 A beam at 3.9 kV, multiply by 0.5 $\sqrt{1100/3900}$ x (1.92 x 10^9) = 5.07 x 10^8; for a 2.5 A beam at 2.75 kV multiply by (2.75/200) x $\sqrt{1100/2750}$ x (1.92 x 10^9) = 1.67 x 10^9.

3. Charge Exchange Calculations

The charge exchange current can be easily calculated from the expressions for the primary ion current J(r,z) and neutral density n(r,z). The total charge exchange current dI_{cx} created in a path length dz is

$$dI_{cx} = \int_0^{\infty} [J(r,z)\ 2\pi r\ n(r,z)\ dr]\ \sigma\ dz\ , \qquad (38)$$

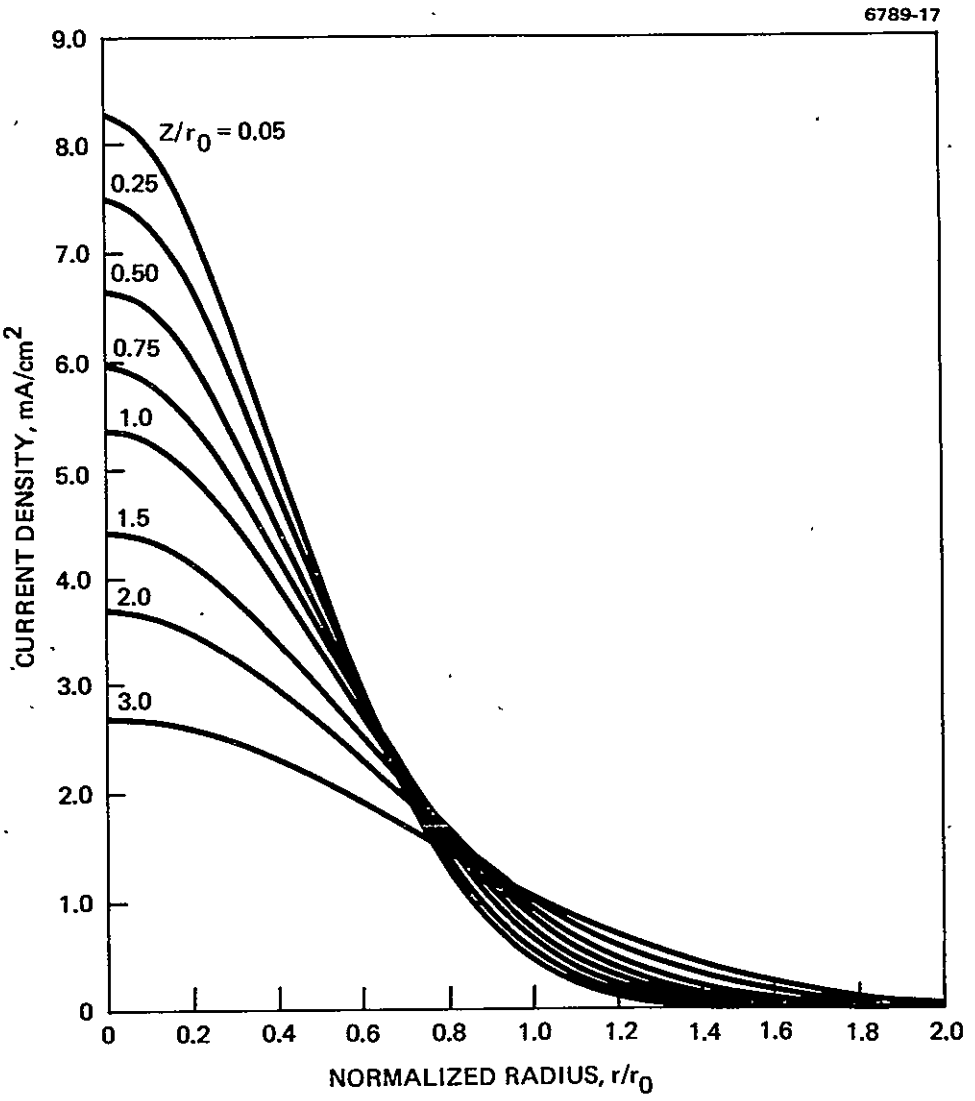

Figure 30. Primary beam current density as a function of radius with axial position as a parameter.

where σ is the charge exchange cross section, which was taken as 7×10^{-15} cm^2 from Ref. 14. This is its value at 1100 V; it increases slowly with decreasing voltage. The total current created in the space between the thruster and the axial location, 0 to z, is given by

$$I_{cx}(z) = \int_0^z dI_{cx} \, . \tag{39}$$

This expression was numerically integrated, and the result is shown in Figure 31. Most of the charge-exchange current is created close to the thruster; for example, $\sim$ 75% of the total charge-exchange current is created within one thruster diameter and $\sim$ 90% is created within two diameters. These calculations of the total generated current do not depend on the position of the beam edge or on the direction in which the ions move.

B. CHARGE EXCHANGE ION EFFLUX

Although the calculation of the charge-exchange ion-generation rate does not depend on the position of the beam edge or on the direction in which the ions move, the calculation of the ion efflux from the beam does. The high-energy ions are essentially mono-energetic and have velocities that are directed primarily along the thrust axis. If there were no electrons injected into this beam, a logarithmically varying potential gradient would be established in a radial direction (the beam edge would expand rapidly with increasing distance from the plane of the accelerator). Ideally, the neutralizer supplies electrons to equal the ion space charge density and thus there is no net charge at any point in the neutralized ion beam envelope. But in reality, the electrons have thermal energy and their velocities are randomly directed and higher than the velocities of the highly directed heavy ions. Consequently, a radially directed potential distribution is established to prevent electron loss at the beam edge (as determined by the ion trajectories from the outermost electrode apertures). In

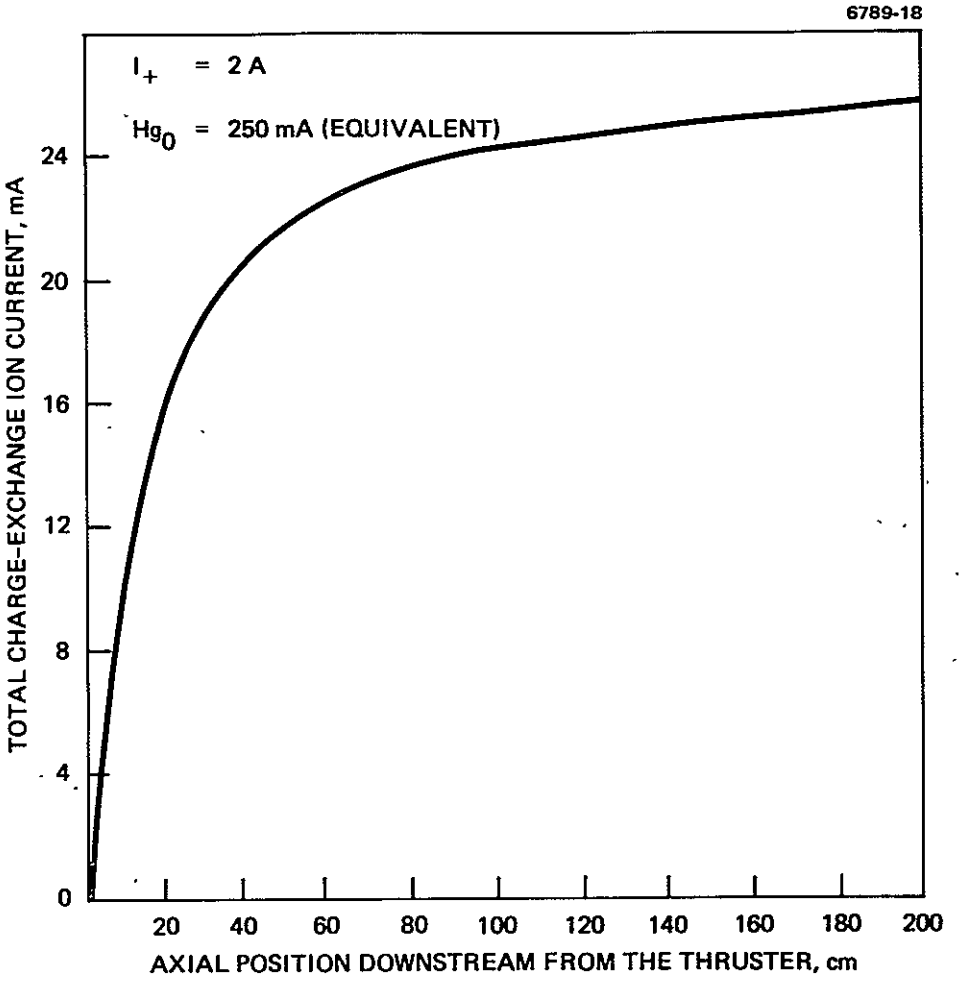

Figure 31. Total charge-exchange ion formation in interval from z = 0 to distance z downstream of thruster. (Note that ∿ 75% of the total charge-exchange ions generated are formed within a distance of one thruster diameter (30 cm)).

where σ is the charge exchange cross section, which was taken as 7×10^{-15} cm^2 from Ref. 14. This is its value at 1100 V; it increases slowly with decreasing voltage. The total current created in the space between the thruster and the axial location, 0 to z, is given by

$$I_{cx}(z) = \int_0^z dI_{cx} \quad . \tag{39}$$

This expression was numerically integrated, and the result is shown in Figure 31. Most of the charge-exchange current is created close to the thruster; for example, $\sim$ 75% of the total charge-exchange current is created within one thruster diameter and $\sim$ 90% is created within two diameters. These calculations of the total generated current do not depend on the position of the beam edge or on the direction in which the ions move.

B. CHARGE EXCHANGE ION EFFLUX

Although the calculation of the charge-exchange ion-generation rate does not depend on the position of the beam edge or on the direction in which the ions move, the calculation of the ion efflux from the beam does. The high-energy ions are essentially mono-energetic and have velocities that are directed primarily along the thrust axis. If there were no electrons injected into this beam, a logarithmically varying potential gradient would be established in a radial direction (the beam edge would expand rapidly with increasing distance from the plane of the accelerator). Ideally, the neutralizer supplies electrons to equal the ion space charge density and thus there is no net charge at any point in the neutralized ion beam envelope. But in reality, the electrons have thermal energy and their velocities are randomly directed and higher than the velocities of the highly directed heavy ions. Consequently, a radially directed potential distribution is established to prevent electron loss at the beam edge (as determined by the ion trajectories from the outermost electrode apertures). In

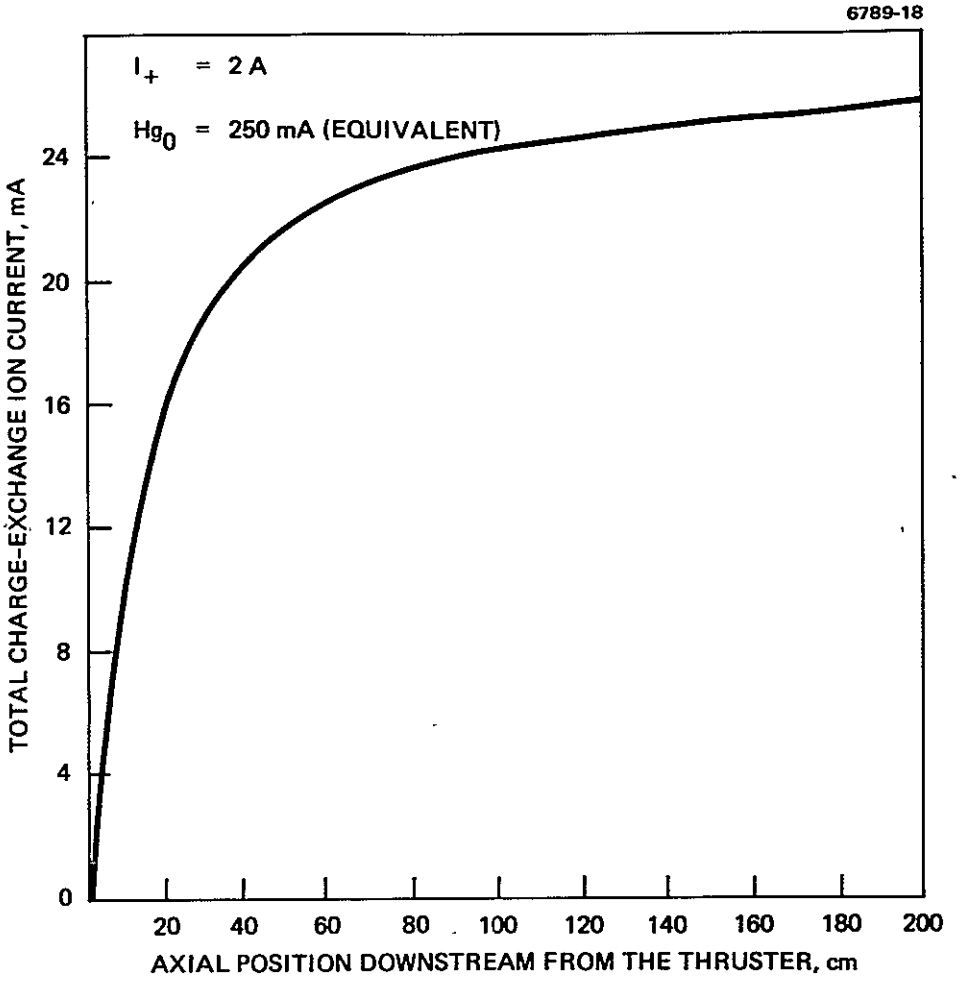

Figure 31. Total charge-exchange ion formation in interval from z = 0 to distance z downstream of thruster. (Note that ∿ 75% of the total charge-exchange ions generated are formed within a distance of one thruster diameter (30 cm)).

the absence of physical boundaries, electron motion along the beam axis is unrestricted and any significant potential gradient (relative to the radial potential gradient) would be rapidly eliminated by electron motion. But if electrons are able to escape from the beam in an axial direction, then an axial potential gradient will also be established. This would be the case for an ion thruster operated in a vacuum chamber. Consequently, experimentally measured axial variations in potential are expected to depend strongly on the boundary conditions in the experiment, and we do not consider the existence of an axial potential gradient to be representative of operating an ion thruster in space. Therefore, to calculate the charge-exchange current density we will assume that the ions move in a radial direction and that the charge-exchange current density differential $dJ_{cx}(r,z)$ is defined by

$$dJ_{cx}(n,z) = \frac{dI_{cx}(z)}{2\pi\, r_{95}} .$$

This is a worst case assumption since a small amount of current generated outside r_{95} has been included. This current density is plotted in Figure 32 and is shown in tabular form in Table 9. Figure 32 shows the rapid decrease in J_{cx} with distance. For example, at one thruster diameter downstream the current density is $\sim$ 12% of the value at z = 0. To calculate the charge-exchange density at r_{95} requires estimating the average velocity in the radial direction at the beam edge, which is a function of the beam plasma potential distribution, V(r).

Kaufman[15] has shown that a good approximation to the potential distribution of the beam is described by the Boltzmann equation that relates the plasma density, potential, and electron temperature as follows:

$$n = n_o\, e^{-\frac{eV}{kT_e}} \qquad (40)$$

Table 9. Tabular Data for Charge-Exchange Data Plotted in Figures 5 and 6

Z (cm)	r_{95} (cm)	J_{cx1} $\mu A/cm^2$	n ions/cm^3
2	15.52	1.29E+01[a]	2.59E+09
4	16.03	1.13E+01	2.26E+09
6	16.55	9.66E+00	1.93E+09
8	17.07	8.18E+00	1.64E+09
10	17.59	6.91E+00	1.38E+09
12	18.10	5.84E+00	1.17E+09
14	18.62	4.95E+00	9.91E+08
16	19.14	4.22E+00	8.44E+08
18	19.66	3.61E+00	7.23E+08
20	20.18	3.11E+00	6.22E+08
22	20.69	2.69E+00	5.39E+08
24	21.21	2.34E+00	4.69E+08
26	21.73	1.05E+00	4.10E+08
28	22.26	1.80E+00	2.60E+08
30	22.76	1.59E+00	3.18E+08
32	23.28	1.41E+00	2.82E+08
34	23.80	1.26E+00	2.52E+08
36	24.32	1.12E+00	2.25E+08
38	24.83	1.01E+00	2.02E+08
40	25.35	9.10E-01	1.82E+08
42	25.87	8.23E-01	1.65E+08
44	26.39	7.46E-01	1.49E+08
46	26.90	6.79E-01	1.36E+08
48	27.42	6.19E-01	1.24E+08
50	27.94	5.67E-01	1.13E+08
52	28.46	5.20E-01	1.04E+08
54	28.97	4.78E-01	9.55E+07
56	29.49	4.40E-01	8.80E+07
58	30.01	4.06E-01	8.13E+07
60	30.53	3.76E-91	7.52E+07
62	31.04	3.49E-01	6.97E+07
64	31.56	3.24E-01	6.47E+07
66	32.08	3.01E-01	6.02E+07
68	32.60	2.81E-01	5.61E+07
70	33.11	2.62E-01	5.24E+07
72	33.63	2.45E-01	4.90E+07
74	34.15	2.29E-01	4.59E+07
76	34.67	2.15E-01	4.30E+07
78	35.19	2.02E-01	4.04E+07
80	35.70	1.90E-01	3.80E+07
82	36.22	1.79E-01	3.58E+07
84	36.74	1.68E-01	3.37E+07
86	37.26	1.59E-01	3.18E+07
88	37.77	1.50E-01	3.00E+07
90	38.29	1.42E-01	2.84E+07
92	38.81	1.34E-01	2.69E+07
94	39.33	1.27E-01	2.55E+07
96	39.84	1.21E-01	2.42E+07
98	40.36	1.15E-01	2.29E+07
100	40.88	1.09E-01	2.18E+07

Z (cm)	r_{95} (cm)	J_{cx} $\mu A/cm^2$	n ions/cm^3
102	41.40	1.04E-01	2.07E+07
104	41.91	9.86E-02	1.97E+07
106	42.43	9.39E-02	1.88E+07
108	42.95	8.96E-02	1.79E+07
110	43.47	8.54E-02	1.71E+07
112	43.98	8.16E-02	1.63E+07
114	44.50	7.79E-02	1.56E+07
116	45.02	7.45E-02	1.49E+07
118	45.54	7.13E-02	1.43E+07
120	46.05	6.82E-02	1.36E+07
122	46.57	6.54E-02	1.31E+07
124	47.09	6.26E-02	1.25E+07
126	47.61	6.01E-02	1.20E+07
128	48.12	5.77E-02	1.15E+07
130	48.64	5.54E-02	1.11E+07
132	49.16	5.32E-02	1.06E+07
134	49.68	5.11E-02	1.02E+07
136	50.20	4.92E-02	9.83E+06
138	50.71	4.73E-02	9.46E+06
140	51.23	4.55E-02	9.11E+06
142	51.75	4.39E-02	8.77E+06
144	52.27	4.23E-02	8.45E+06
146	52.78	4.07E-02	8.15E+06
148	53.30	3.93E-02	7.86E+06
150	53.82	3.79E-02	7.58E+06
152	54.34	3.66E-02	7.32E+06
154	54.85	3.53E-02	7.07E+06
156	55.37	3.41E-02	6.83E+06
158	55.89	3.30E-02	6.60E+06
160	56.41	3.19E-02	6.38E+06
162	56.92	3.08E-02	6.17E+06
164	57.44	2.98E-02	5.97E+06
166	57.96	2.89E-02	5.78E+06
168	58.48	2.80E-02	5.59E+06
170	58.99	2.71E-02	5.42E+06
172	59.51	2.62E-02	5.25E+06
174	60.03	2.54E-02	5.09E+06
176	60.55	2.47E-02	4.93E+06
178	61.06	2.39E-02	4.78E+06
180	61.58	2.32E-02	4.64E+06
182	62.10	2.25E-02	4.50E+06
184	62.62	2.19E-02	4.37E+06
186	63.14	2.12E-02	4.24E+06
188	63.65	2.06E-02	4.12E+06
190	64.17	2.00E-02	4.00E+06
192	64.69	1.95E-02	3.89E+06
194	65.21	1.89E-02	3.78E+06
196	65.72	1.84E-02	3.68E+06
198	66.24	1.79E-02	3.58E+06

[a]Expressed in scientific notation, e.g., 1.29E+01 = 1.29 x 10^1.

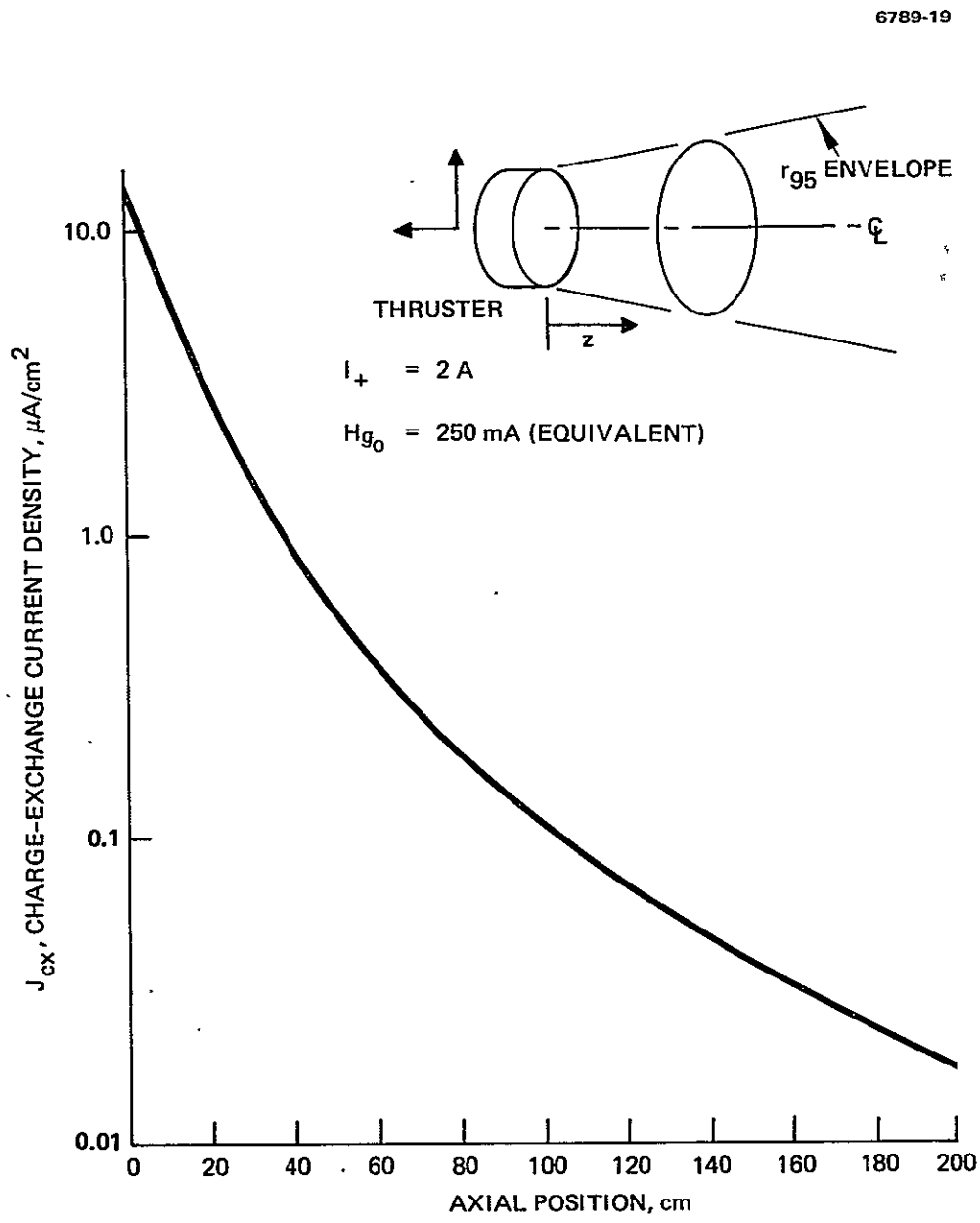

Figure 32. Calculated current density of Hg^+ charge-exchange ions passing through conical surface enclosing 95% of beam current as a function of distance downstream from the thruster.

For this equation to be consistent with

$$J = J_o \, e^{-\left(\frac{r}{r_o}\right)^2} , \tag{41}$$

it is necessary that the following equation hold:

$$eV(r) = kT_e \left(\frac{r}{r_o}\right)^2 . \tag{42}$$

At r_{95} where $r = \sqrt{3}\, r_o$, $V(r) \cong 3\ kT_e = -15$ V, where the center of the beam at $r = 0$ is at $V = 0$. Let $g(r,z)$ be the volume charge-exchange generation rate (in A/cm^3), where $g(r,z)$ equals $J(r,z)\ n(r,z)\ \sigma$. Then the average velocity $\langle u \rangle$, at the r_{95} beam edge is given by

$$\langle u(z) \rangle = \int_0^{r_{95}} g(r,z) \sqrt{\frac{2e}{m_i}\left[V_{95} - V(r)\right]} \cdot 2\pi r \, dr \Big/ \int_0^{r_{95}} g(r,z)\ 2\pi r \, dr . \tag{43}$$

This expression was evaluated at several z positions from $z = 0$ to $z = 200$ cm. The average energy is essentially independent of z with a value 10.1 ± 2 eV (which is $\approx 2\ kT_e$). The corresponding average velocity, $\langle v \rangle$, can therefore be obtained by solving

$$\frac{1}{2} m \langle v \rangle^2 = 2\ kT_e , \tag{44}$$

which yields

$$\langle v \rangle = 2\sqrt{\frac{kT_e}{m_i}} \cong 3.1 \times 10^5 \text{ cm/sec} , \tag{45}$$

which is twice the Bohm minimum velocity for formation of a stable sheath (the Bohm velocity was derived for a monoenergetic velocity distribution). Using this value of $\langle v \rangle$, the charge-exchange current densities were converted to ion number densities using $n = J/e\langle v \rangle$ and plotted in Figure 33 as a function of distance downstream from the thruster.

C. EFFLUX MODEL FOR A THRUSTER ARRAY

To estimate the charge-exchange boundary for an array of thrusters, the current-density distribution for a 6 x 2 thruster array was calculated at z = 30 cm and z = 60 cm downstream from the array. The primary ion beam current density distribution at an arbitrary point was obtained by summing the current density contributions for each of the 12 thrusters at the observation point r_o:

$$J_{tot}(r_o,z) = \sum_{i=1}^{12} J_i \exp\left(-\Delta_i^2/r_o^2\right) , \qquad (46)$$

where $\Delta_i = |r_o - r_i|$ is the distance between the center of the thruster and the observation point. Contours were calculated for normalized amplitudes of e^{-1}, e^{-2}, and e^{-3}. The latter is the 5% amplitude defined to be the nominal beam edge that encloses 95% of the beam current. The results of these calculations are shown in Figure 34. The contours shown in Figure 34 show that at z = 30 cm the thrust beams have not merged (i.e., the source boundary for the charge exchange ions are circular) and that at z = 60 cm the r_{95} boundaries have merged to form an undulating rectangular boundary. For either case, however, the far-field current density distribution must be obtained by calculating trajectories that pass through the beams of adjacent thrusters; such a calculation would be beyond the scope of this work.

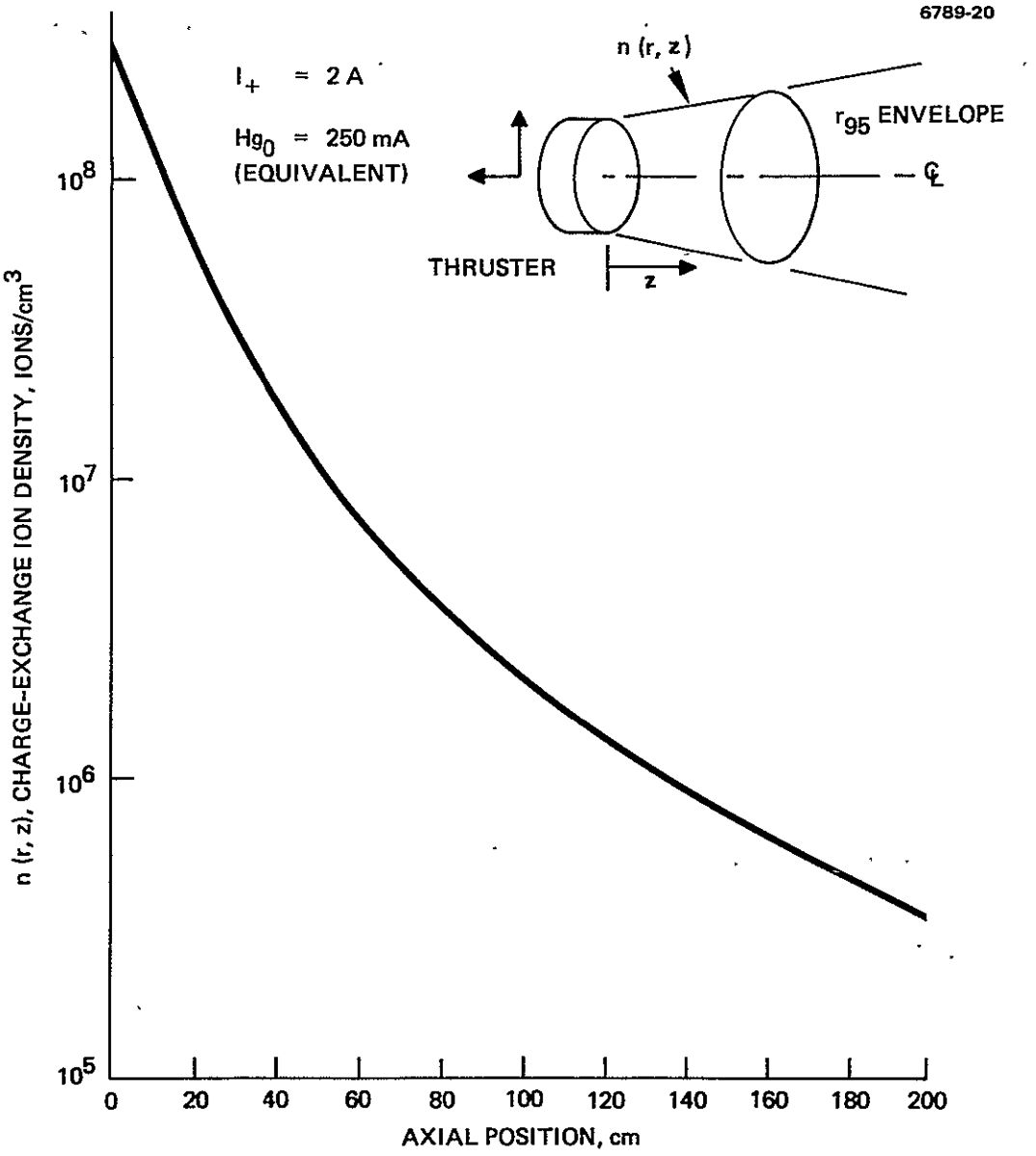

Figure 33. Calculated density of Hg^+ charge-exchange ions at conical surface enclosing 95% of beam current as a function of distance downstream from the thruster.

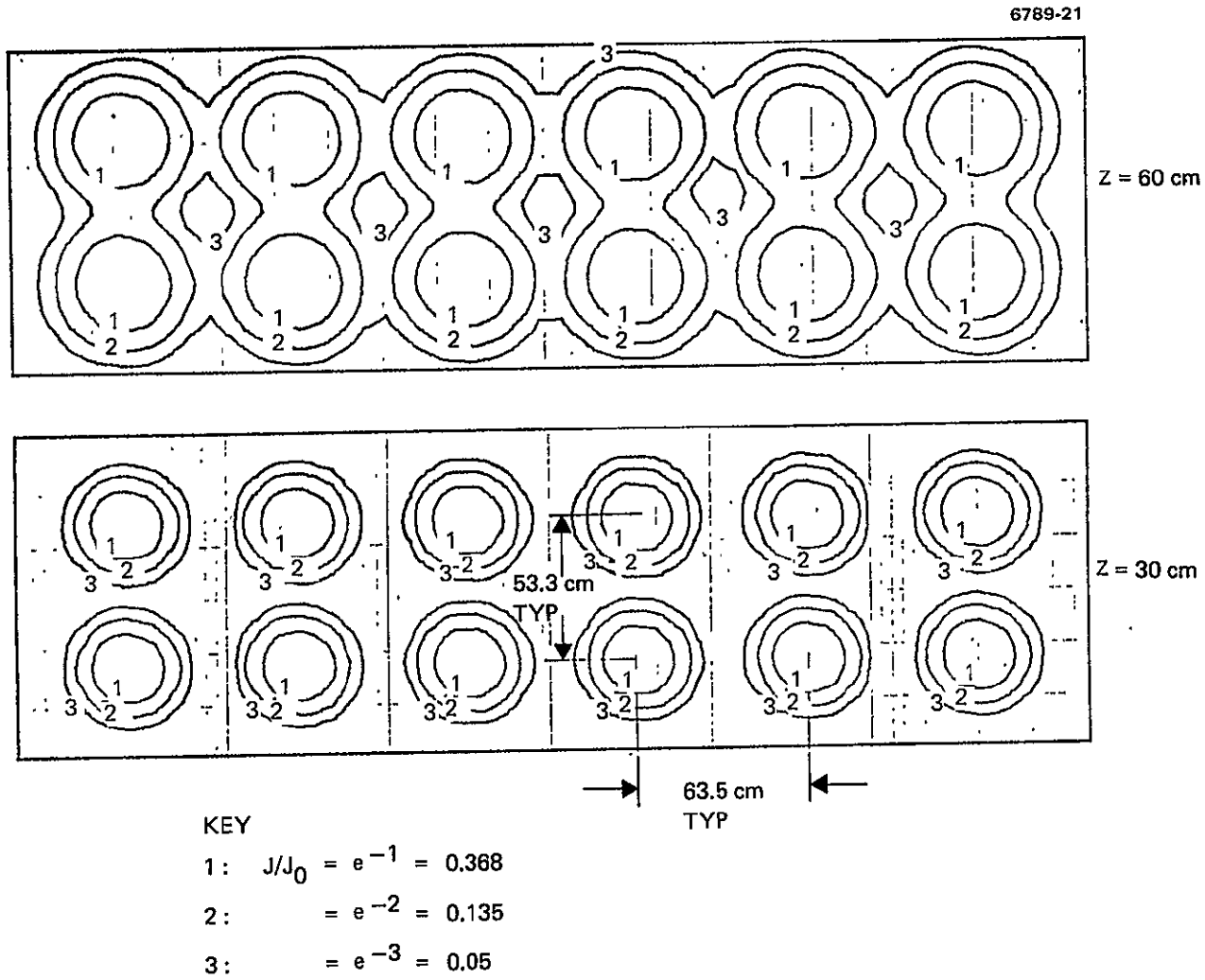

Figure 34. Calculated contours of constant current density for a 2 x 6 array of thrusters for axial positions of 30 and 60 cm. (The r_{95} contours have not merged at z = 30 cm but they have at z = 60 cm.)

A rather crude estimate can be made for combinations of thrusters by assuming that the charge-exchange space charge will collect in the region between thrusters until a potential distribution is formed such that the neutralizing electrons are confined. At this point, charge exchange ions will again be driven out of the beam region at the same rate at which they are generated. Figure 35 shows two examples of combined beams at z = 60 cm. The current densities J_1 and J_2 shown in Figure 35(a) refer to the curved and linear segments of the combined beam envelope. The current density, J_1, is simply the value given in Table 9 for z = 60 cm.

The current density J_2 is given by

$$J_2 = \frac{60.5\pi \times J_1}{2 \times 53.3} = 1.8\ J_1 \ . \tag{47}$$

For the 12-thruster case (Figure 35(b)), J_1 and J_2 are obtained in the same manner; J_3, however, is given by

$$J_3 = \frac{10 \times 61 \times \pi}{2 \times 320} J_1 = 3J_1 \ . \tag{48}$$

Hence the geometry and current density for a combined beam envelope can be obtained using the above expressions and Table 9 for any value of z.

D. THE HOLLOW CATHODE NEUTRALIZER

The hollow cathode neutralizer used on the 30-cm ion thruster is fundamentally an electron source that provides electrons to the ion beam to equalize or neutralize the ion current. The configuration in use is shown as Figure 36 with densities and potentials as indicated. The relatively low-voltage (12 to 20 V) discharge that is maintained between the cathode orifice and the keeper (keep alive) electrode serves to maintain a high-density plasma in the cathode orifice region and to supply electrons to the ion beam. If the neutral and charged

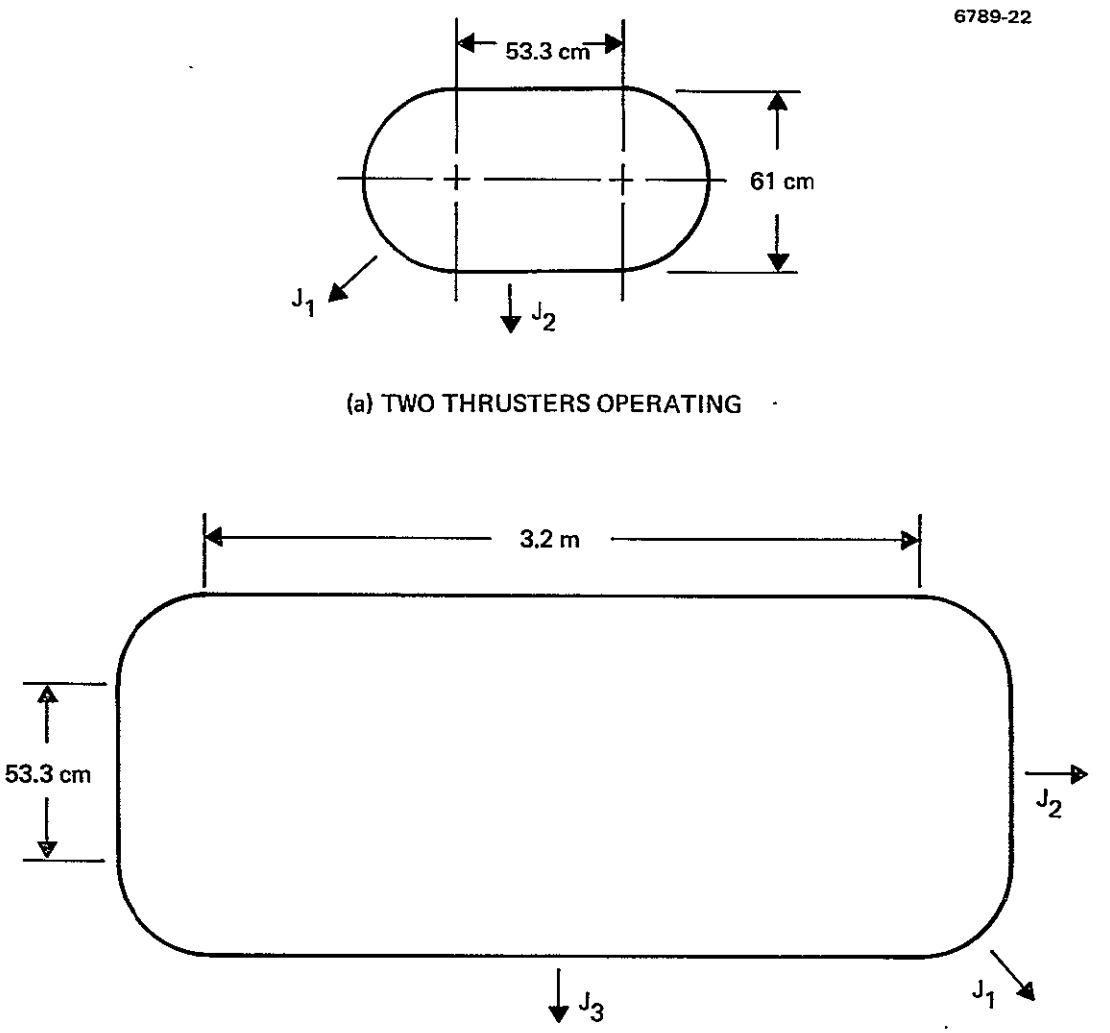

Figure 35. Assumed cross section for combined ion beams at z = 60 cm.

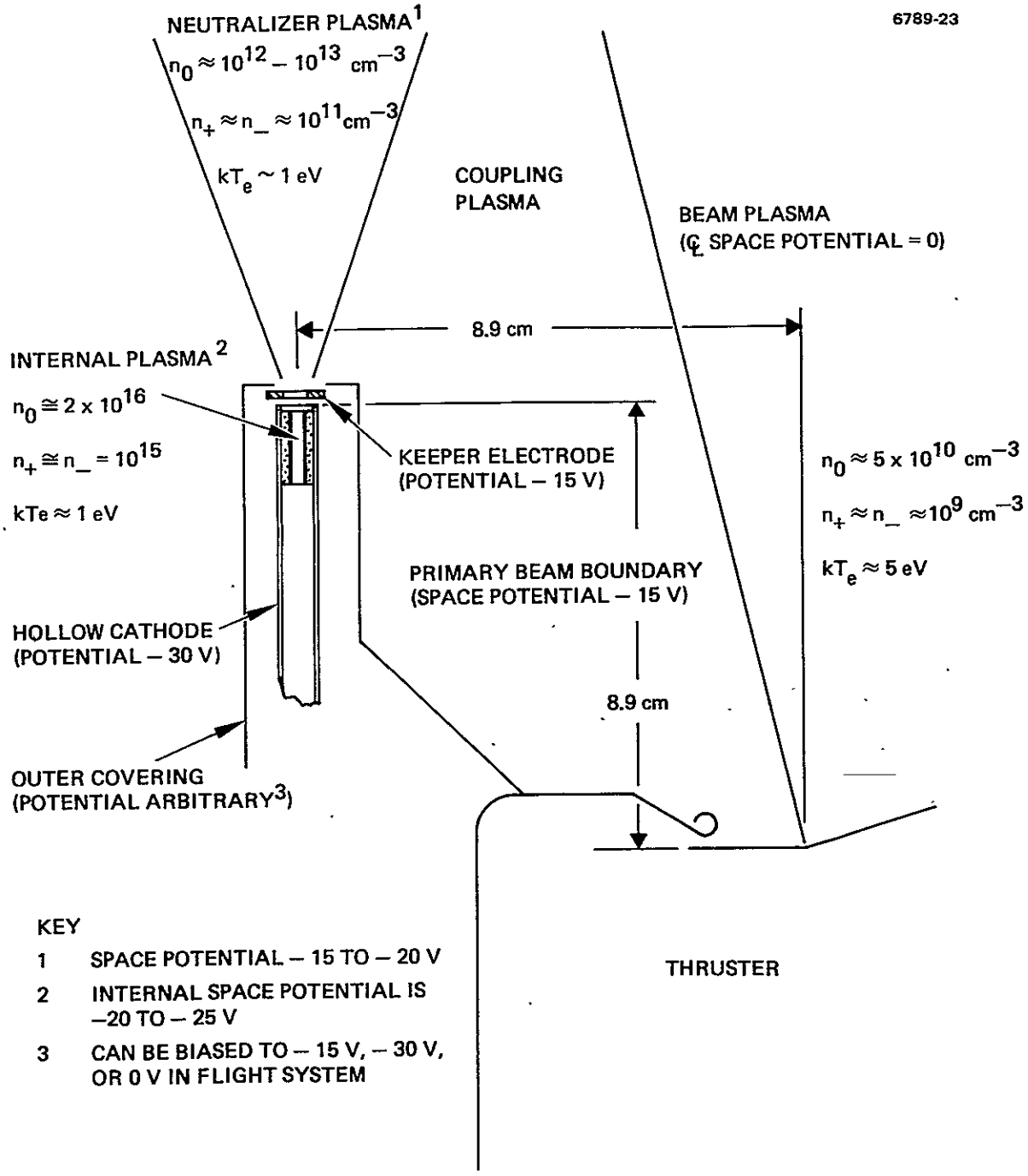

Figure 36. Neutralizer/ion-beam diagram.

particle densities in the orifice and surrounding regions are as shown in Figure 36, the process of beam neutralization is thought to be relatively effective and any azimuthal assymmetries that might be present are very localized to a region within several cm of the neutralizer. A complete description of hollow cathode and neutralizer operation can be found in Ref. 16 through 27.

E. CONCLUSIONS

The generation of charge-exchange ions in the ion-beam exhaust plume takes place predominantly in the region immediately downstream from the accelerator electrode. The neutralized ion beam establishes a radial potential gradient to contain the neutralizing electrons and this potential gradient expels the charge exchange ions from the ion beam in a radially outward direction. A beam envelope boundary was defined and the charge-exchange ion density and ion current density were calculated as a function of location on the boundary. The results considered to be valid provided that the strength of externally applied electric fields are significantly smaller at the beam boundary than the field required to contain the thermalized electrons (from the neutralizer) in the beam. We presented a technique for scaling the charge-exchange ion efflux in proportion to the ion beam current and also described a procedure for using the calculated data from a single thruster to obtain the efflux from a thruster array. This data, together with the geometry assumed, is considered to form a representative numerical model for the charge-exchange ion efflux that is useful for estimating the plasma densities in the space around the thrust system. The ion beam and efflux model described should also be useful for formulating the numerical boundary conditions necessary for computing the electron and ion currents that will flow between the ion beam plume and any spacecraft or solar array surfaces that would be operated at high relative potentials (as in the case of the direct drive solar array).

SECTION 5

CONCLUSIONS

Each section of this volume contains in detail the conclusions reached for the particular technology area investigated. Therefore, here we only summarize the important conclusions:

- The 900-series 30-cm EMT requires only minor modifications to satisfy the requirements of a Halley's comet rendezvous or other extended performance missions.
- The performance characteristics of the thruster that was modified for extended-performance operation were the same as had been projected from extrapolated EMT data.
- A high-voltage propellant electric isolator design that is based on the EMT isolator concept can be scaled to meet the extended-performance requirements (as defined under this study).
- The capability of EMT technology (the technology includes the modifications required for extended-performance operation) for meeting the lifetime requirements of an extended performance mission was not demonstrated and requires verification.

REFERENCES

1. R.L. Poeschel and R.P. Vahrenkamp, "Performance Mapping of a 30-CM Engineering Model Thruster," AIAA Paper No. 75-342, New Orleans, Louisiana, March 1975.

2. C.R. Collett and R.L. Poeschel, "A 10,000 Hour Endurance Test of a 700 Series 30-CM Engineering Model Thruster," AIAA Paper 76-1019, Key Biscayne, Florida, November 1976.

3. R.L. Poeschel et al., "High-Power and 2.5 kW Advanced-Technology Ion Thruster," NASA CR-135163, Hughes Research Laboratories, February 1977.

4. R.L. Poeschel et al., "2.5 kW Advanced Technology Ion Thruster," NASA CR-134687, Hughes Research Laboratories, August 1974.

5. R.L. Poeschel et al., "2.5 kW Advanced Technology Ion Thrusters," NASA CR-135076, Hughes Research Laboratories, April 1976.

6. Sh. G. Askerov and L.A. Sena, "Cathode Sputtering of Metals by Slow Mercury Ions," Soviet Physics-Solid State 11, No. 6, 1288, December 1969.

7. C.R. Collett and R.T. Bechtel, "An Endurance Test of a 900 Series 30-CM Engineering Model Ion Thruster," AIAA Paper No. 76-1020, Key Biscayne, Florida, November 1976.

8. M.A. Mantenieks and V.K. Rawlin, "Studies of Internal Sputtering in a 30-CM Ion Thruster," AIAA Paper No. 75-400, New Orleans, Louisiana, March 1975.

9. W. Knauer, "Electrical Isolator," U.S. Patent 3,520,110, July 1970.

10. J.W. Pye, "The Development of Electrical Isolators for Mercury Ion Thrusters," Royal Aircraft Establishment Technical Report 73054, Farnborough, England (1973).

11. K. Arnold, Hughes Research Laboratories, private communication.

12. M.A. Mantenieks, "Status of 30-cm-diameter Mercury Ion Thruster Isolator Development," AIAA Paper No. 76-1027, Key Biscayne, Florida, November 1976.

13. E. Eckert, Heat and Mass Transfer (McGraw Hill, N.Y., 1959).

14. H.R. Kaufman, "Charge-Exchange Plasma Generated by an Ion Thruster," NASA CR-134844, June 1975.

15. I.P. Iovitsu and N. Ionescu-Pallas., Sov. Phys. Tech. Phys. 4, 781 (1959).

16. V.K. Rawlin and W.R. Kerslake, "SERT II: Durability of the Hollow Cathode and Future Applications of Hollow Cathodes," Spacecraft and Rockets 7, No. 1, January 1970, pp. 14-20.

17. V.K. Rawlin and E.V. Pawlik, "A Mercury Plasma-Bridge Neutralizer," Spacecraft and Rockets 5, No. 7, July 1968, pp. 814-820.

18. D.F. Hall, R.F. Kemp, and H. Shelton, "Mercury Discharge Devices and Technology," Paper 67-669, Sept. 1967, AIAA, New York, N.Y.

19. J.W. Ward and H.F. King, "Mercury Hollow Cathode Plasma Bridge Neutralizers," Spacecraft and Rockets 5, No. 10, Oct. 1968, pp. 1161-1164.

20. D.C. Byers, "Effect of Power Supply Impedance on the SERT II Neutralizer," TM X-52543, NASA, Cleveland, Ohio, 1969.

21. G.A. Csiky, "Measurement of Some Properties of a Discharge from a Hollow Cathode," TN D-4966, NASA, Cleveland, Ohio, 1969.

22. H.R. Kaufman, "Technology of Electron-Bombardment Ion Thrusters," Advances in Electronics and Electron Physics 36 (Academic Press, San Francisco, 1976).

23. H.L. Witting, "Hollow Cathodes with Thermionic Cathodes," J. Appl. Phys. 42, 5478-82 (1971).

24. R.J. Martin and J.E. Rowe, "Experimental Investigation of the Low Voltage Arc in Noble Gases," J. Appl. Phys. 39, 4289-98 (1968).

25. S.N. Salinger and J.E. Rowe, "Determination of the Predominant Ionization and Loss Mechanisms for the Low-Voltage Arc Mode in a Neon Plasma Diode," J. Appl. Phys. 39, 4299-4307 (1968).

26. H. Minoo, "Contributed Papers to the Conference on Hollow-Cathode Discharges and Their Applications," Universite Paris-Sud, Orsat, France, Sept. 1971.

27. C.M. Philip, "A Study of Hollow Cathode Discharge Characteristics," AIAA Paper No. 70-1087, 1970. Also AIAA J., Vol. 9, pp. 2191-2196 (1971).

28. M. Knoll, F. Ollendorff, and R. Rompe, Gasentladungstabellen (Springer-Verlag, Berlin, 1935).